Article

Model and Simulation of a Floating Hybrid Wind and Current Turbines Integrated Generator System, Part II: Hydrodynamics and Acting Forces

Fernando Tamarit [ID], Emilio García, Eduardo Quiles *[ID] and Antonio Correcher [ID]

Instituto de Automática e Informática Industrial ai2, Universitat Politècnica de València, Camino de Vera s/n, 46022 Valencia, Spain; fertape@posgrado.upv.es (F.T.); egarciam@isa.upv.es (E.G.); ancorsal@upv.es (A.C.)
* Correspondence: equiles@isa.upv.es; Tel.: +34-963877007-75793

Abstract: This work is part of a series of publications that propose a floating hybrid system for which a simulation tool has been developed, called FHYGSYS (Floating Hybrid Generator Systems Simulator). The objective of this series of publications is to analyze the behavior and to evaluate different control strategies of the floating hybrid system. This system consists of an "OC3-Hywind" wind turbine and two marine current turbines presented by the authors in previous publications. This work completes the exposition of the mathematical model of the floating hybrid system started in a previous publication (Part I), in which the inertial, kinematic, and dynamic parts of the model were described. In this second part, the forces acting on the floating system are extensively described, and the turbines are modeled using the so-called One-Dimensional theory (or also known as Simple theory). The results obtained with the FHYGSYS simulation tool have been validated—through a code-to-code comparison—with FASTv8, both in the first part and in this second part of this work.

Keywords: floating wind turbine; marine current turbines; tidal turbines; wind energy; renewable energy; spar-buoy platform; system modelling and identification; added mass processing; moored systems; turbine modeling

1. Introduction

In the first part of this work [1], the mathematical model of a floating hybrid system consisting of a floating wind turbine—a OC3-Hywind-type wind turbine [2,3]—and two marine current turbines such as those described in [4,5] was presented. More specifically, the modeling hypotheses; the method of processing the kinematics, based on the use of homogeneous transformation matrices; and the processing of the dynamics of the floating hybrid system were explained. To complete the computation of the dynamics, the inertial data processing of the different bodies that make up the floating hybrid system and the processing of the added mass of the system were described.

The inertial data of each body of the floating system were obtained using software for the mechanical design of solids—in this case, Solid Works®—and the computation of the entire mathematical model developed was carried out using Matlab®. The resulting software tool was called the Floating Hybrid Generator Systems Simulator (FHYGSYS).

In [1], the following question was asked, and for clarification, at this point, it is interesting to ask it again: "why did we choose to develop our own tool like FHYGSYS? Mainly because, when the research line began, there was no simulation tool that would clearly allow the simulation of marine current turbines, offering the possibility of freely designing different control strategies. The main objective of the research is precisely that: to study the behavior of a hybrid floating system like the one described using different automatic control strategies" [1].

In control engineering, systems modeling is an important part that allows for the development of automatic control strategies and control approaches for failure diagnosis

and prediction of systems to be controlled. For this reason, it is interesting to obtain a mathematical modeling strategy that allows for performing this task in a relatively simple way, as described in [1] and in this paper.

The purpose of FHYGSYS is to offer a mathematical solution for modeling OC3-Hywind-type floating hybrid systems to which marine current turbines are added, constituting a system such as the one shown in Figure 1. In addition, the philosophy described in [1] and in this paper can be adapted to other floating system concepts, or even to other types of systems, whether in a marine environment or not.
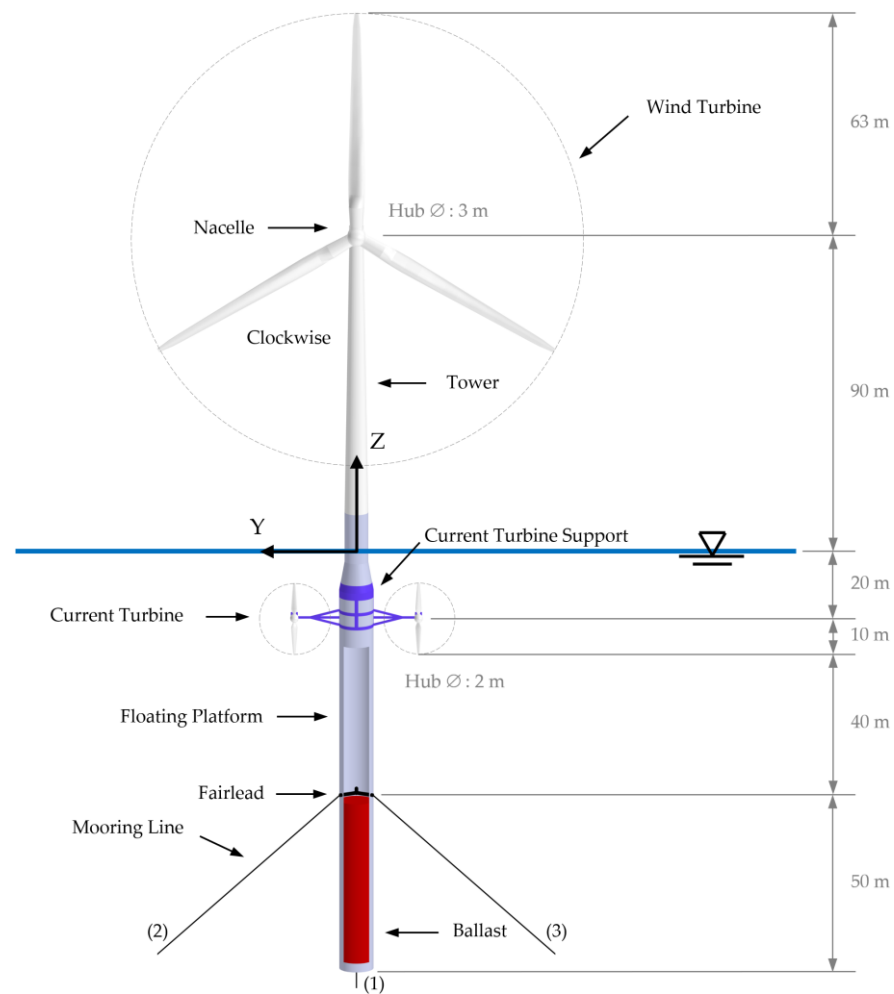

Figure 1. Floating hybrid system: (1), (2), and (3) are the numbers that give names to the mooring lines used in this text to be able to refer to them. This figure was taken from [1].

FHYGSYS executes in its own code the entire mathematical model—kinematics, dynamics, aerodynamics, hydrodynamics, mooring system behavior, gravitational influence, and Coriolis–centripetal effects; this is an important feature of the tool. As FHYGSYS is a time-domain software tool, the processing of the entire mathematical model is executed for each instant of time (a range of values from 0.1 to 0.0125 s has been used). The only externally preprocessed data required—through Solid Works®—are the inertial characteristics of the bodies that make up the floating system and the inertial characteristics of the volume of the submerged elements (these data are found in Appendix A of [1]). The relationship between all the elements processed by the mathematical model is shown in Figure 2.
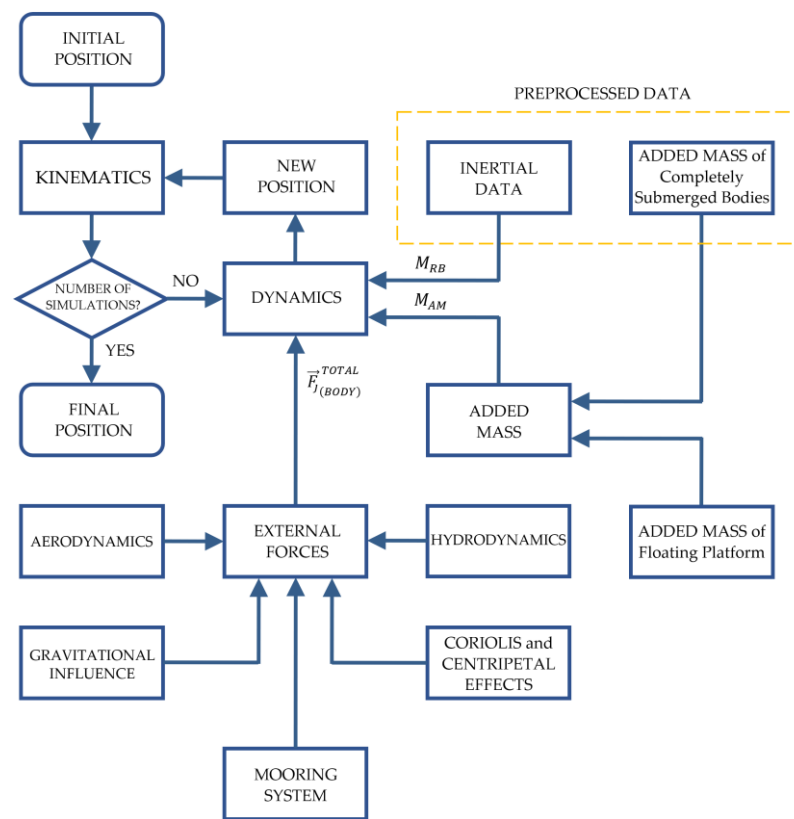
Figure 2. Flowchart of how the entire mathematical model works.

There are different types of wind turbine simulation tools developed by companies or institutions. Some of them are presented below.

FAST [6] is the reference tool in research and in the industrial field for the aero-hydro-servo-elastic simulation of wind turbines both for installations on land and in the sea, whether they are installed on the seabed or on floating systems. FASTv8 [7] is the latest public release under the FAST Modularization Framework before the transition to OpenFAST. WAMIT® [8], which is considered the most advanced set of tools available for analyzing wave interactions with offshore platforms and other structures or vessels, is used by FAST for its operation. OpenFAST [9] is an open-source wind turbine simulation tool—which is under development—that was established with the FASTv8 code as its starting point.

HAWC2 (Horizontal Axis Wind turbine simulation Code 2nd generation) [10] is an aeroelastic code intended for calculating wind turbine response in the time domain. The core of the code was developed by the Aeroelastic Design Research Program at DTU Wind Energy, DTU Risø Campus in Denmark. The QBlade software [11] is a multi-physics code that covers the complete range of aspects required for the aero-servo-hydro-elastic design, prototyping, simulation, and certification of wind turbines. ASHES (aero-servo-hydro-elastic simulation) [12] is a design and analysis software—which is under development—for onshore and offshore wind turbines.

Simulia Wind Turbine Simulation [13] offers a comprehensive suite of wind turbine simulation technologies to optimize and accelerate their design. By accessing Simulia Wind Turbine Simulation technology through the 3D-Experience platform, all design groups and their suppliers can benefit from real-time collaboration and a system-level view on all components. OpenWindPower [14] is offshore wind turbine analysis software that helps choose design alternatives, predict performance, and deliver safe and cost-effective offshore wind farm structures. It can also be used for fixed foundation or floating platform offshore wind turbine projects. DNV offers different software packages for off-shore wind turbines [15]—Bladed, Sesam, and Sima—which provides guidance in the development

of floating offshore wind energy projects. ANSYS Fluent [16] is a fluid simulator software sometimes used in research work.

The WAsP software suite [17]—developed by Technical University of Denmark (DTU)—is an industry standard for wind resource assessment, siting, and energy yield calculation for wind turbines and wind farms.

There are also simulators for the training of wind turbine operator and maintenance technicians, who seek to learn operation and maintenance tasks safely. Simulwind [18] is a European training project for wind farm operation and maintenance personnel, with the aim of developing a simulator capable of showing all the main faults and solutions that can be found in both wind turbines and wind farms. Purdue University Northwest has developed the Wind Tech Safety and Troubleshooting Simulator [19] for the training of wind turbine technicians.

In relation to marine turbine simulation tools, the list is considerably reduced; the authors have only found two relevant tools. TidalBladed [20] is a validated tool—developed by DNV—for simulating tidal turbines at the design stage. OpenTidalFarm [21] is an open-source software for simulating and optimizing tidal turbine farms. All these tools can be compared in Table 1.

Table 1. Comparison of some examples of simulation tools for wind and marine turbine systems.

Tool	License	Simulator Type	Simulates MCT [1]	Simulates FHS [2]
FAST v8 and OpenFAST	Free	Aero-hydro-servo-elastic	No	No
WAMIT	Educational/Commercial	Wave interactions with Offshore structures	-	-
HAWC2	Trial/Commercial	Aeroelastic	No	No
QBlade	Academic/Commercial	Aero-servo-hydro-elastic	No	No
ASHES	Evaluation/Commercial	Aero-servo-hydro-elastic	No	No
Simulia WTS [3]	Commercial	WTS [3] to optimize their design	No	No
OpenWindPower	Commercial	WTS [3] to optimize their design	No	No
DNV software packages	Commercial	WTS [3] to optimize their design	No	No
ANSYS Fluent	Trial/Commercial	Fluid Simulation Software	No	No
WAsP	Educational/Commercial	Wind resource assessment	-	-
Simulwind	GPL [4]	Technician training	No	No
Wind Tech Simulator	Free	Technician training	No	No
TidalBladed	Commercial	TTS [5] to optimize their design	Yes	No
OpenTidalFarm	GPL [4]	Optimizing tidal turbine farms	Yes	No
FHYGSYS	Free (soon)	Aero-servo-hydro	Yes	Yes

[1] Marine Current Turbines. [2] Floating Hybrid Systems. [3] Wind Turbine Simulation. [4] General Public License. [5] Tidal Turbine Simulation.

Regarding research work, there are studies focused on the modeling and simulation of wind and marine turbines.

In [22], a wind action simulation software consisting of two models was used. The first simulates short-term components—representing turbulence using von Karman's model [23]—and the second simulates medium-term and long-term wind speed components, applying Van der Hoven's model [24]. The data generated with the wind simulator were applied to an electromechanical simulator, allowing the torque and speed of the generator shaft to be evaluated by applying a continuous feedback control system. In [25], an electromechanical simulator, similar to the one explained in [22] but in which a wind steady-state behavior model was used, was presented. Similar studies can be found in [26–28].

In [29], a simulator for the study of micro wind turbines for urban areas was presented. It is composed of a fan, which simulates the action of the wind, and was applied to the wind turbine in a wind tunnel. The results were compared with those obtained by simulating

the wind turbine with Blade Element Momentum (BEM) theory and with those obtained with the commercial software ANSYS Fluent [16].

Focusing on floating wind turbines, [30] presented an in-depth analysis of the different floating system modeling tools existing at that time, analyzing the structural dynamics, aerodynamics, hydrodynamics, and the mooring system of each one of them.

In [31], a high-fidelity aerodynamic method was presented to correct the speed of the incident wind on the rotor of a floating wind turbine. This method can be applied to any simulation code. In [32], the different loads acting on an offshore wind turbine were explained, analyzing the modeling alternatives in each case. The study focused on offshore fixed foundation wind turbines installed at shallow depths. In [33], the non-linear behavior arising in a floating wind turbine subjected to simultaneous wind and wave loads was studied, with the aim of evaluating the structural fatigue of the floating system. In [34], a simplified model for large-scale offshore wind farms was presented, based on the simulation of the wake effects of each wind turbine and how they affect the adjacent ones.

In [35], an aero-hydro-elastic model was proposed to predict power production in the time domain. To develop the model, a floating OC3-Hywind-type wind turbine [2,3] had been chosen. The results of the study were compared with those presented in [36].

Regarding studies on marine turbines, the study in [37] is a very interesting work because it covers all the problems of the simulation of marine turbines, from the modeling of the marine currents for long periods of time to the modeling of the marine turbines applying the BEM theory. The results were compared with those obtained in [38,39]. Based on [37], a study was carried out in [40] but including an electromechanical simulator composed of an electric motor coupled to a generator, thus allowing the data obtained with the simulation to be compared with those obtained experimentally.

In [41,42], an electromechanical simulator was described, in which an electric motor was coupled to a generator and then to an active brake to study power generation and the automatic control system. In [43], the production of electrical energy in an array of marine turbines was studied using computational fluid dynamics (CFD) software, analyzing the effect of wake propagation in the adjacent turbines. In [44], a simulator—using Matlab-Simulink®—of a tidal current turbine, the drive train, and the generator was implemented.

In [45], a comparison between simulated and real data from a tidal turbine was performed. The simulation data were obtained using TidalBladed software [20], applying von Karman's model [23] for turbulent flow modeling of the marine current. Real data were obtained from Alstom Ocean Energy's 1 MW tidal turbine [46], which was deployed at the European Marine Energy Center (EMEC). In [47], the limitations of the modeling of individual marine turbines when applied to a tidal turbine farm were studied. For this, Python software developed in [48] was used. The tidal current model was obtained using the JONSWAP (Joint North Sea Wave Project) spectrum to which a necessary term was added to complete the marine current model affecting adjacent turbines in a tidal turbine farm.

In [49], a solid–fluid interaction model of a marine turbine was presented, using two turbulent flow modeling strategies: the Reynolds-Averaged Navier–Stokes (RANS) and the Large Eddy Simulation (LES) method. The fluid modeling was performed with ANSYS Fluent [16], and the results were compared with experimental data obtained in [39]. In [50], a model of tidal turbines in a water-sediment environment was presented. The turbine modeling was based on the BEM theory but correcting the values of lift coefficient (C_L) and the drag coefficient (C_D) of each airfoil. The fluid modeling was performed with ANSYS Fluent [16], and the results were compared with experimental data obtained using a wind tunnel.

Regarding floating hybrid systems, in [51], the first version of a hybrid system capable of taking advantage of both wind energy and marine currents to produce electricity with the aim of maximizing the performance of a structure installed in the sea was presented. In [52], using the proposed system presented in [51], augmentation channels were included in the marine turbines to increase their efficiency in conditions of low fluid intensity. In [53],

different proposals for hybrid systems for the extraction of energy from wind, waves, and marine currents were reviewed. In [54], a mathematical model of a hybrid system capable of extracting energy from both wind and waves was presented.

In [55], the first version of the mathematical model described in [1] and completed in this paper was presented. In that version, the mobile coordinate system was located at the center of mass of the floating system, while in [1], it was located—as shown in Figure 1—at the intersection of the floating platform with the still water level. In [56], the numerical model of a hybrid system composed of a floating wind turbine and a Wave Energy Converter (WEC) system was presented, with the aim of optimizing the size and layout of the WEC system. In [57], the control and supervision requirements of floating hybrid systems were reviewed, taking as an example those described in [1,52,55].

This paper is structured as follows: In Section 2.1, the work developed in [1] is briefly reviewed to use it as a starting point for the rest of the sections. In Section 2.2, the forces acting on the floating system are introduced. In Section 2.3, the modeling of the wind and marine currents used to calculate the different forces is presented. In Sections 2.4–2.7, the forces acting on the floating system are extensively discussed. These are, in order of appearance, the forces exerted by the mooring system, the gravitational forces, the hydrodynamic forces, and the Coriolis–centripetal forces. Next, in Section 2.8, the modeling of the turbines using the One-Dimensional theory is explained, which allows for obtaining the forces exercised by the turbines. Section 3 presents the results obtained in the performed tests, and finally, Section 4 includes the discussion and future work for this line of research.

2. Materials and Methods

2.1. Introduction to the Mathematical Model of the Floating Hybrid System

The first task for the modeling of a floating hybrid system such as the one exposed in [1]—and which appears in Figure 1—could be considered the mechanical design of all the elements that compose it, using solid mechanical design software, in our case, Solid Works®. As indicated in the Introduction, this task constitutes the data preprocessing that provides FHYGSYS with information on the mechanical characteristics of the physical system whose behavior is going to be simulated (see Figure 2). The mechanical characteristics—or inertial data—obtained in this way are the mass, the center of mass, and the inertia tensor, formed by the moments and products of inertia of each element (all these data appear in Appendix A of [1]).

From the mechanical characteristics of each element, the global inertial data—mass (m_{FS}); center of mass (CoM); and inertia tensor, composed of moments (I_{xx}, I_{yy}, I_{zz}) and products of inertia (I_{xy}, I_{yz}, I_{zx})—of the floating hybrid system are obtained. This process was explained in detail in [1]. Table 2 shows the global values of the inertial properties—extracted from Appendix A of [1]—applied to FHYGSYS for the dynamics processing of the floating hybrid system shown in Figure 1. These data are inserted into FHYGSYS through the rigid body matrix (M_{RB}), which is shown in Equation (1), extracted from [1].

$$M_{RB} = \begin{bmatrix} m_{FS} & 0 & 0 & 0 & m_{FS} \cdot z_{CoM} & -m_{FS} \cdot y_{CoM} \\ 0 & m_{FS} & 0 & -m_{FS} \cdot z_{CoM} & 0 & m_{FS} \cdot x_{CoM} \\ 0 & 0 & m_{FS} & m_{FS} \cdot y_{CoM} & -m_{FS} \cdot x_{CoM} & 0 \\ 0 & -m_{FS} \cdot z_{CoM} & m_{FS} \cdot y_{CoM} & I_{xx} & -I_{xy} & -I_{zx} \\ m_{FS} \cdot z_{CoM} & 0 & -m_{FS} \cdot x_{CoM} & -I_{xy} & I_{yy} & -I_{yz} \\ -m_{FS} \cdot y_{CoM} & m_{FS} \cdot x_{CoM} & 0 & -I_{zx} & -I_{yz} & I_{zz} \end{bmatrix} \tag{1}$$

This methodology is a fast and effective way to model mechanical systems and is extensible to systems of a different nature; for example, it can be used in control engineering for modeling mechanical systems.

Processing of the added mass discussed in [1]—interpreting this as a particular volume of fluid particles that are accelerated with the submerged part of the floating system [58]—is performed in a similar way to inertial processing. In this case, the inertial data are also necessary, but the volume of water displaced by the submerged and partially submerged

parts of the floating system are used, that is, the mass of these volumes, their centers of buoyancy, and their inertia tensors (these data appear in Appendix A of [1]).

Table 2. Global inertial properties of the floating hybrid system (for $t = 0$).

Element	Floating Hybrid System
Mass (kg)	8,138,259
Ixx (kg·m^2)	67,434,701,761 [1]
Iyy (kg·m^2)	67,398,679,463 [1]
Izz (kg·m^2)	144,576,159 [1]
Ixy (kg·m^2)	7.56248 [1]
Iyz (kg·m^2)	−75.8696 [1]
Izx (kg·m^2)	−12,699,829 [1]
Center of Mass (m)	(−0.0172219, 0, −76.6108) [2]

[1] Calculated at origin of the mobile coordinate system. [2] Expressed in the mobile coordinate system.

The totally submerged elements are the blades, the hubs, and the support of the marine current turbines. These are treated as if they were some more solid elements, that is, their mechanical design is carried out—in Solid Works®—considering them as compact solids and using the density of sea water for the design. In Figure 2, these elements are represented in the preprocessed data block together with the inertial data.

The partially submerged element is the floating platform, and its submerged volume varies as a function of time, so this calculation is performed using FHYGSYS at each instant of time while the simulation is running. This implies that, at each instant of time, a new mass, a new center of buoyancy, and a new inertia tensor of the submerged volume of the floating platform are obtained.

In the same way as in the previous case, from the mechanical characteristics of each element, the global inertial data—mass of the submerged volume ($m_{SUM}(t)$); center of buoyancy (*CoB*); and inertia tensor, composed of moments ($I_{xx(SUM)}$, $I_{yy(SUM)}$, $I_{zz(SUM)}$) and products of inertia ($I_{xy(SUM)}$, $I_{yz(SUM)}$, $I_{zx(SUM)}$)—of all submerged parts of the floating hybrid system are obtained. These values—extracted from Appendix A of [1]—appear in Table 3.

Table 3. Global inertial properties of the floating hybrid system to calculate added mass (for $t = 0$).

Element	Floating Hybrid System
Volume (m^3)	8100.42
Mass (kg)	8,302,931
Ixx$_{(SUM)}$ (kg·m^2)	41,051,048,910 [1]
Iyy$_{(SUM)}$ (kg·m^2)	41,036,448,653 [1]
Izz$_{(SUM)}$ (kg·m^2)	103,989,376 [1]
Ixy$_{(SUM)}$ (kg·m^2)	0 [1]
Iyz$_{(SUM)}$ (kg·m^2)	0 [1]
Izx$_{(SUM)}$ (kg·m^2)	−60,847.1 [1]
Center of Buoyancy (m)	(0.000366417, 0, −61.6897) [2]

[1] Calculated at origin of the mobile coordinate system. [2] Expressed in the mobile coordinate system.

As in the previous case, these data are applied to FHYGSYS by means of a matrix, in this case, the added mass matrix (M_{AM}), which appears in Equation (32) of [1]. To obtain this matrix, the coefficients—which depend on the shape of the submerged volume—that correct the values of the M_{AM} matrix must be calculated. In Equation (32) of [1], some elements appear multiplied by the mass of the submerged volume ($m_{SUM}(t)$). As in Equations (26)–(28) of [1], the mass of the submerged volume ($m_{SUM}(t)$) must be multiplied by the coefficients as a function of α_0, β_0, and γ_0. For this reason, Equation (32) of [1] should be interpreted as shown in Equation (2).

$$M_{AM} = - \begin{bmatrix} X_{\dot{u}} & 0 & 0 & 0 & Y_{\dot{v}} \cdot z_{CoB} & -Z_{\dot{w}} \cdot y_{CoB} \\ 0 & Y_{\dot{v}} & 0 & -X_{\dot{u}} \cdot z_{CoB} & 0 & Z_{\dot{w}} \cdot x_{CoB} \\ 0 & 0 & Z_{\dot{w}} & X_{\dot{u}} \cdot y_{CoB} & -Y_{\dot{v}} \cdot x_{CoB} & 0 \\ 0 & -Y_{\dot{v}} \cdot z_{CoB} & Z_{\dot{w}} \cdot y_{CoB} & K_{\dot{p}} & -I_{xy(SUM)} & -I_{zx(SUM)} \\ X_{\dot{u}} \cdot z_{CoB} & 0 & -Z_{\dot{w}} \cdot x_{CoB} & -I_{xy(SUM)} & M_{\dot{q}} & -I_{yz(SUM)} \\ -X_{\dot{u}} \cdot y_{CoB} & Y_{\dot{v}} \cdot x_{CoB} & 0 & -I_{zx(SUM)} & -I_{yz(SUM)} & N_{\dot{r}} \end{bmatrix} \quad (2)$$

Although all these processes were explained in detail in [1], given its importance, for greater clarity, an example of calculating the M_{AM} matrix for instant $t = 0$ has been included in Appendix A of this work.

As indicated in the Introduction, in the first part of this work [1], the mathematical modeling of kinematics and dynamics were explained. The computation of the kinematics was based on the use of homogeneous transformation matrices [59], while the computation of the dynamics was based on the application of Newton's second law for a floating system, as indicated in [60]. To apply the dynamics, it is necessary to know the inertial data and the added mass of the floating system, as well as the resultant forces that act on it (see Figure 2). Both the obtained inertial data and the added mass have been reviewed in previous paragraphs and are explained in depth in [1]. To complete the exposition of our mathematical model, it is necessary to explain in detail how to obtain the resultant forces that act on the floating system. In [1], a brief review of all of them was provided, and in the following sections, the details are presented.

2.2. Influential Forces on the Floating Hybrid System

The calculation of the forces acting on the floating hybrid system is carried out vectorially; this implies that vectors must be used to represent both the forces and the moments that act on it. As indicated in [1], for the processing of the mathematical model, two main coordinate systems were used, a fixed one that is considered inertial and a mobile one that is fixed to the floating system and therefore accelerates with it (see Figure 3).
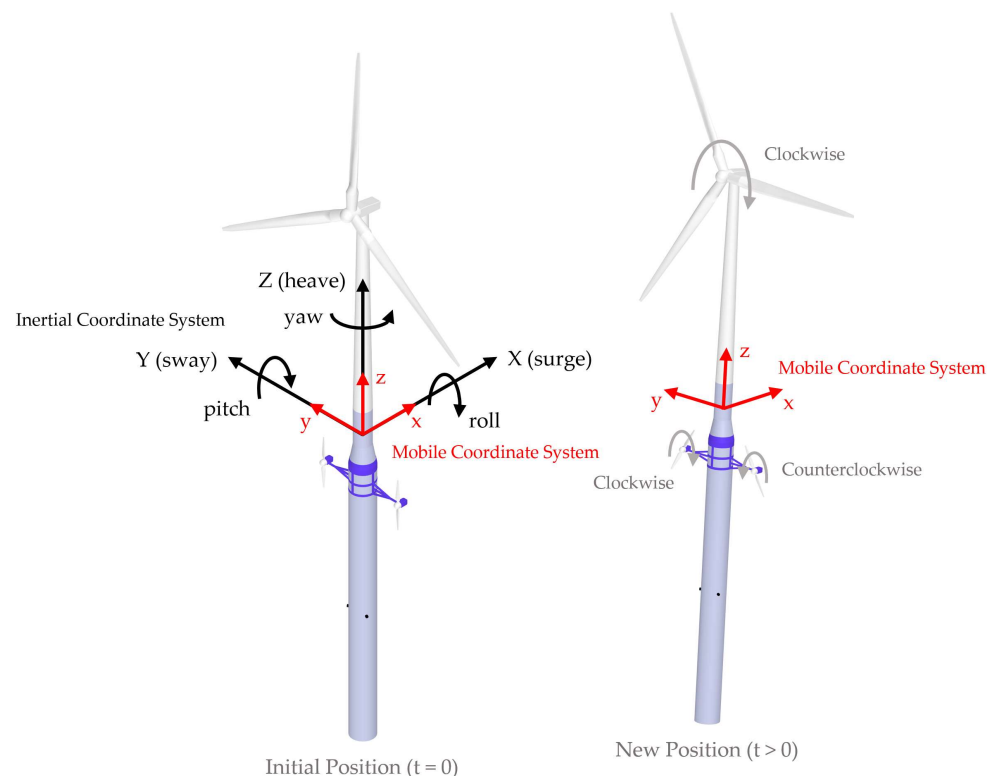

Figure 3. Degrees of freedom of the floating system and inertial and mobile coordinate systems.

In Figure 3, the inertial and mobile coordinate systems can be seen at two different instants of time; in the initial position, both coordinate systems are coincident.

Applying Newton's second law to a floating system, Equation (3) is obtained, which allows for solving the dynamics in the mathematical model and calculating the acceleration generated in the system. Starting from this acceleration, in [1], we explained in detail how the new position of the system is calculated. The equation thus represented is extracted from [1], in which the M_{RB} and M_{AM} matrices appear related to the resultant forces acting on the floating hybrid system expressed in the mobile coordinate system $\left(\overrightarrow{F}_{j(BODY)}^{TOTAL} \right)$.

$$\overrightarrow{av}_{j(BODY)} = (M_{RB} + M_{AM})^{-1} \cdot \overrightarrow{F}_{j(BODY)}^{TOTAL} = (M_{RB} + M_{AM})^{-1} \cdot \left[F_x F_y F_z M_x M_y M_z \right]^T \quad (3)$$

The resultant forces acting on the floating system is made up of many interactions. At a first level, this resultant could be subdivided as shown in Figure 2 into five groups of force and moment vectors. This subdivision corresponds to the one presented in Equation (4), extracted from [1].

$$\overrightarrow{F}_{j(BODY)}^{TOTAL} = \overrightarrow{F}_{j(BODY)}^{WIND\ TURBINE} + \overrightarrow{F}_{j(BODY)}^{GRAVITY} + \overrightarrow{F}_{j(BODY)}^{HYDRODYNAMICS} + \overrightarrow{F}_{j(BODY)}^{MOORING\ SYSTEM} + \overrightarrow{F}_{j(BODY)}^{CORIOLIS} \quad (4)$$

As indicated in [1], the calculation of the resultant forces is based on the fact that those forces change very little between instants of time; this allows for the application of the superposition theorem [61], calculating the forces separately and adding them to obtain the resultant forces acting on the floating hybrid system. Dynamics processing is easier if the resultant forces are expressed in the mobile coordinate system; therefore, each of the forces must also be expressed in this coordinate system. In [1] and in this paper, this procedure was adopted for simplicity and coherence with the methodology explained in [60].

The general criteria applied for the calculation of each one of the forces is the following: first, the corresponding force vector is obtained in the mobile coordinate system; second, the point of application of the force vector on the floating system is deduced; and finally, the force vector is translated from this point to the origin of the mobile coordinate system, thus obtaining the moment vector at the origin of this system caused by the force vector. The theoretical foundations that support this criterion are widely used in mechanics and can be found in [62–64]. Table 4 shows some common constants used to calculate the different forces.

Table 4. Simulation environment constants.

Property	Value	Symbol
Gravity Acceleration [1]	9.80665 m/s^2	g
Density of Air [1]	1.225 kg/m^3	ρ_{AIR}
Density of Seawater [1]	1025 kg/m^3	$\rho_{SEA\ WATER}$
Water Depth [2]	320 m	d_{WATER}

[1] Value used by FASTv8. [2] Source [2].

Next, the modeling of the acting fluids on the floating hybrid system is described: these are the wind and the marine currents. These models are subsequently used in the following sections to obtain some of the force vectors acting on the floating system. These forces could modify moving parts—for example, the force of the wind rotates the wind turbine and the force of the marine currents rotates the marine current turbines—or generate thrusts such as marine currents on the floating platform.

2.3. Modeling of the Wind and the Marine Currents Acting on the Floating Hybrid System

2.3.1. Wind Modeling

The modeling of the wind action used in [1] and in this work is unidirectional and steady—although more complete models could also be used in FHYGSYS, such as those exposed in [31,35]; this model has been chosen for simplicity and because it facilitates the validation process of the FHYGSYS tool. In this way, to define the wind action that will be used in a certain simulation, only the wind speed (V_{W-REF}) and its direction (δ) must be indicated. These two values are constant for a given simulation.

The wind speed (V_{W-REF}) is the magnitude of the wind velocity vector at the reference height (z_{REF}). This reference height is 90 m above the still water level—the height of the hub of the wind turbine in the initial position [2,3]—following the same criteria used in [7,65].

Taking into account that the wind speed depends on the height (h), to calculate the magnitude ($V_{WIND}(h)$) of the wind velocity vector at a certain height ($z_{WIND}(t) > 0$), Equation (5)—extracted from [65]—is used, where (α) is the power law exponent, which has a value of 1/7 for normal wind conditions and 0.11 for extreme conditions [65]. In [1] and in this work, all the simulations have been carried out considering normal wind conditions, so the power law exponent (α) always takes the value 1/7.

$$V_{WIND}(h) = V_{W-REF} \cdot \left(\frac{z_{WIND}(t)}{z_{REF}} \right)^{\alpha} \tag{5}$$

The orientation of the wind velocity vector is always parallel to the X-Y plane of the inertial coordinate system. The direction (δ) is the angle of rotation of the wind velocity vector around the Z axis of the inertial coordinate system with which a vector field is obtained (see Figure 4), whose vectors are also parallel to the X-Y plane of the inertial coordinate system, rotated by a certain angle (δ) around the Z axis. In this way, a uniform-wind-shear-type velocity vector field is obtained as described in [66].

To obtain the wind velocity vectors ($\vec{v}_{WIND(INERTIAL)}(h)$) of the vector field rotated by the corresponding angle (δ), Equation (6) is applied, thus calculating the wind velocity vectors expressed in the inertial coordinate system.

$$\vec{v}_{WIND(INERTIAL)}(h) = V_{WIND}(h) \cdot \begin{bmatrix} \cos \delta & -\sin \delta & 0 \\ \sin \delta & \cos \delta & 0 \\ 0 & 0 & 1 \end{bmatrix} \cdot \begin{bmatrix} 1 \\ 0 \\ 0 \end{bmatrix} \tag{6}$$

When this vector field interacts with the floating hybrid system, it must be considered that the floating system moves through the water due to the forces acting on it. Considering this issue, one more calculation must be made. First, the velocity vector ($\vec{v}_{point(INERTIAL)}(t)$) of the floating system at the calculation point must be obtained. This is performed by differentiating with respect to time—applying the expressions from Appendix C of [1]—the position of this point expressed in the inertial coordinate system ($\vec{p}_{point(INERTIAL)}(t)$) (Equation (7)). In this case, the Z coordinate of the calculation point ($\vec{p}_{point(INERTIAL)}(t)$) corresponds to the height ($z_{WIND}(t)$) used in Equation (5).

$$\vec{v}_{point(INERTIAL)}(t) = \frac{d}{dt} \vec{p}_{point(INERTIAL)}(t) \tag{7}$$

Finally, the effective wind velocity vector ($\vec{v}_{EFF-WIND(INERTIAL)}(h,t)$)—which acts on a certain point of the floating system—is obtained by adding the velocity vector ($\vec{v}_{point(INERTIAL)}(t)$) of this calculation point to the wind velocity vector ($\vec{v}_{WIND(INERTIAL)}(h)$) at the height at which the point is located (Equation (8)).

$$\vec{v}_{EFF-WIND(INERTIAL)}(h,t) = \vec{v}_{WIND(INERTIAL)}(h) + \vec{v}_{point(INERTIAL)}(t) \tag{8}$$
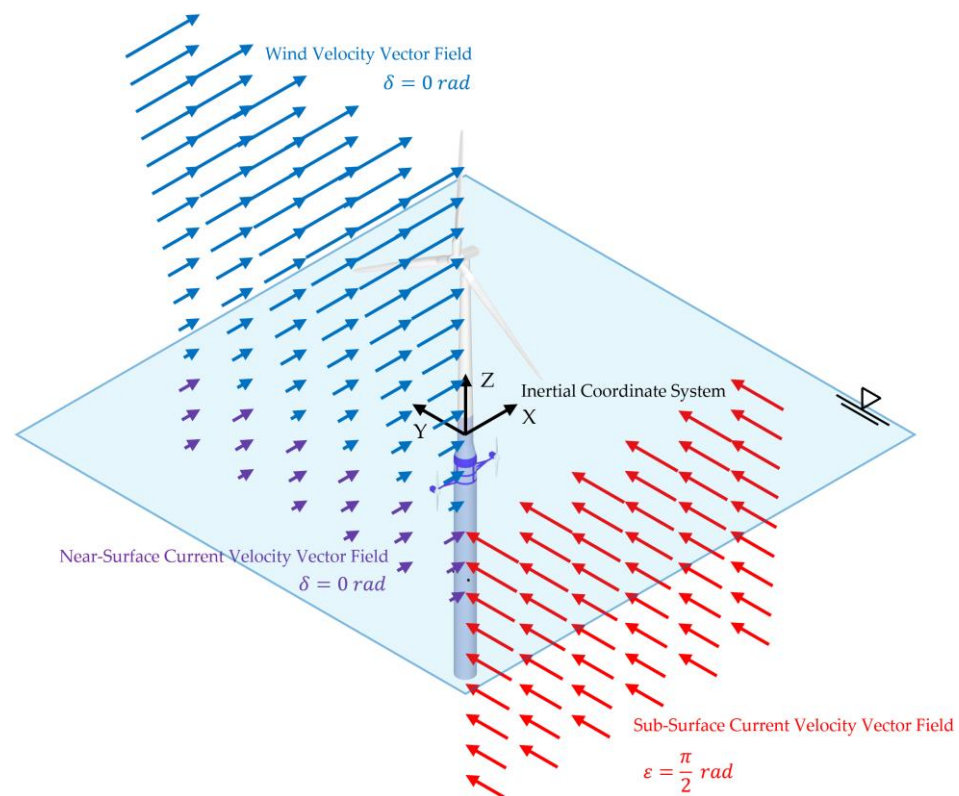
Figure 4. Wind, near-surface current, and sub-surface current velocity vector fields.

2.3.2. Sub-Surface Current Modeling

The modeling of the sub-surface current action used in [1] and in this work is also unidirectional and steady. So, the same criteria described for modeling the wind—explained in the previous section—are used to model the sub-surface current. In this case, to define the current action that will be used in a certain simulation, the current speed (V_{SWL}) and its direction (ε) must also be indicated. These two values are also constant for a given simulation.

Analogously to the previous case, the current velocity (V_{SWL}) is the magnitude of the sub-surface current velocity vector at the reference depth, following the criteria of [65] the reference depth is at the still water level ($z_{SSCUR}(t) = 0$).

In this case, the current speed depends on the depth (*h*), to calculate the magnitude ($V_{SSCUR}(h)$) of the current velocity vector at a certain depth ($z_{SSCUR}(t) \leq 0$); Equation (9)—extracted from [65]—is used, where (α) is the power law exponent and takes the same value exposed in the previous section, 1/7 for normal current conditions [65]. To use Equation (9), another piece of information that must be known is the total water depth (d_{WATER}) at which the simulation is performed. The one indicated in [2]—whose value is 320 m—has been chosen for all the simulations (see Table 4).

$$V_{SSCUR}(h) = V_{SWL} \cdot \left(\frac{z_{SSCUR}(t) + d_{WATER}}{d_{WATER}} \right)^{\alpha} \tag{9}$$

The sub-surface current velocity vectors also constitute a vector field whose vectors are always parallel to the X-Y plane of the inertial coordinate system and rotated by a certain angle (ε) around the Z axis of the inertial coordinate system (see Figure 4). In [65], it is indicated that in general, it may be acceptable to assume that the sub-surface currents are aligned with the wave direction.

As in the previous case, to obtain the sub-surface current velocity vectors ($\vec{v}_{SSCUR(INERTIAL)}(h)$) of the vector field rotated by the corresponding angle (ε), Equation (10)

is applied, thus also calculating the sub-surface current velocity vectors expressed in the inertial coordinate system.

$$\vec{v}_{SSCUR(INERTIAL)}(h) = V_{SSCUR}(h) \cdot \begin{bmatrix} \cos\varepsilon & -\sin\varepsilon & 0 \\ \sin\varepsilon & \cos\varepsilon & 0 \\ 0 & 0 & 1 \end{bmatrix} \cdot \begin{bmatrix} 1 \\ 0 \\ 0 \end{bmatrix} \qquad (10)$$

Equivalent to the previous case, to obtain the effective current velocity vector ($\vec{v}_{EFF-SSCURR(INERTIAL)}(h,t)$)—which acts on a certain point of the floating system—Equation (11) is applied.

$$\vec{v}_{EFF-SSCURR(INERTIAL)}(h,t) = \vec{v}_{SSCUR(INERTIAL)}(h) + \vec{v}_{point(INERTIAL)}(t) \qquad (11)$$

The velocity vector ($\vec{v}_{point(INERTIAL)}(t)$) of the floating system at the calculation point is obtained in the same way using Equation (7). In this case, the Z coordinate of the calculation point ($\vec{p}_{point(INERTIAL)}(t)$) also corresponds to the depth ($z_{SSCUR}(t)$) used in Equation (9).

2.3.3. Near-Surface Current Modeling

Unlike the sub-surface current, the near-surface current arises exclusively from the action of the wind, so its orientation is the same as that of the wind. This type of current also constitutes a vector field whose vectors are always parallel to the X-Y plane of the inertial coordinate system and rotated the same angle (δ) as the wind around the Z axis of the inertial coordinate system (see Figure 4).

Since the near-surface current appears from the wind, the magnitude ($V_{NSCUR}(h)$) of the near-surface current velocity vector at the reference depth—this is the same as in the case of the sub-surface current, at the still water level ($z_{NSCUR}(t) = 0$)—is obtained by applying the following reasoning.

According to the criterion of [65], from the reference wind speed (V_{W-REF}), Equation (5) is applied for a height of 10 m ($z_{WIND}(t) = 10$), yielding $V_{WIND}(10)$. The effects of the near-surface current are considered to disappear from a depth of 20 m [65], so to obtain the magnitude ($V_{NSCUR}(h)$) of the velocity vector of this current, Equation (12) is applied—extracted from [65]—for the desired depth ($0 \geq z_{NSCUR}(t) \geq -20$).

$$V_{NSCUR}(h) = 0.01 \cdot V_{WIND}(10) \cdot \left(1 + \frac{z_{NSCUR}(t)}{20}\right) \qquad (12)$$

In the same way as in the previous cases, to obtain the near-surface current velocity vectors ($\vec{v}_{NSCUR(INERTIAL)}(h)$) of the vector field rotated by the corresponding angle (δ), Equation (13) is used, thus also calculating the near-surface current velocity vectors expressed in the inertial coordinate system.

$$\vec{v}_{NSCUR(INERTIAL)}(h) = V_{NSCUR}(h) \cdot \begin{bmatrix} \cos\delta & -\sin\delta & 0 \\ \sin\delta & \cos\delta & 0 \\ 0 & 0 & 1 \end{bmatrix} \cdot \begin{bmatrix} 1 \\ 0 \\ 0 \end{bmatrix} \qquad (13)$$

As in the previous cases, to obtain the effective current velocity vector ($\vec{v}_{EFF-NSCURR(INERTIAL)}(h,t)$)—which acts on a certain point of the floating system—Equation (14) is applied.

$$\vec{v}_{EFF-NSCURR(INERTIAL)}(h,t) = \vec{v}_{NSCUR(INERTIAL)}(h) + \vec{v}_{point(INERTIAL)}(t) \qquad (14)$$

The velocity vector ($\vec{v}_{point(INERTIAL)}(t)$) of the floating system at the calculation point is obtained in the same way using Equation (7). In this case, the Z coordinate of the

calculation point ($\vec{p}_{point(INERTIAL)}(t)$) also corresponds to the depth ($z_{NSCUR}(t)$) used in Equation (12).

Although FHYGSYS offers this possibility, the near-surface current is not used neither in [1] nor in this work to carry out simulations, since its effect is small.

2.4. Vector of Mooring System Forces

The mooring system is responsible for avoiding the drift of the floating hybrid system, retaining it as close as possible to its initial position. Following the approach of [2], it is composed of three mooring lines arranged at 120 degrees—in the initial position—around the Z axis of the inertial coordinate system (see Figure 5).
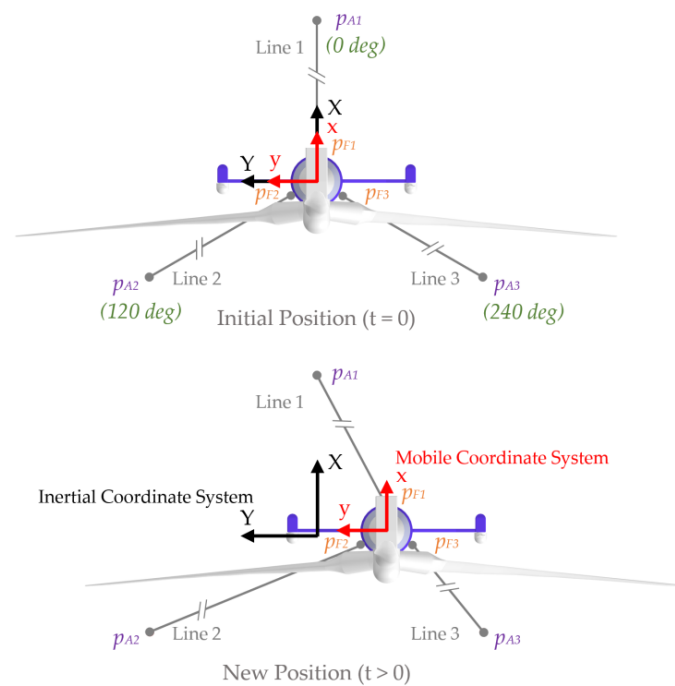

Figure 5. Position of the significant points of the mooring system at two instants of time.

Table 5 shows the position of the points of the fairleads attached to the floating platform and the anchors fixed on the seabed. These values are expressed in the inertial coordinate system, correspond to the initial position of the floating system (see Figure 5), and are deduced from the information provided by [2]. The assignment of the line numbers corresponds to the numbering indicated in [1] and in Figures 1 and 5.

Table 5. Significant values of the mooring system in the initial position.

Element	Symbol	Position (m)
Mooring Line Fairlead 1	p_{F1}	$(5.2, 0, -70)$
Mooring Line Anchor 1	p_{A1}	$(853.87, 0, -320)$
Yaw angle with respect to inertial X axis	$\varphi_{Line\ 1}$	0 deg
Mooring Line Fairlead 2	p_{F2}	$(-2.6, 4.503, -70)$
Mooring Line Anchor 2	p_{A2}	$(-426.9, 739.5, -320)$
Yaw angle with respect to inertial X axis	$\varphi_{Line\ 2}$	120 deg
Mooring Line Fairlead 3	p_{F3}	$(-2.6, -4.503, -70)$
Mooring Line Anchor 2	p_{A3}	$(-426.9, -739.5, -320)$
Yaw angle with respect to inertial X axis	$\varphi_{Line\ 3}$	240 deg

The fairleads move attached to the floating platform, while the anchors always remain fixed on the seabed. This implies—as shown in Figure 5—that the position of the anchors

remains constant with respect to the inertial coordinate system, but not with respect to the mobile coordinate system and, vice versa, the position of the fairleads varies with respect to the inertial coordinate system but not with respect to the mobile coordinate system.

In [2], three different models of the mooring system are proposed; among them, a non-linear model of an individual mooring line has been chosen. The characteristics of this type of modeling are extracted from [61,67]. In this way, the force and moment vector of each mooring line is calculated separately, and then, these vectors are added using Equation (15), thus obtaining the total force vector of the entire mooring system.

$$\overset{\rightarrow MOORING\ SYSTEM}{F_{j(BODY)}}(t) = \overset{\rightarrow LINE\ 1}{F_{j(BODY)}}(t) + \overset{\rightarrow LINE\ 2}{F_{j(BODY)}}(t) + \overset{\rightarrow LINE\ 3}{F_{j(BODY)}}(t) \tag{15}$$

Applying the criteria explained in [61], the first task to obtain the vector of forces of the mooring lines is to express the points of the fairleads (p_{Fi}) in the anchor coordinate system (see Figure 6b). This task is carried out by expressing, as a previous step, these points in an intermediate anchor coordinate system, whose three axes are parallel to those of the inertial coordinate system and whose origins are exactly at the anchor position of each one of the mooring lines (see Figure 6a).
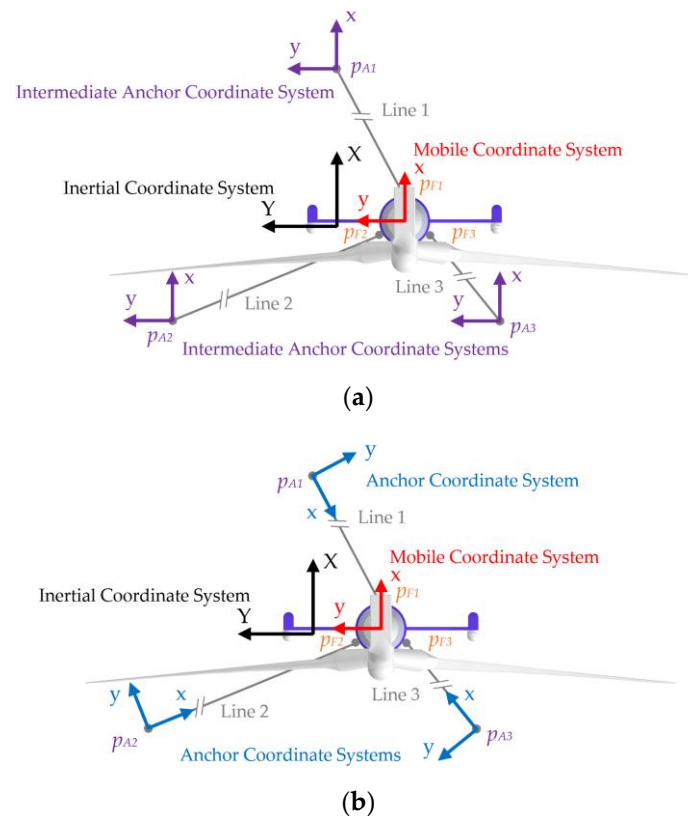

(a)

(b)

Figure 6. Location of the auxiliary coordinate systems of the mooring lines: (**a**) location of the three intermediate anchor coordinate systems; (**b**) location of the three anchor coordinate systems.

As a second step, the angle ($\varphi_{anchorCS\ i}(t)$) that each of these three intermediate anchor coordinate systems must be rotated—around its corresponding Z axis—is calculated. Thus, each of the X axes are directed toward the corresponding fairlead points. In this way, the anchor coordinate systems are correctly located for the calculations (see Figure 6b).

Expressing the above in a mathematical way, for the calculation in a mooring line, Equations (16) and (17) are applied to express—in the intermediate anchor coordinate

system—the position vector of the fairlead in the initial position ($\vec{p}_{FAi(INTER)(t=0)}$) and in the position of a subsequent instant of time ($\vec{p}_{FAi(INTER)(t>0)}(t)$).

$$\vec{p}_{FAi(INTER)(t=0)} = \left[p_{Fi(INERTIAL)(t=0)} - p_{Ai(INERTIAL)} \right]^T \cdot \begin{bmatrix} 1 & 0 & 0 \\ 0 & 1 & 0 \\ 0 & 0 & 0 \end{bmatrix} \quad (16)$$

$$\vec{p}_{FAi(INTER)(t>0)}(t) = \left[p_{Fi(INERTIAL)(t>0)}(t) - p_{Ai(INERTIAL)} \right]^T \cdot \begin{bmatrix} 1 & 0 & 0 \\ 0 & 1 & 0 \\ 0 & 0 & 0 \end{bmatrix} \quad (17)$$

Since the angle ($\varphi_{anchorCS\ i}(t)$) to be calculated is an angle rotated around the Z axes of the intermediate anchor coordinate systems—the X-Y plane of an intermediate anchor coordinate system and that of an anchor coordinate system is always parallel to the X-Y plane of the inertial coordinate system—the Z coordinate in Equations (16) and (17) must be zero.

Afterwards, performing the cross product ($\vec{cross}_{FAi(INTER)}(t)$)—through Equation (18)— of the position vectors $\vec{p}_{FAi(INTER)(t=0)}$ and $\vec{p}_{FAi(INTER)(t>0)}(t)$, the angle ($\varphi_{anchor\ i}(t)$) formed by these two position vectors is obtained using Equation (19). These equations are widely used in vector calculus and can be found in [68].

$$\vec{cross}_{FAi(INTER)}(t) = \vec{p}_{FAi(INTER)(t=0)} \times \vec{p}_{FAi(INTER)(t>0)}(t) = \begin{vmatrix} \vec{i} & \vec{j} & \vec{k} \\ x_{pFAi(INTER)(t=0)} & y_{pFAi(INTER)(t=0)} & 0 \\ x_{pFAi(INTER)(t>0)} & y_{pFAi(INTER)(t>0)} & 0 \end{vmatrix} \quad (18)$$

$$\varphi_{anchor\ i}(t) = \text{asin}\left(\frac{\left| \vec{cross}_{FAi(INTER)}(t) \right|}{\left| \vec{p}_{FAi(INTER)(t=0)} \right| \cdot \left| \vec{p}_{FAi(INTER)(t>0)}(t) \right|} \right) \quad (19)$$

Figure 7 shows the anchor coordinate system in two instants of time, which allows us to observe the angle $\varphi_{anchor\ 3}$, formed by the anchor coordinate system—of mooring line 3—at the initial instant ($t = 0$) and a subsequent instant of time ($t > 0$).
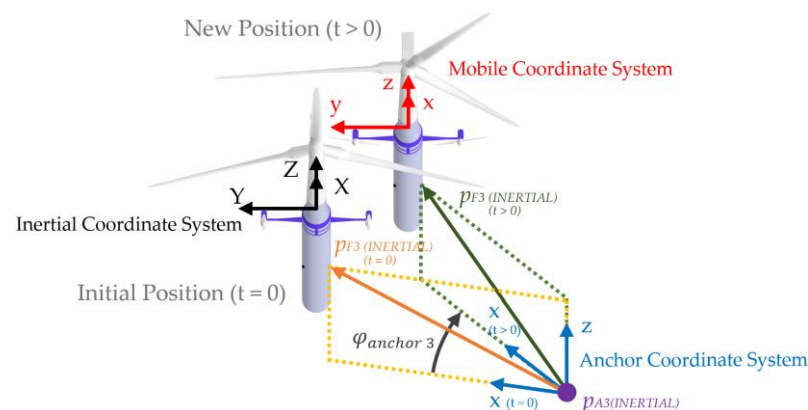

Figure 7. Representation of the anchor coordinate system at two instants of time.

The sign of the Z component of $\vec{cross}_{FAi(INTER)}(t)$ determines the sign of the angle $\varphi_{anchor\ i}(t)$; therefore, to calculate the rotated angle of the anchor coordinate system with respect to the intermediate anchor coordinate system ($\varphi_{anchorCS\ i}(t)$), Equation (20) or (21), depending on the case, should be used. The $\varphi_{Line\ i}$ angle is the corresponding one—for each

mooring line—which appears in Table 5. In these two equations, the angles are represented in radians.

$$\varphi_{anchorCS\,i}(t)\Big|_{z_{\overrightarrow{crossFAi(INTER)}}\geq 0} = \varphi_{anchor\,i}(t) + \varphi_{Line\,i} + \pi \tag{20}$$

$$\varphi_{anchorCS\,i}(t)\Big|_{z_{\overrightarrow{crossFAi(INTER)}}<0} = -\varphi_{anchor\,i}(t) + \varphi_{Line\,i} + \pi \tag{21}$$

Once the angle $\varphi_{anchorCS\,i}(t)$ has been calculated, the fairlead point $(p_{Fi(INERTIAL)}(t))$—of one of the mooring lines represented in the inertial coordinate system—is obtained but represented in the anchor coordinate system $(p_{Fi(ANCHOR)}(t))$, using Equations (22) and (23). Equation (22) yields the homogeneous transformation matrix $(M_{HTi\,ANCHOR}^{INERTIAL})$ that allows for the change between the two coordinate systems.

$$M_{HTi\,ANCHOR}^{INERTIAL}(t) = M_{HTi\,ANCHOR}^{INERTIAL} = \begin{bmatrix} 1 & 0 & 0 & p_{Ai(INERTIAL)x} \\ 0 & 1 & 0 & p_{Ai(INERTIAL)y} \\ 0 & 0 & 1 & p_{Ai(INERTIAL)z} \\ 0 & 0 & 0 & 1 \end{bmatrix} \cdot \begin{bmatrix} \cos\varphi_{anchorCS\,i} & -\sin\varphi_{anchorCS\,i} & 0 & 0 \\ \sin\varphi_{anchorCS\,i} & \cos\varphi_{anchorCS\,i} & 0 & 0 \\ 0 & 0 & 1 & 0 \\ 0 & 0 & 0 & 1 \end{bmatrix} \tag{22}$$

$$p_{Fi(ANCHOR)}(t) = \left(M_{HTi\,ANCHOR}^{INERTIAL}\right)^{-1} \cdot p_{Fi(INERTIAL)}(t) = \begin{bmatrix} x_{Fi} \\ y_{Fi} \\ z_{Fi} \\ 1 \end{bmatrix} = \begin{bmatrix} x_{Fi} \\ 0 \\ z_{Fi} \\ 1 \end{bmatrix} \tag{23}$$

To facilitate the following calculations and for consistency with [61], the X and Z components of $p_{Fi(ANCHOR)}(t)$ are assigned the symbols x_{Fi} and z_{Fi}, respectively (see Equation (23)). The y_{Fi} component always takes the value zero because each of the X axes of the anchor coordinate systems are directed toward the corresponding fairlead points.

The main characteristics that define the behavior of the mooring system are extracted from [2] and are shown in Table 6. These values—together with the x_{Fi} and z_{Fi} components—allow the calculation of the force vector of each mooring line.

Table 6. Mooring system properties.

Property	Value	Symbol
Unstretched Mooring Line Length [1]	902.2 m	L
Equivalent Mooring Line Extensional Stiffness [1]	384,243 kN	EA
Cable-seabed friction coefficient [2]	0.001	C_B
Equivalent Mooring Line Mass Density [1]	77.7066 kg/m	m_{Line}
Mooring Line Diameter [1]	0.09 m	D_C
Additional Yaw Spring Stiffness [1]	98,340 kN·m/rad	$AddYS$

[1] Source [2]. [2] Value used by FASTv8.

The modeling of the mooring lines is based on the mathematical representation of the catenary arcs that draw each one of them. Before presenting these equations, it is important—as also explained in [61,67]—to preprocess some data to simplify them.

Specifically, based on the information shown in Tables 4 and 6, the apparent weight of the mooring line in fluid per unit length (w_L) is obtained using Equation (24) and the unstretched portion of the mooring line resting on the seabed (L_{Bi}) using Equation (25). Both equations represented in this way are taken from [61].

$$w_L = \left(m_{Line} - \rho_{SEAWATER} \cdot \frac{\pi \cdot D_C^2}{4}\right) \cdot g \tag{24}$$

$$L_{Bi} = L - \frac{V_{Fi}}{w_L} \tag{25}$$

The force vector of each mooring line ($F_{Line\ i}$) has two components: one horizontal (H_{Fi}) and one vertical (V_{Fi}); the latter appears in Equation (25). The force vectors of lines 2 and 3, as well as their horizontal and vertical components, are shown in Figure 8.
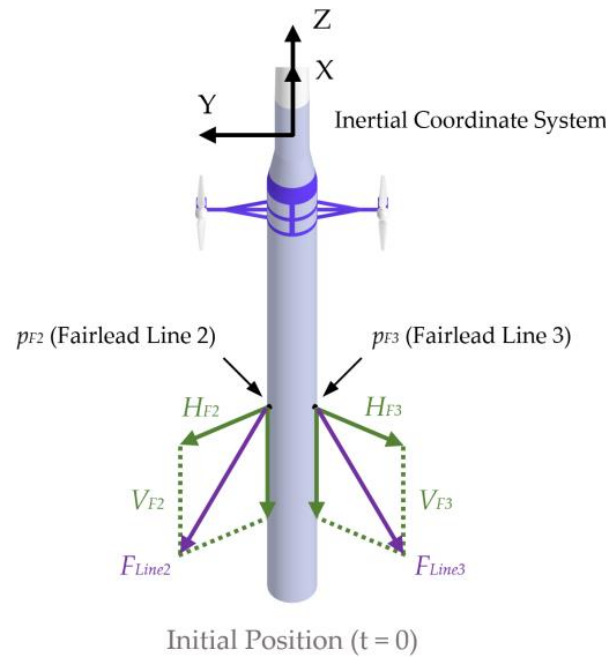

Figure 8. Mooring line force vectors and their points of application.

The next step is to calculate the horizontal (H_{Fi}) and vertical (V_{Fi}) components of the force vector ($F_{Line\ i}$) of each mooring line, for which a system of two equations in two unknowns is used. When a portion of the mooring line adjacent to the anchor rests on the seabed ($L_{Bi} > 0$), Equations (26) and (27) are applied. Equation (26) is extracted from [61] and Equation (27) is extracted from [67].

$$x_{Fi}(H_{Fi}, V_{Fi}) = L_{Bi} + \frac{H_{Fi}}{w_L} \cdot \ln\left[\frac{V_{Fi}}{H_{Fi}} + \sqrt{1 + \left(\frac{V_{Fi}}{H_{Fi}}\right)^2}\right] + \frac{H_{Fi} \cdot L}{EA} + \frac{C_B \cdot w_L}{2 \cdot EA} \cdot \left[\left(L_{Bi} - \frac{H_{Fi}}{C_B \cdot w_L}\right) \cdot MAX\left(L_{Bi} - \frac{H_{Fi}}{C_B \cdot w_L}, 0\right) - L_{Bi}^2\right] \tag{26}$$

$$z_{Fi}(H_{Fi}, V_{Fi}) = \frac{H_{Fi}}{w_L} \cdot \left[\sqrt{1 + \left(\frac{V_{Fi}}{H_{Fi}}\right)^2} - 1\right] + \frac{V_{Fi}^2}{2 \cdot EA \cdot w_L} \tag{27}$$

When no portion of the line rests on the seabed ($L_{Bi} \leq 0$), Equations (28) and (29) are used, both extracted from [61].

$$x_{Fi}(H_{Fi}, V_{Fi}) = \frac{H_{Fi} \cdot L}{EA} + \frac{H_{Fi}}{w_L} \cdot \left\{\ln\left[\frac{V_{Fi}}{H_{Fi}} + \sqrt{1 + \left(\frac{V_{Fi}}{H_{Fi}}\right)^2}\right] - \ln\left[\frac{V_{Fi} - w_L \cdot L}{H_{Fi}} + \sqrt{1 + \left(\frac{V_{Fi} - w_L \cdot L}{H_{Fi}}\right)^2}\right]\right\} \tag{28}$$

$$z_{Fi}(H_{Fi}, V_{Fi}) = \frac{H_{Fi}}{w_L} \cdot \left[\sqrt{1 + \left(\frac{V_{Fi}}{H_{Fi}}\right)^2} - \sqrt{1 + \left(\frac{V_{Fi} - w_L \cdot L}{H_{Fi}}\right)^2}\right] + \frac{1}{EA} \cdot \left(V_{Fi} \cdot L - \frac{w_L \cdot L^2}{2}\right) \tag{29}$$

These systems of equations are composed of implicit equations, and to solve them—as indicated in [61]—the Newton–Raphson method explained in [69] is used. This is an

iteration method that needs a value for H_{Fi} and V_{Fi} as a starting point for the iteration process; in [61], how to initialize these values is explained.

How to obtain the values of the horizontal (H_{Ai}) and vertical (V_{Ai}) components of the vector of forces produced in each of the anchors is also explained in [61]. The calculation of these components is not included in this work since they are not necessary to calculate the vector of mooring system forces.

Once the appropriate system of equations has been solved, from the values of H_{Fi} and V_{Fi}, the force vector of the corresponding mooring line ($F_{Line\ i}$ or $\overset{\rightarrow LINE\ i}{F}_{(ANCHOR)}(t)$) is obtained by applying Equation (30). In Equations (25) to (30), the H_{Fi} and V_{Fi} components are dependent on time; this detail has not been indicated in them for clarity, but this dependence is indicated on the force vector of Equation (30). In this equation, the force vector is expressed in a homogeneous format for its combination with the corresponding homogeneous transformation matrices.

$$\overset{\rightarrow LINE\ i}{F}_{(ANCHOR)}(t) = F_{Line\ i} = [-H_{Fi}\,0\,-V_{Fi}\,0]^T \tag{30}$$

As indicated in Section 2.2 and verified in Equation (15), the force vector of each mooring line must be expressed in the mobile coordinate system. This is performed in two steps: First by means of Equation (31), the force vector is expressed in the inertial coordinate system.

$$\overset{\rightarrow LINE\ i}{F}_{(INERTIAL)}(t) = M_{HTi\,ANCHOR}^{\quad INERTIAL} \cdot \overset{\rightarrow LINE\ i}{F}_{(ANCHOR)}(t) \tag{31}$$

As a second step, Equation (32) is used to express the force vector in the mobile coordinate system. The homogeneous transformation matrix ($M_{HT\,BODY}^{\quad INERTIAL}$) is obtained by processing the kinematics of the floating hybrid system, whose detailed explanation is found in [1].

$$\overset{\rightarrow LINE\ i}{F}_{(BODY)}(t) = \left(M_{HT\,BODY}^{\quad INERTIAL} \right)^{-1} \cdot \overset{\rightarrow LINE\ i}{F}_{(INERTIAL)}(t) \tag{32}$$

Once the force vectors of each mooring line have been calculated and expressed in the mobile coordinate system using Equation (32), the last step is to obtain an equivalent force and moment vector expressed at the origin of the mobile coordinate system—which is the point where all the forces are expressed to apply the dynamics equations (Equations (3) and (4))—equivalent to the force vectors calculated in each of the fairleads. This is performed using Equations (33) and (34). This is a common method used in mechanics and can be found in [62–64].

$$\overset{\rightarrow LINE\ i}{M}_{(BODY)}(t) = p_{Fi(BODY)} \times \overset{\rightarrow LINE\ i}{F}_{(BODY)}(t) = \begin{vmatrix} \vec{i} & \vec{j} & \vec{k} \\ x_{pFi} & y_{pFi} & z_{pFi} \\ F_x & F_y & F_z \end{vmatrix} \tag{33}$$

$$\overset{\rightarrow LINE\ i}{F}_{j(BODY)}(t) = \begin{bmatrix} \overset{\rightarrow LINEi}{F}_{(BODY)}(t) \\ \overset{\rightarrow LINEi}{M}_{(BODY)}(t) \end{bmatrix} \tag{34}$$

As explained in previous paragraphs, when the floating system is in its initial position, the points expressed in the inertial coordinate system and in the mobile coordinate system are coincident. It has also been indicated that the fairlead points do not vary with respect to the mobile coordinate system (see Figure 5). For this reason, it could be considered that the points $p_{Fi(BODY)}$ of Equation (33) are those that appear in Table 5.

Applying from Equations (16) to (34), the force and moment vector of each one of the mooring lines is obtained, and from here, the calculation of the vector of mooring system forces is completed by applying Equation (15). This last result is used in Equation (4) to

obtain the resultant vector from all the forces and moments acting on the floating hybrid system.

In this work, the modeling of the mooring system is carried out in the same way as in [2] for a floating OC3-Hywind-type system. The same simplifications have also been considered, including the simplification of the delta connection of each mooring line with its fairlead. This produces a decrease in the yaw stiffness of the mooring lines. This issue is compensated for by applying an additional yaw spring stiffness value (see Table 6) for the entire mooring system. For simplicity and following the same criteria used in FASTv8 [7], this compensation is performed together with the calculation of the additional linear damping, which is explained in the study on hydrodynamics in Section 2.6.2.

2.5. Vector of Gravitational Forces

The calculation of the vector of gravitational forces is based on the application of Newton's second law to the floating hybrid system. For this, the vector of gravitational forces is expressed in the inertial coordinate system ($\vec{F}_{(INERTIAL)}^{GRAVITY}$) as observed in Equation (35).

$$\vec{F}_{(INERTIAL)}^{GRAVITY} = \begin{bmatrix} 0 \\ 0 \\ -m_{FS} \cdot g \end{bmatrix} \tag{35}$$

This vector is constant—expressed in the inertial coordinate system—since it depends only on the value of the acceleration due to gravity (see Table 4) and on the total mass of the floating hybrid system (m_{FS}). The calculation of this mass is explained in [1] but it simply consists of adding the masses—found in Appendix A of [1]—of all the bodies that make up the floating hybrid system.

Following the calculation criteria established for this work, the vector of forces represented in Equation (35) must be expressed in the mobile coordinate system ($\vec{F}_{(BODY)}^{GRAVITY}(t)$), through Equation (36). The $M_{BODY}^{INERTIAL}$ matrix is equivalent to the $M_{HT\,BODY}^{INERTIAL}$ matrix as long as only vectors—no points—are interchanged between coordinate systems. With the $M_{BODY}^{INERTIAL}$ matrix, the vectors are represented with three components, while with the $M_{HT\,BODY}^{INERTIAL}$ matrix, they have to be represented in a homogeneous format.

$$\vec{F}_{(BODY)}^{GRAVITY}(t) = \left(M_{BODY}^{INERTIAL}\right)^{-1} \cdot \vec{F}_{(INERTIAL)}^{GRAVITY} \tag{36}$$

The point of application of the force is the center of mass ($CoM_{(BODY)}(t)$)—expressed in the mobile coordinate system—of the floating hybrid system, and by means of Equations (37) and (38), the equivalent force and moment vector expressed at the origin of the mobile coordinate system is obtained. The calculation of ($CoM_{(BODY)}(t)$) in explained in [1] and is time-dependent due to the rotation of the turbines.

$$\vec{M}_{(BODY)}^{GRAVITY}(t) = CoM_{(BODY)}(t) \times \vec{F}_{(BODY)}^{GRAVITY}(t) = \begin{vmatrix} \vec{i} & \vec{j} & \vec{k} \\ x_{CoM} & y_{CoM} & z_{CoM} \\ F_x & F_y & F_z \end{vmatrix} \tag{37}$$

$$\vec{F}_{i(BODY)}^{GRAVITY}(t) = \begin{bmatrix} \vec{F}_{(BODY)}^{GRAVITY}(t) \\ \vec{M}_{(BODY)}^{GRAVITY}(t) \end{bmatrix} \tag{38}$$

Figure 9 shows—it two instants of time—the vector of gravitational forces located at its point of application (*CoM*) and the vector of hydrostatic forces also located at its point of application (*CoB*).
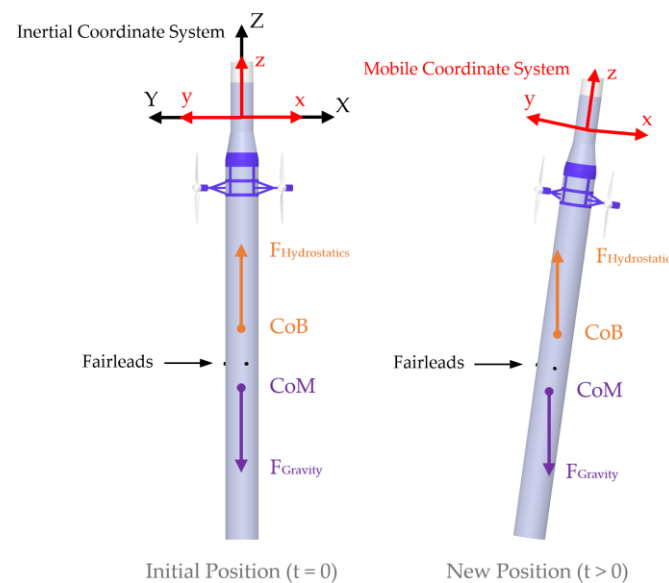
Figure 9. Gravity and hydrostatic force vectors and their points of application.

From Figure 9 it may be deduced that, although the magnitude of the vector is constant both in the inertial and mobile coordinate systems, the components of the vector are constant only in the inertial coordinate system (see Equation (35)). This is due to the change in location experienced by the mobile coordinate system attached to the floating system, so in this coordinate system, the components of the force vector vary with time. Mathematically, this is proved since—as explained in [1]—the transformation matrix ($M_{BODY}^{INERTIAL}$) also varies with time (see Equation (36)).

2.6. Vector of Hydrodynamics Forces

This section explains in detail the set of forces that act on a physical system partially submerged in a fluid—such as seawater in this case—with a density much greater than that of air (see Table 4). It is about solving a complex problem—the hydrodynamic problem—in which many factors influence. Generalizing, it could be considered that the modeling of the hydrodynamic problem always requires neglecting aspects that are not very influential, with the aim of having a reliable and robust model but with an acceptable computational cost, assuming that simulation inaccuracies could occur in exceptional situations due to this unmodeled dynamics.

Hydrodynamics is considered the key to the investigation of floating power generation systems [70]. In [58], an exhaustive analysis of the theory associated with the hydrodynamic problem applicable to any oceanic engineering system is presented. In contrast, in [70], a review of the problem of the influence of hydrodynamics on floating wind turbines is made. In relation to floating hybrid systems, [71] presents an interesting study of the hydrodynamic problem based on a floating wind turbine that combines a wave energy generation system.

The modeling of the hydrodynamic problem presented in this work, in other words, the modeling of the hydrodynamic problem implemented in the FHYGSYS tool, is based on the one proposed in [61] but with some nuances, nuances based on other approaches to certain parts of the hydrodynamic model, exposed in [60,72,73] or on our own conclusions drawn from the experience acquired in the study, development, and validation of the FHYGSYS tool. All these aspects are dealt with in detail in the following subsections.

As also indicated in [1], in this work, the force and moment vector of the hydrodynamic problem is divided into different simpler problems, which when solved separately, facilitate the complete solution of the hydrodynamic problem. This is possible given the assumption indicated in [1] and in previous sections, that the modeling hypotheses allow the application of the superposition theorem.

The set of force and moment vectors in which the hydrodynamic problem is divided—as in [1]—are shown in Equation (39), exposing each of them in the following subsections, except $F_{j(BODY)}^{\rightarrow CURRENTTURBINE}$, which is explained in Section 2.8.2.

$$F_{j(BODY)}^{\rightarrow HYDRODYNAMICS} = F_{j(BODY)}^{\rightarrow HYDROSTATICS} + F_{j(BODY)}^{\rightarrow ADDITIONAL\ DAMPING} + F_{j(BODY)}^{\rightarrow ADDED\ MASS} + F_{j(BODY)}^{\rightarrow VISCOUS\ DRAG} + F_{j(BODY)}^{\rightarrow CURRENT\ TURBINE} + F_{j(BODY)}^{\rightarrow WAVES} \quad (39)$$

2.6.1. Vector of Hydrostatic Forces

Obtaining the vector of hydrostatic forces is based on the application of Archimedes' principle [74] to the floating hybrid system. Equation (40) shows the vector of hydrostatic forces expressed in the inertial coordinate system ($F_{(INERTIAL)}^{\rightarrow HYDROSTATICS}(t)$).

$$F_{(INERTIAL)}^{\rightarrow HYDROSTATICS}(t) = \begin{bmatrix} 0 \\ 0 \\ m_{SUM}(t) \cdot g \end{bmatrix} \quad (40)$$

As observed in Equation (40), the vector depends on gravity (see Table 4) and on the mass of the submerged volume ($m_{SUM}(t)$). This mass is obtained as the product of the density of seawater (see Table 4) and the submerged volume at each instant of time. The calculation of $m_{SUM}(t)$ is explained in detail in [1].

Observing Equation (40) and Figure 9, it can be deduced that the vector of hydrostatic forces varies with time in the inertial coordinate system—due to the variation in the submerged volume of the floating system at each instant of time—and that it also varies with time in the mobile coordinate system, due to the variation in the submerged volume and due to the change in position, at each instant of time, of the mobile coordinate system with respect to the inertial coordinate system.

As in previous cases, from the vector of forces expressed in the inertial coordinate system, using Equation (41), the vector ($F_{(BODY)}^{\rightarrow HYDROSTATICS}(t)$) expressed in the mobile coordinate system is obtained.

$$F_{(BODY)}^{\rightarrow HYDROSTATICS}(t) = \left(M_{BODY}^{INERTIAL} \right)^{-1} \cdot F_{(INERTIAL)}^{\rightarrow HYDROSTATICS}(t) \quad (41)$$

Subsequently, from the center of buoyancy of the floating system ($CoB_{(BODY)}(t)$)—point of application of force—and the force vector obtained in Equation (41), through Equations (42) and (43), the equivalent force and moment vector expressed at the origin of the mobile coordinate system is obtained.

$$M_{(BODY)}^{\rightarrow HYDROSTATICS}(t) = CoB_{(BODY)}(t) \times F_{(BODY)}^{\rightarrow HYDROSTATICS}(t) = \begin{vmatrix} \vec{i} & \vec{j} & \vec{k} \\ x_{CoB} & y_{CoB} & z_{CoB} \\ F_x & F_y & F_z \end{vmatrix} \quad (42)$$

$$F_{i(BODY)}^{\rightarrow HYDROSTATICS}(t) = \begin{bmatrix} F_{(BODY)}^{\rightarrow HYDROSTATICS}(t) \\ M_{(BODY)}^{\rightarrow HYDROSTATICS}(t) \end{bmatrix} \quad (43)$$

The calculation of the center of buoyancy ($CoB_{(BODY)}(t)$) was explained in detail in [1] and due to the variation with time of the submerged volume and the rotation of the marine turbines, its calculation is carried out at each instant of time.

In other works, in which the hydrostatic problem is treated, as in [60,73,75], a combined solution of the vectors of gravitational and hydrostatic forces is explained. In [1] and in this work, it has been decided to expose the two forces separately for clarity. Bearing in mind that in this work a spar-buoy-type floating structure is modeled—it is not intended to offer a generalized solution for all types of floating structures—the exposed modeling of these

two forces provides mathematical simplicity, that is justified with the validation tests of the FHYGSYS tool exposed in Section 3, in Appendix B, and in Appendix E of [1].

2.6.2. Vector of Additional Damping and Stiffness Forces

In [2], it is explained that Statoil—the developer of the spar-buoy floating system concept called "Hywind"—indicates that the joint influence of the linear radiation damping—from potential-flow theory—and the nonlinear viscous-drag—from the Morison's formulation—when summed, do not capture all the hydrodynamic damping of a real Hywind floating platform.

To correct this situation in [2], the inclusion of a vector of additional damping forces is proposed. This force is obtained from Equation (44), also extracted from [2], where the additional damping matrix is multiplied by the velocity vector ($\vec{vv}_{i(INERTIAL)}(t)$) of the floating hybrid system expressed in the inertial coordinate system (see Equation (45)). The calculation of the vector $\vec{vv}_{i(INERTIAL)}(t)$ is explained in detail in [1].

$$\begin{bmatrix} \vec{F}_{(INERTIAL)}^{ADDITIONAL\ DAMPING}(t) \\ \vec{M}_{(INERTIAL)}^{ADDITIONAL\ DAMPING}(t) \end{bmatrix} = - \begin{bmatrix} 100,000 & 0 & 0 & 0 & 0 & 0 \\ 0 & 100,000 & 0 & 0 & 0 & 0 \\ 0 & 0 & 130,000 & 0 & 0 & 0 \\ 0 & 0 & 0 & 0 & 0 & 0 \\ 0 & 0 & 0 & 0 & 0 & 0 \\ 0 & 0 & 0 & 0 & 0 & 13,000,000 \end{bmatrix} \cdot \begin{bmatrix} \dot{q}_1 \\ \dot{q}_2 \\ \dot{q}_3 \\ \dot{q}_4 \\ \dot{q}_5 \\ \dot{q}_6 \end{bmatrix} \tag{44}$$

$$\vec{vv}_{i(INERTIAL)}(t) = \begin{bmatrix} \dot{q}_1 \dot{q}_2 \dot{q}_3 \dot{q}_4 \dot{q}_5 \dot{q}_6 \end{bmatrix}^T \tag{45}$$

As indicated in Section 2.4, one of the simplifications assumed in [2] for the modeling of the mooring system produces a decrease in the yaw stiffness of the mooring lines. It is also indicated that this issue is compensated for by applying an additional yaw spring stiffness value (*AddYS* in Table 6) for the entire mooring system. Following the criteria used in FAST v8 [7], this compensation is made by applying Equation (46), where $q_6(t)$ is the yaw value of the floating hybrid system at each instant of time.

$$\vec{M}_{(INERTIAL)}^{STIFFNESS}(t) = \begin{bmatrix} 0 \\ 0 \\ -AddYS \cdot q_6(t) \end{bmatrix} \tag{46}$$

The point of application of the calculated forces and moments is the origin of the inertial coordinate system. Through Equations (47) and (48), the force vector ($\vec{F}_{(BODY)}^{ADDITIONAL\ DAMPING}(t)$) and the moment vector ($\vec{M}_{(BODY)}^{ADDITIONAL\ DAMPING\ \&\ STIFFNESS}(t)$) expressed in the mobile coordinate system are obtained, respectively.

$$\vec{F}_{(BODY)}^{ADDITIONAL\ DAMPING}(t) = \left(M_{BODY}^{INERTIAL} \right)^{-1} \cdot \vec{F}_{(INERTIAL)}^{ADDITIONAL\ DAMPING}(t) \tag{47}$$

$$\vec{M}_{(BODY)}^{ADDDAMP\ \&\ STIFFNESS}(t) = \left(M_{BODY}^{INERTIAL} \right)^{-1} \cdot \left(\vec{M}_{(INERTIAL)}^{ADDITIONAL\ DAMPING}(t) + \vec{M}_{(INERTIAL)}^{STIFFNESS}(t) \right) \tag{48}$$

Finally, in Equation (49), the two vectors obtained in Equations (47) and (48) are joined to find the vector of additional damping and stiffness forces ($\vec{F}_{j(BODY)}^{ADDITIONAL\ DAMPING}(t)$).

$$\vec{F}_{j(BODY)}^{ADDITIONAL\ DAMPING}(t) = \begin{bmatrix} \vec{F}_{(BODY)}^{ADDITIONAL\ DAMPING}(t) \\ \vec{M}_{(BODY)}^{ADDDAMP\ \&\ STIFFNESS}(t) \end{bmatrix} \tag{49}$$

2.6.3. Vector of Viscous Drag Forces

This force appears when a fluid moving at a certain speed impacts a body that is stationary, when a body moves over a fluid that is at rest, or when both the fluid and the body move at certain speeds. This effect increases, fundamentally, with the velocity—of the fluid, the body, or both—and with the density of the fluid.

The calculation of the vector of viscous drag forces is based on the application of Morison's equation [61,65,72,73,76] combined with the strip theory. This consists of dividing the floating system into small sections—circular sections in this case—in which Morison's equation is applied, and then, the results are integrated. In [1] and in this work, the zones of the tower of the floating system free from the shadow of the wind turbine ($h_{free\ shadow}$) and the submerged part of the floating platform ($h_{submerged}$) have been divided into these small circular sections. With Equation (50) and the data in Table 7, $h_{free\ shadow}$ is calculated.

$$h_{free\ shadow} = h_{Hub} - \left(L_{Blade} + \frac{D_{Hub}}{2} \right) \cdot \cos \left(\varphi_{Shaft\ Tilt} - \varphi_{Precone} \right) \tag{50}$$

Table 7. Dimensions of the wind turbine necessary for the calculation of $h_{Tower\ Shadow}$.

Property	Value	Symbol
Hub height [1]	90 m	h_{Hub}
Hub diameter [1]	3 m	D_{Hub}
Blade Length [1]	61.5 m	L_{Blade}
Precone [1]	−2.5 deg	$\varphi_{Precone}$
Shaft tilt [1]	5 deg	$\varphi_{Shaft\ Tilt}$
Total draft [2]	120 m	$h_{submerged}$

[1] Source [3]. [2] Source [2], this value is at the initial position.

Considering the balance between accurate results and acceptable computational speed, the tower portion ($h_{free\ shadow}$) and the submerged area of the floating platform ($h_{submerged}$) have been divided into circular sections every 0.5 m along the Z axis, resulting in 296 circular sections in the centers of which the p_{VDi} points are located. Figure 10 shows these zones, affected by the corresponding thrust vectors.
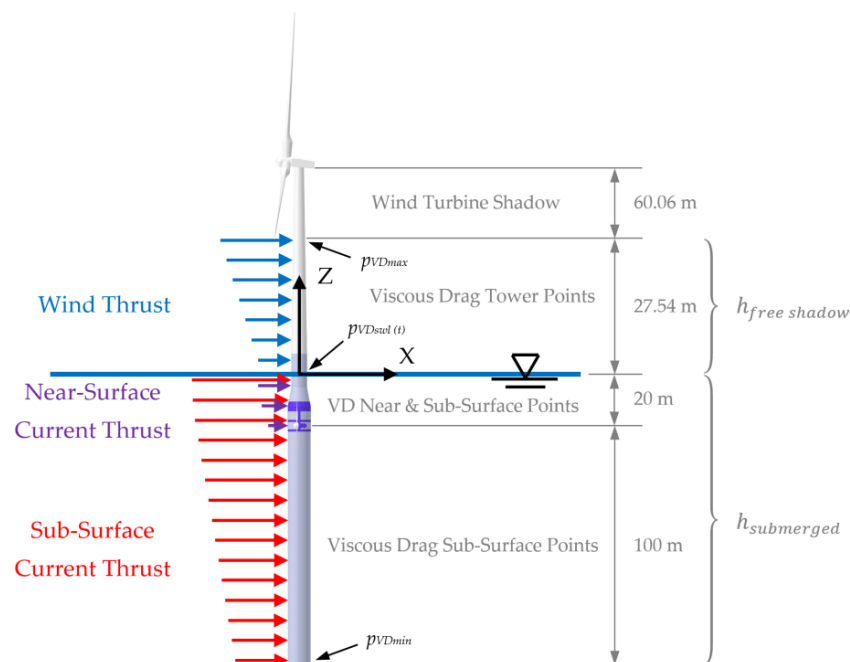

Figure 10. Thrusts included in the vector of viscous drag forces.

Figure 10 also shows the three thrusts included in the calculation of the vector of viscous drag forces ($\overset{\rightarrow VISCOUS\ DRAG}{F_{j(BODY)}}$): wind thrust, near-surface current thrust, and sub-surface current thrust. In [1], the description of this vector is simplified, showing the influence of the three thrusts through Equation (51).

$$\overset{\rightarrow VISCOUS\ DRAG}{F_{j(BODY)}} = \overset{\rightarrow WIND\ TOWER}{F_{j(BODY)}} + \overset{\rightarrow NEAR-SURFACE\ CURRENT}{F_{j(BODY)}} + \overset{\rightarrow SUB-SURFACE\ CURRENT}{F_{j(BODY)}} \tag{51}$$

The calculation of the vector of viscous drag forces is somewhat more laborious. The floating hybrid system is immersed in two fluids, air and seawater—the density of the seawater is approximately a thousand times greater than that of air (see Table 4)—and it moves interacting with the two fluids that can have different directions and speeds. In this situation, the relative velocity ($\vec{v}_{VDRi(INERTIAL)}(h,t)$) between the fluids and the floating platform can result in hydrodynamic damping [65].

As a starting point, instead of the thrusts indicated in Figure 10, the velocity of each fluid is used. These velocities are calculated by means of Equations (6), (10), and (13), for wind ($\vec{v}_{WIND(INERTIAL)}(h)$), sub-surface current ($\vec{v}_{SSCUR(INERTIAL)}(h)$), and near-surface current ($\vec{v}_{NSCUR(INERTIAL)}(h)$), respectively. These three velocities depend on the height or depth—depending on the case—and are calculated—as explained in Section 2.3—in each one of the p_{VDi} points. For the calculation of the vector of viscous drag forces, the effect of marine turbines and their support has been neglected, since it is very small compared with the effect of the floating platform.

In Equation (52), the resultant velocity vectors—relative velocity between the fluids and the floating platform, $\vec{v}_{VDRi(INERTIAL)}(h,t)$—calculated at each of the p_{VDi} points and expressed in the inertial coordinate system are obtained.

$$\vec{v}_{VDRi(INERTIAL)}(h,t) = \vec{v}_{WIND(INERTIAL)}(h) + \vec{v}_{NSCUR(INERTIAL)}(h) + \vec{v}_{SSCUR(INERTIAL)}(h) - \vec{v}_{VDi(INERTIAL)}(h,t) \tag{52}$$

As indicated in previous paragraphs, the velocity of the floating platform ($\vec{v}_{VDi(INERTIAL)}(h,t)$) moving through the fluid must be considered in the calculation of Equation (52). This velocity is obtained—as shown in Equation (53)—by differentiating the position of the p_{VDi} points—expressed in the inertial coordinate system—with respect to time.

$$\vec{v}_{VDi(INERTIAL)}(h,t) = \frac{d}{dt}\vec{p}_{VDi(INERTIAL)}(t) \tag{53}$$

Following the explanation of [65], when a structure moves significantly, the Morison equation is applied from the relative velocity ($\vec{v}_{VDRi(INERTIAL)}(h,t)$) calculated in Equation (52); this is also indicated in [61,72,76]. Due to the nature of the Morison equation, it only makes sense to apply it to the surge and sway modes of motion [61,72]. Equations (54) and (55) show Morison's equation [61,65,72,73,76] for each of these modes of motion.

$$d\overset{\rightarrow VISCOUS}{F_{x(INERTIAL)}}(h,t) = \frac{1}{2} \cdot C_D(h) \cdot \rho_{fluid}(h) \cdot D(h) \cdot \vec{v}_{VDRix(INERTIAL)}(h,t) \cdot \left|\vec{v}_{VDRix-y(INERTIAL)}(h,t)\right| \cdot dh \tag{54}$$

$$d\overset{\rightarrow VISCOUS}{F_{y(INERTIAL)}}(h,t) = \frac{1}{2} \cdot C_D(h) \cdot \rho_{fluid}(h) \cdot D(h) \cdot \vec{v}_{VDRiy(INERTIAL)}(h,t) \cdot \left|\vec{v}_{VDRix-y(INERTIAL)}(h,t)\right| \cdot dh \tag{55}$$

The magnitude of the relative velocity ($\left|\vec{v}_{VDRix-y(INERTIAL)}(h,t)\right|$) is easily calculated using Equation (56), while the values of the drag coefficient ($C_D(h)$), fluid density ($\rho_{fluid}(h)$), and diameter of the circular section ($D(h)$) used in Equations (54) and (55) are shown in Table 8. To calculate the diameters ($D(h)$) of the intermediate points of the tower and of the

conical region of the floating platform, linear interpolation is performed from the data in Table 8.

$$\left| \vec{v}_{VDRix-y(INERTIAL)}(h,t) \right| = \sqrt{\vec{v}_{VDRix(INERTIAL)}^{2}(h,t) + \vec{v}_{VDRiy(INERTIAL)}^{2}(h,t)} \quad (56)$$

Table 8. Data from significant points used with Morison's equation.

Zone	Location	$C_D(h)$	$\rho_{fluid}(h)$ [3]	$D(h)$ [2]
WT Shadow	Tower top	1 [1]	ρ_{AIR}	3.87 m
$h_{free\ shadow}$	Tower bottom	1 [1]	ρ_{AIR}	6.5 m
$h_{free\ shadow}$	Floating platform above still water level	0.6 [2]	ρ_{AIR}	6.5 m
$h_{submerged}$	Floating platform above the conical region, below still water level	0.6 [2]	$\rho_{SEA\ WATER}$	6.5
$h_{submerged}$	Floating platform below the conical region	0.6 [2]	$\rho_{SEA\ WATER}$	9.4 m

[1] Source [7,77]. [2] Source [2]. [3] Table 2.

From the force vectors calculated by Morison's equation at the p_{VDi} points—force application points ($p_{VDi} = p_{VDi(INERTIAL)}(t)$)—the next step is to obtain the moments of these forces expressed at the origin of the mobile coordinate system. This is achieved by Equations (57)–(59).

$$d\vec{F}_{(BODY)}^{VISCOUS}(h,t) = \left(M_{BODY}^{INERTIAL}\right)^{-1} \cdot \left[d\vec{F}_{x(INERTIAL)}^{VISCOUS}(h,t) \, d\vec{F}_{y(INERTIAL)}^{VISCOUS}(h,t) \, 0 \right]^{T} \quad (57)$$

$$p_{VDi(BODY)}(t) = \left(M_{BODY}^{INERTIAL}\right)^{-1} \cdot p_{VDi(INERTIAL)}(t) \quad (58)$$

$$d\vec{M}_{(BODY)}^{VISCOUS}(h,t) = p_{VDi(BODY)}(t) \times d\vec{F}_{(BODY)}^{VISCOUS}(h,t) = \begin{vmatrix} \vec{i} & \vec{j} & \vec{k} \\ x_{pVD} & y_{pVD} & z_{pVD} \\ dF_x & dF_y & dF_z \end{vmatrix} \quad (59)$$

Afterwards, the integral is carried out—through Equation (60)—of the force and moment vectors between the points p_{VDmin} and p_{VDmax} (see Figure 10) with a dh—as indicated above—of 0.5 m. This integral is calculated by applying the multiple application of trapezoidal rule [69].

$$\vec{F}_{(BODY)}^{VISCOUS}(t) = \int_{pVDmin}^{pVDmax} \begin{bmatrix} d\vec{F}_{(BODY)}^{VISCOUS}(h,t) \\ d\vec{M}_{(BODY)}^{VISCOUS}(h,t) \end{bmatrix} \cdot dh \quad (60)$$

Finally, the force and moment vector obtained with Equation (60) is expressed in the inertial coordinate system to ensure that only the surge, sway, roll, and pitch modes of motion have a non-zero value. This is performed by means of Equations (61) and (62), while with Equation (63), the final vector of viscous drag forces is calculated.

$$\vec{F}_{(INERTIAL)}^{VISCOUS}(t) = M_{BODY}^{INERTIAL} \cdot \vec{F}_{(BODY)}^{VISCOUS}(t) \quad (61)$$

$$\overset{\rightarrow VISCOUS\ DRAG}{F_{(INERTIAL)}}(t) = \begin{bmatrix} 1 & 0 & 0 & 0 & 0 & 0 \\ 0 & 1 & 0 & 0 & 0 & 0 \\ 0 & 0 & 0 & 0 & 0 & 0 \\ 0 & 0 & 0 & 1 & 0 & 0 \\ 0 & 0 & 0 & 0 & 1 & 0 \\ 0 & 0 & 0 & 0 & 0 & 0 \end{bmatrix} \cdot \overset{\rightarrow VISCOUS}{F_{(INERTIAL)}}(t) \tag{62}$$

$$\overset{\rightarrow VISCOUS\ DRAG}{F_{j(BODY)}}(t) = \left(M_{BODY}^{INERTIAL} \right)^{-1} \cdot \overset{\rightarrow VISCOUS\ DRAG}{F_{(INERTIAL)}}(t) \tag{63}$$

2.6.4. Vector of Added Mass Forces

The added mass should be interpreted as a particular volume of fluid particles that are accelerated with the submerged part of the floating system [58]. The modeling used in the FHYGSYS tool to compute the added mass and used in Equation (3) to solve the dynamics of the floating system is explained in detail in Section 2.3.3 of [1].

In this work, a model of the computation of the added mass equivalent to the one explained in [1] is presented, which is also implemented in FHYGSYS and allows us to visualize the responses of the vector of added mass forces in each one of the degrees of freedom of the floating system. The modeling consists of solving the system of differential equations shown in Equations (64)–(69). This system of equations is extracted from [60,78], where its algebraic development also appears, not included in this work for brevity.

$$\frac{d}{dt}\frac{\partial T_{AM}}{\partial u} = r \cdot \frac{\partial T_{AM}}{\partial v} - q \cdot \frac{\partial T_{AM}}{\partial w} - X_A \tag{64}$$

$$\frac{d}{dt}\frac{\partial T_{AM}}{\partial v} = p \cdot \frac{\partial T_{AM}}{\partial w} - r \cdot \frac{\partial T_{AM}}{\partial u} - Y_A \tag{65}$$

$$\frac{d}{dt}\frac{\partial T_{AM}}{\partial w} = q \cdot \frac{\partial T_{AM}}{\partial u} - p \cdot \frac{\partial T_{AM}}{\partial v} - Z_A \tag{66}$$

$$\frac{d}{dt}\frac{\partial T_{AM}}{\partial p} = w \cdot \frac{\partial T_{AM}}{\partial v} - v \cdot \frac{\partial T_{AM}}{\partial w} + r \cdot \frac{\partial T_{AM}}{\partial q} - q \cdot \frac{\partial T_{AM}}{\partial r} - K_A \tag{67}$$

$$\frac{d}{dt}\frac{\partial T_{AM}}{\partial q} = u \cdot \frac{\partial T_{AM}}{\partial w} - w \cdot \frac{\partial T_{AM}}{\partial u} + p \cdot \frac{\partial T_{AM}}{\partial r} - r \cdot \frac{\partial T_{AM}}{\partial p} - M_A \tag{68}$$

$$\frac{d}{dt}\frac{\partial T_{AM}}{\partial r} = v \cdot \frac{\partial T_{AM}}{\partial u} - u \cdot \frac{\partial T_{AM}}{\partial v} + q \cdot \frac{\partial T_{AM}}{\partial p} - p \cdot \frac{\partial T_{AM}}{\partial q} - N_A \tag{69}$$

The system of equations is solved from the value of the kinetic energy of the added mass (T_{AM}) and the velocity vector ($\overrightarrow{vv}_{i(BODY)}$) of the floating system expressed in the mobile coordinate system. Both magnitudes are obtained by applying Equations (70) and (71), which thus described, are extracted from [1], deduced from similar expressions explained in [60]. How to obtaining the velocity vector ($\overrightarrow{vv}_{i(BODY)}$) and the added mass matrix (M_{AM}) is explained in detail in [1]. In Appendix A, the calculation method of the added mass matrix (M_{AM}) is shown with an example.

$$T_{AM} = \frac{1}{2} \cdot \left(\overrightarrow{vv}_{i(BODY)} \right)^T \cdot M_{AM} \cdot \overrightarrow{vv}_{i(BODY)} \tag{70}$$

$$\overrightarrow{vv}_{i(BODY)}(t) = [u\ v\ w\ p\ q\ r]^T \tag{71}$$

Once the system of equations has been solved, the values of the components of the vector of added mass forces are obtained as shown in Equation (72).

$$\vec{F}_{j(BODY)}^{ADDEDMASS}(t) = -[X_A Y_A Z_A K_A M_A N_A]^T \tag{72}$$

2.6.5. Vector of Wave Forces

There are different approaches for the mathematical modeling of waves, but it could be summarized into two: the one based on the regular—or linear—wave theory [58,72–74,76] and the one based on a spectrum that allows for generating irregular—or non-linear—waves [58,61,65,73,74,76]. In FHYGSYS, it has been decided to model the waves using a spectrum that provides irregular waves, since this produces more realistic results.

There are different types of spectra, but [65] recommends two for wave simulation in offshore wind turbines systems: the Pierson–Moskowitz spectrum and the JONSWAP (Joint North Sea Wave Project) spectrum. In [65], it is indicated that the Pierson–Moskowitz spectrum is often used for a fatigue analysis, while the JONSWAP spectrum is used for an extreme event analysis.

In this work, the waves have been modeled using the JONSWAP spectrum; this allows us to perform simulations with any of the mentioned spectra since the JONSWAP spectrum is based on the Pierson–Moskowitz spectrum.

To generate a spectrum of waves, two interrelated data are needed to define their behavior: the significant wave height and their peak period. These two data are also related—on many occasions—to wind speed, although this depends on the particular conditions of each geographical location [65,73].

As an example of the relationship between significant wave height, wave period, and wind speed, the data in Table 9 are shown. These data have been extracted from [73] and are used in FHYGSYS when it is desired to generate a wind speed-dependent sea state. A reduced but equivalent version of the data in Table 9 is presented in [2].

Table 9. Environmental conditions.

Mean Wind Speed [1] V_{W-REF} (m/s)	Significant Wave Height H_s (m)	Peak Period T_p (s)	Wavelength [2] λ_{wave} (m)
2.5	0.09	2.0	6
7.5	0.67	4.8	34.56
8.6	0.88	5.4	43.74
10.5	1.40	6.5	63.375
12.1	1.86	7.2	77.76
13.6	2.44	8.1	98.415
17.6	3.66	9.7	141.135
22.0	4.57	10.5	165.375
25.8	5.49	11.3	191.535
30.1	6.71	12.1	219.615
35.1	9.14	13.6	277.44
42.9	15.24	17.0	433.5

[1] Wind speeds at 90 m reference height. [2] Approximate values calculated with Equation (73).

To expand the information in Table 9, the wavelength calculated using Equation (73), extracted from [79], has been included. In [2], some expressions are presented that allow for a more precise calculation of λ_{wave}, but with the little difference found, Equation (73) has been used for simplicity of calculation.

$$\lambda_{wave} \cong T_p^2 + \frac{T_p^2}{2} \tag{73}$$

The Pierson–Moskowitz spectrum is obtained using Equation (74); the equation thus expressed is extracted from [61,73].

$$S_{P-M}^{1-Sided}(\omega) = \frac{1}{2 \cdot \pi} \cdot \frac{5}{16} \cdot H_s^2 \cdot T_p \cdot \left(\frac{\omega \cdot T_p}{2 \cdot \pi}\right)^{-5} \cdot \exp\left[-\frac{5}{4} \cdot \left(\frac{\omega \cdot T_p}{2 \cdot \pi}\right)^{-4}\right] \tag{74}$$

When FHYGSYS works with the JONSWAP spectrum, Equation (75) is used, which, as can be seen, is based on the result of Equation (74). Equation (75) expressed in this way is also extracted from [61,73].

$$S_{JONSWAP}^{1-Sided}(\omega) = S_{P-M}^{1-Sided}(\omega) \cdot \left[1 - 0.287 \cdot \ln \gamma\left(T_p, H_s\right)\right] \cdot \gamma\left(T_p, H_s\right)^{\exp\left[-\frac{1}{2} \cdot \left(\frac{\frac{\omega \cdot T_p}{2 \cdot \pi} - 1}{\sigma(\omega)}\right)^2\right]} \tag{75}$$

Equations (74) and (75) give the results in rad/s. In [65], the same equations appear but are adjusted to give the results in Hz (f). On the other hand, in Equation (75), there are two coefficients, $\gamma\left(T_p, H_s\right)$ and $\sigma(\omega)$, whose calculations are easy to perform and are explained in [61,65]; they are not included in this work for brevity.

As observed in Equations (74) and (75), the results depend on the frequency of the incident waves (ω) expressed in rad/s. To solve them, a frequency sweep must be carried out, solving the equations for each of the frequencies. To obtain acceptable results with a low computational cost, a cut-off frequency is used that delimits the bandwidth used. Specifically, the same technique is used as the one described in [61], which consists of using a proportional cut-off frequency corresponding to the spectrum peak period, being the proportionality factor used equal to 3.0 [61].

Once the bandwidth is bounded, FHYGSYS divides it into 120 intervals from the lowest frequency to the highest frequency, thus defining the omega (ω) values for the rest of the calculations. With this number of intervals, acceptable results have been obtained in the model validation process with FASTv8 [7]. The results of this validation appear in Section 3 and in Appendix B.

With Equations (74) and (75) only one side of the spectrum ($S_{JONSWAP}^{1-Sided}(\omega)$) is obtained; to obtain the complete spectrum ($S_{JONSWAP}^{2-Sided}(\omega)$) necessary in subsequent calculations, Equation (76)—extracted from [61]—is used.

$$S_{JOWNSWAP}^{2-Sided}(\omega) = \begin{cases} \frac{1}{2} \cdot S_{JONSWAP}^{1-Sided}(\omega) & for \, \omega \geq 0 \\ \frac{1}{2} \cdot S_{JONSWAP}^{1-Sided}(-\omega) & for \, \omega < 0 \end{cases} \tag{76}$$

As indicated in [61], to ensure that the individual wave components have a random phase and that the instantaneous wave elevation is normally distributed with zero mean, a white Gaussian noise time-series process—represented by $W(\omega)$—is used. In [61], the implication of this term and its mode of application are explained in detail. Briefly, the term $W(\omega)$ is calculated by means of Equation (77), extracted from [61].

$$W(\omega) = \begin{cases} 0 & for \, \omega = 0 \\ \sqrt{-2 \cdot \ln[U_1(\omega)]} \cdot [\cos(2 \cdot \pi \cdot U_2(\omega)) + j \cdot \sin(2 \cdot \pi \cdot U_2(\omega))] & for \, \omega > 0 \\ \sqrt{-2 \cdot \ln[U_1(-\omega)]} \cdot [\cos(2 \cdot \pi \cdot U_2(-\omega)) - j \cdot \sin(2 \cdot \pi \cdot U_2(-\omega))] & for \, \omega < 0 \end{cases} \tag{77}$$

where j is the imaginary unit ($\sqrt{-1}$), and $U_1(\omega)$ and $U_2(\omega)$ are random numbers—obtained with Matlab® using the commands rng() and rand()—generated from two different seeds. Specifically—to help in the wave modeling validation process—the same ones used by FASTv8 [7] have been used as seeds in FHYGSYS: 1011121314 for $U_1(\omega)$ and 123456789 for $U_2(\omega)$.

Once the spectrum $S_{JONSWAP}^{2-Sided}(\omega)$ and the white Gaussian noise $W(\omega)$ have been calculated, FHYGSYS generates a mesh that represents the sea state in the geometric place where the simulation of the floating hybrid system occurs.

The elevation $\zeta_{mesh}(t)$ of each grid element is obtained as the real part of the result found using Equation (78). This equation is taken from [61], but a Δt term has been added to it—included in the discretized version of the equation from [72]—which represents the time increment (Δt) used for the simulation. As indicated in the Introduction, FHYGSYS could use a range of values from 0.1 to 0.0125 s as the time increment for simulations.

$$\zeta(t,x,y) = \frac{1}{2\cdot\pi}\cdot\int_{-\infty}^{\infty} W(\omega)\cdot\sqrt{\frac{2\cdot\pi}{\Delta t}\cdot S_{JONSWAP}^{2-Sided}(\omega)}\cdot e^{-j\cdot k(\omega)\cdot[x\cdot\cos\beta + y\cdot\sin\beta]}\cdot e^{j\cdot\omega\cdot t}\cdot d\omega \qquad (78)$$

In Equation (78), x and y are the components—expressed in the inertial coordinate system—of each grid element; β is the yaw angle—expressed in radians—that represents the direction of the waves; and $k(\omega)$ represents the wave number in a finite depth and is obtained by Equation (79), extracted from [2,61,73,76]. It is an implicit equation that is solved by applying the Newton–Raphson method explained in [69].

$$k(\omega)\cdot\tanh[k(\omega)\cdot d_{WATER}] = \frac{\omega^2}{g} \qquad (79)$$

In Equation (79), d_{WATER} represents the total water depth and g is the acceleration due to gravity; both data are shown in Table 4.

In Equation (78), the spectrum $S_{JONSWAP}^{2-Sided}(\omega)$, the white Gaussian noise $W(\omega)$, the wave number $k(\omega)$, and ω are vectors 121 elements long. This is due—as mentioned in previous paragraphs—to the fact that FHYGSYS divides the bandwidth with which ω is represented into 120 intervals. Finally, $d\omega$ is the difference between each of these intervals. With this information, Equation (78) is solved at each instant of time by applying the multiple application of trapezoidal rule [69]. Figure 11 shows the mesh that represents the sea state at a certain instant of time.
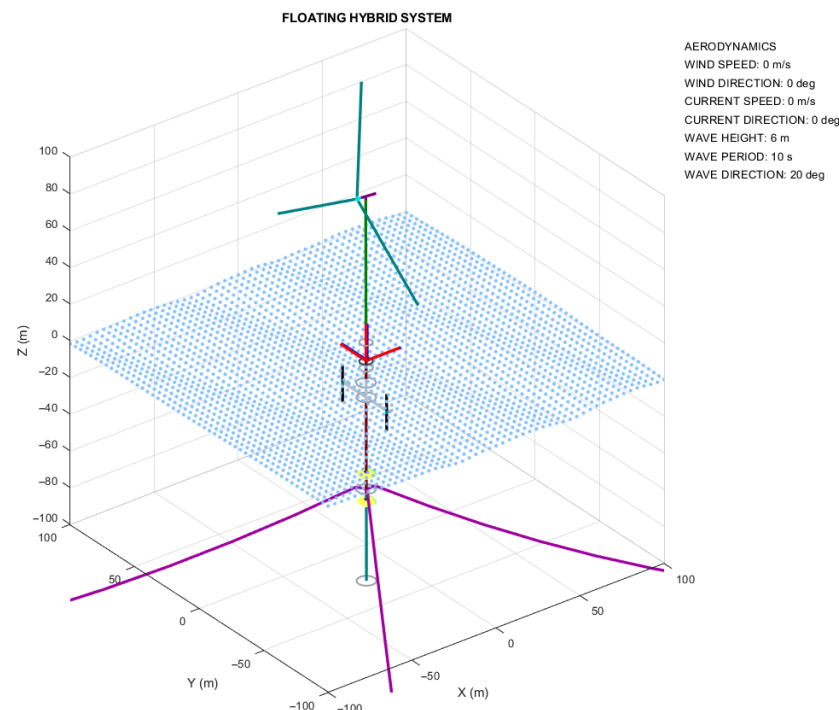

Figure 11. Mesh representing the sea state on the floating hybrid system (see Figure 1) represented by FHYGSYS (using Matlab®). Different colors are used to easily differentiate the different elements that make up the floating hybrid system.

In relation to obtaining the vector of wave forces, in [79], the calculation of this vector for certain situations is explained. On the other hand, Ref. [61] explains a generic solution

to carry out this calculation. In this work, it was decided to implement a solution based on the one described in [80] for wave excitation of a truncated vertical cylinder. For this, it is necessary to previously calculate the acceleration of the water particles produced by the waves along the submerged part of the floating platform ($h_{submerged}$). This is performed using Equation (80)—extracted from [61]—which is solved in a similar way to Equation (78). The only difference is that, in this case, the values of x, y, and z correspond to those of the $p_{VDi(INERTIAL)}$ points used to calculate the vector of viscous drag forces corresponding to the submerged part of the floating platform ($h_{submerged}$, see Figure 10).

$$a(t,x,y,z) = \int_{-\infty}^{\infty} W(\omega) \cdot \sqrt{\frac{2 \cdot \pi}{\Delta t} \cdot S_{JONSWAP}^{2-Sided}(\omega)} \cdot e^{-j \cdot k(\omega) \cdot [x \cdot \cos \beta + y \cdot \sin \beta]} \cdot \omega^2 \cdot \frac{\cosh[k(\omega) \cdot (z + d_{WATER})]}{\sinh[k(\omega) \cdot d_{WATER}]} \cdot e^{j \cdot \omega \cdot t} \cdot d\omega \quad (80)$$

The next step is to calculate the X and Y components of the acceleration found in Equation (80), this is made by applying Equations (81) and (82)—extracted from [61]—respectively. In these equations, the real part of the results obtained is taken.

$$a_{x(INERTIAL)}(h,t) = a_{x(INERTIAL)}(t,z) = Re\left[\frac{j \cdot \cos \beta}{2 \cdot \pi} \cdot a(t,x,y,z)\right] \quad (81)$$

$$a_{y(INERTIAL)}(h,t) = a_{y(INERTIAL)}(t,z) = Re\left[\frac{j \cdot \sin \beta}{2 \cdot \pi} \cdot a(t,x,y,z)\right] \quad (82)$$

With these results, Equation (83) is used to obtain the X and Y components of the differential of the force vector $d\overrightarrow{F}_{x,y(INERTIAL)}^{WAVES}(h,t)$. This is a version of the equation presented in [80] to calculate the wave excitation of a truncated vertical cylinder.

$$d\overrightarrow{F}_{x,y(INERTIAL)}^{WAVES}(h,t) = 2 \cdot \rho_{SEA\ WATER} \cdot \pi \cdot \left[\frac{D(h)}{2}\right]^2 \cdot \overrightarrow{a}_{x,y(INERTIAL)}(h,t) \cdot dh \quad (83)$$

In [80], it is considered that the cylinder has the same radius, and the acceleration at the still water level point is calculated applying an exponential term that decreases the influence of the acceleration as the depth increases along the cylinder. In Equation (83), the radius corresponding to each depth is used, obtained from the data in Table 8, in the same way as for the calculation of the vector of viscous drag forces. The acceleration term ($\overrightarrow{a}_{x,y(INERTIAL)}(h,t)$) calculated using Equations (80)–(82) includes an exponential term equivalent to that from the equation mentioned in [80]. Finally, *dh* represents the same differential—of 0.5 m—as the one used to calculate the vector of viscous drag forces.

Next, the differential of the vector $d\overrightarrow{F}_{x,y(BODY)}^{WAVES}(h,t)$—expressed in the mobile coordinate system—is calculated by applying Equation (84).

$$d\overrightarrow{F}_{x,y(BODY)}^{WAVES}(h,t) = \left(M_{BODY}^{INERTIAL}\right)^{-1} \cdot \left[d\overrightarrow{F}_{x,y(INERTIAL)}^{WAVES}(h,t)0\right]^T \quad (84)$$

Then, using Equation (85), the differential of the moments $d\overrightarrow{M}_{x,y(BODY)}^{WAVES}(h,t)$ produced at the origin of the mobile coordinate system is obtained. In Equation (85), $p_{VDi(BODY)}(t)$ points are the same as previously calculated in Equation (58).

$$d\overrightarrow{M}_{x,y(BODY)}^{WAVES}(h,t) = p_{VDi(BODY)}(t) \times d\overrightarrow{F}_{x,y(BODY)}^{WAVES}(h,t) = \begin{vmatrix} \overrightarrow{i} & \overrightarrow{j} & \overrightarrow{k} \\ x_{pVD} & y_{pVD} & z_{pVD} \\ dF_x & dF_y & dF_z \end{vmatrix} \quad (85)$$

From the data obtained in Equations (84) and (85), the force and moment vector $\overrightarrow{F}_{x,y(BODY)}^{WAVES}(t)$ for the X and Y coordinates are obtained using Equation (86). The limits of

the integral p_{VDmin} and p_{VDswl} correspond to those of the submerged part ($h_{submerged}$) of the floating platform (see Figure 10). Equation (86) is also solved by applying the multiple applications of the trapezoidal rule [69].

$$\vec{F}_{x,y(BODY)}^{WAVES}(t) = \int_{pVDmin}^{pVDswl} \left[\begin{array}{c} d\vec{F}_{x,y(BODY)}^{WAVES}(h,t) \\ d\vec{M}_{x,y(BODY)}^{WAVES}(h,t) \end{array} \right] \cdot dh \tag{86}$$

Finally, the Z component of the vector of wave forces is calculated using Equation (87), extracted from [79,80]. This equation calculates the mass of the volume of water caused by the elevation $\zeta_{swl}(t)$ in the waves at the point of intersection of the floating platform with the still water level ($p_{VDswl}(t)$), with the circular area at this point being $\pi \cdot r_{swl}^2(t)$. The mass is then multiplied by the acceleration due to gravity g to calculate $\vec{F}_{z(INERTIAL)}^{WAVES}(t)$.

$$\vec{F}_{z(INERTIAL)}^{WAVES}(t) = \left[\begin{array}{c} 0 \\ 0 \\ \zeta_{swl}(t) \cdot \rho_{SEAWATER} \cdot \pi \cdot r_{swl}^2(t) \cdot g \\ 0 \\ 0 \\ 0 \end{array} \right] \tag{87}$$

The elevation of the waves $\zeta_{swl}(t)$ is determined by Equation (78) using those of the point $p_{VDswl}(t)$ as coordinates X and Y. This point is calculated by finding the intersection of the X-Y plane of the inertial coordinate system with the line formed by two points belonging to the floating platform. This problem is easily solved using the equations of a plane in space and the parametric equations of a line in space.

Equations (83) and (87) are valid for wave lengths much larger than the diameter of the affected cylinder [79,80]. Table 8 shows that the largest diameter of the floating platform is 9.4 m. On the other hand, Table 9 shows that the results obtained with Equations (83) and (87) can be considered acceptable in almost all sea states.

As a last step, with Equation (88) the vector $\vec{F}_{z(BODY)}^{WAVES}(t)$ expressed in the mobile coordinate system is obtained and, through Equation (89), the results of Equations (86) and (88) are added to obtain the vector of wave forces ($\vec{F}_{j(BODY)}^{WAVES}(t)$).

$$\vec{F}_{z(BODY)}^{WAVES}(t) = \left(M_{BODY}^{INERTIAL} \right)^{-1} \cdot \vec{F}_{z(INERTIAL)}^{WAVES}(t) \tag{88}$$

$$\vec{F}_{j(BODY)}^{WAVES}(t) = \vec{F}_{x,y(BODY)}^{WAVES}(t) + \vec{F}_{z(BODY)}^{WAVES}(t) \tag{89}$$

2.7. Vector of Coriolis–Centripetal Forces

This calculation is based on the criterion presented in [60], in which, starting from the rigid body matrix (M_{RB}) broken down as observed in Equation (90) and using Equations (91) and (92), two vectors, $\overset{\rightarrow}{cv}1$ and $\overset{\rightarrow}{cv}2$, are obtained.

$$M_{RB} = \left[\begin{array}{cc} M_{RB(11)} & M_{RB(12)} \\ M_{RB(21)} & M_{RB(22)} \end{array} \right] \tag{90}$$

$$\overset{\rightarrow}{cv}1 = \left[\begin{array}{c} x_{cv1} \\ y_{cv1} \\ z_{cv1} \end{array} \right] = M_{RB(11)} \cdot \left[\begin{array}{c} \overset{\rightarrow}{vv}_{1(BODY)} \\ \overset{\rightarrow}{vv}_{2(BODY)} \\ \overset{\rightarrow}{vv}_{3(BODY)} \end{array} \right] + M_{RB(12)} \cdot \left[\begin{array}{c} \overset{\rightarrow}{vv}_{4(BODY)} \\ \overset{\rightarrow}{vv}_{5(BODY)} \\ \overset{\rightarrow}{vv}_{6(BODY)} \end{array} \right] \tag{91}$$

$$
\overrightarrow{cv2} = \begin{bmatrix} x_{cv2} \\ y_{cv2} \\ z_{cv2} \end{bmatrix} = M_{RB(21)} \cdot \begin{bmatrix} \overrightarrow{vv}_{1(BODY)} \\ \overrightarrow{vv}_{2(BODY)} \\ \overrightarrow{vv}_{3(BODY)} \end{bmatrix} + M_{RB(22)} \cdot \begin{bmatrix} \overrightarrow{vv}_{4(BODY)} \\ \overrightarrow{vv}_{5(BODY)} \\ \overrightarrow{vv}_{6(BODY)} \end{bmatrix} \tag{92}
$$

Vector $\overrightarrow{vv}_{i(BODY)}$ is the velocity vector of the floating system expressed in the mobile coordinate system. The calculation of this vector is explained in detail in [1]. From the vectors calculated in Equations (91) and (92), the Coriolis–centripetal matrix (M_{CC}) is obtained as indicated in Equation (93).

$$
M_{CC} = \begin{bmatrix}
0 & 0 & 0 & 0 & z_{cv1} & -y_{cv1} \\
0 & 0 & 0 & -z_{cv1} & 0 & x_{cv1} \\
0 & 0 & 0 & y_{cv1} & -x_{cv1} & 0 \\
0 & z_{cv1} & -y_{cv1} & 0 & z_{cv2} & -y_{cv2} \\
-z_{cv1} & 0 & x_{cv1} & -z_{cv2} & 0 & x_{cv2} \\
y_{cv1} & -x_{cv1} & 0 & y_{cv2} & -x_{cv2} & 0
\end{bmatrix} \tag{93}
$$

Once the Coriolis–centripetal matrix has been established, the vector of Coriolis–centripetal forces ($F_{j(BODY)}^{\rightarrow CORIOLIS}(t)$) is obtained using Equation (94).

$$
F_{j(BODY)}^{\rightarrow CORIOLIS}(t) = \begin{bmatrix} \overrightarrow{F}_{(BODY)}^{\rightarrow CORIOLIS} \\ \overrightarrow{M}_{(BODY)}^{\rightarrow CORIOLIS} \end{bmatrix} = -M_{CC}(t) \cdot \overrightarrow{vv}_{i(BODY)}(t) \tag{94}
$$

2.8. Turbine Modeling

In this section the modeling of the turbines used in [1] is explained. These have been modeled using the One-Dimensional theory—or Simple theory [66,81]. This methodology considers that the turbine rotor behaves in an ideal way [81], neglecting, for example, friction effects, or not considering the number of turbine blades.

Section 2.8.1 explains in detail the methodology used to obtain the vector of wind turbine forces using One-Dimensional theory, while in Section 2.8.2, the method to apply the methodology explained in Section 2.8.1 and adapted to the modeling of marine current turbines is presented.

2.8.1. Vector of Wind Turbine Forces

As a first step, the effective wind velocity vector ($\overrightarrow{v}_{EFF-WIND(INERTIAL)}(h,t)$) is calculated using Equations (5)–(8), from the simulation wind speed (V_{W-REF}) and the point of application of the vector of wind turbine forces ($F_{WThrust}$), which is the center of mass ($CoM_{WTurbine}$) of the wind turbine (see Figure 12).

In Equation (7), the $\overrightarrow{p}_{point(INERTIAL)}(t)$ point corresponds to the center of mass of the wind turbine ($CoM_{WTurbine}(t)$) expressed in the inertial coordinate system. The center of mass of the wind turbine ($CoM_{WTurbine}$) is calculated from the inertial data of the hub and the three blades of the wind turbine; these data appear in Appendix A of [1]. Table 10 shows part of the data necessary to obtain the vector of wind turbine forces; some of these data appear in Table 7 but are repeated in Table 10 for clarity in the explanation.
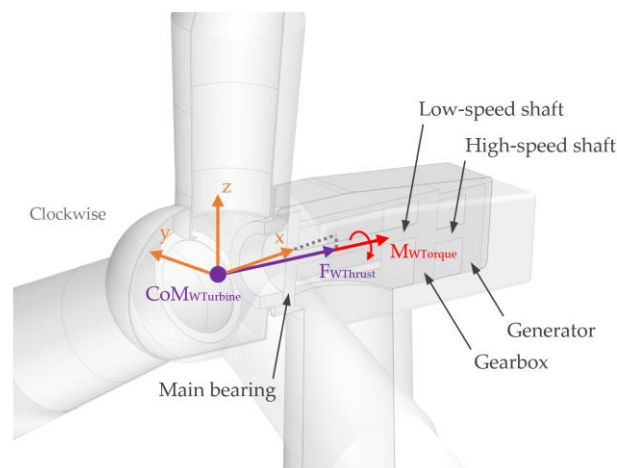
Figure 12. Thrust and torque vectors of wind turbine and its point of application. The axes of the coordinate system that appear in the figure—with its center at $CoM_{WTurbine}$—are parallel to those of the mobile coordinate system.

Table 10. Wind turbine properties.

Property [1]	Value	Symbol
Hub height	90 m	h_{Hub}
Hub radius	1.5 m	r_{Hub}
Blade Length	61.5 m	L_{Blade}
Precone	−2.5 deg	$\varphi_{Precone}$
Shaft tilt	5 deg	$\varphi_{Shaft\ Tilt}$
Gearbox Ratio	97:1	$gearR$
Electrical Generator Efficiency	0.944	$genE$

[1] Source [3].

The next step is to calculate the unit vector ($\overrightarrow{v}_{WThrust(BODY)}$) of the vector of wind turbine forces ($F_{WThrust}$); this is carried out by applying Equation (95) from the data in Table 10, where δ is the wind direction. This vector is aligned with the high-speed shaft, which is inclined 5 degrees ($\varphi_{Shaft\ Tilt}$) with respect to the Y axis of the mobile coordinate system (see Figure 12).

$$\overrightarrow{v}_{WThrust(BODY)} = \begin{bmatrix} \cos\delta & -\sin\delta & 0 \\ \sin\delta & \cos\delta & 0 \\ 0 & 0 & 1 \end{bmatrix} \cdot \begin{bmatrix} \cos\left(\varphi_{Shaft\ Tilt} \cdot \frac{\pi}{180}\right) & 0 & \sin\left(\varphi_{Shaft\ Tilt} \cdot \frac{\pi}{180}\right) \\ 0 & 1 & 0 \\ -\sin\left(\varphi_{Shaft\ Tilt} \cdot \frac{\pi}{180}\right) & 0 & \cos\left(\varphi_{Shaft\ Tilt} \cdot \frac{\pi}{180}\right) \end{bmatrix} \cdot \begin{bmatrix} 1 \\ 0 \\ 0 \end{bmatrix} \quad (95)$$

The vector of wind turbine forces ($F_{WThrust}$) is obviously not aligned with the effective wind velocity vector ($\overrightarrow{v}_{EFF-WIND(INERTIAL)}(h,t)$) for different reasons: the shaft tilt angle, the movement of the floating system due to buoyancy, sea currents, the waves, etc. To model this situation, the vector projection [68] of the effective wind velocity vector ($\overrightarrow{v}_{EFF-WIND(BODY)}(h,t)$)—expressed in the mobile coordinate system by Equation (96)—is calculated on the unit vector in the direction of the force ($\overrightarrow{v}_{WThrust(BODY)}$). This is calculated using Equation (97), and the symbol * in the equation means the scalar product of the two vectors.

$$\overrightarrow{v}_{EFF-WIND(BODY)}(h,t) = \left(M_{BODY}^{INERTIAL}\right)^{-1} \cdot \overrightarrow{v}_{EFF-WIND(INERTIAL)}(h,t) \quad (96)$$

$$\vec{v}_{EFF-WThrust(BODY)}(t) = \vec{v}_{WThrust(BODY)} \cdot \frac{\vec{v}_{EFF-WIND(BODY)}(h,t) * \vec{v}_{WThrust(BODY)}}{\left|\vec{v}_{WThrust(BODY)}\right|^2} \tag{97}$$

$$V_{1-2}(t) = \left|\vec{v}_{EFF-WThrust(BODY)}(t)\right| \tag{98}$$

The magnitude of the effective velocity vector ($\vec{v}_{EFF-WThrust(BODY)}(t)$) on the wind turbine calculated in Equation (97) is named as $V_{1-2}(t)$ in Equation (98) for simplicity in subsequent calculations and for consistency with the nomenclature used in [66].

Table 11 shows different data that condition the behavior of the wind turbine to apply the One-Dimensional theory.

Table 11. Rotor speed, axial induction factor, and pitch angle as a function of wind speed.

Wind Speed [1] V_{W-REF} (m/s)	Rotor Speed [2] Ω (rpm)	Axial Induction Factor $axif$ (-)	Pitch Angle [2] φ_{pitch} (deg)
3	6.97	0.219414	0
4	7.18	0.200177	0
5	7.51	0.186398	0
6	7.94	0.176555	0
7	8.47	0.172797	0
8	9.16	0.165412	0
9	10.3	0.165851	0
10	11.43	0.166114	0
11	11.89	0.163337	0
11.4	12.1 [3]	0.155162	0

[1] Wind speeds at 90 m reference height. [2] Source [61]. [3] Rated rotor speed.

As observed in Table 11, neither in [1] nor in this work have simulations been carried out with wind speeds higher than 11.4 m/s because, from this wind speed, it is necessary to apply a certain pitch angle to the blades, which has not been modeled using One-Dimensional theory. In an upcoming work, the modeling of the turbines will be explained using the Blade Element Momentum theory, with which the behavior of the turbines is modeled when a pitch angle greater than 0 degrees can be applied.

To complete the calculation of the vector of wind turbine forces, it is necessary to calculate the magnitude of the force. This is achieved by applying the One-Dimensional theory. Table 11 shows the data of the axial induction factor ($axif$) for different wind speeds (V_{W-REF}). After evaluating different options, the authors decided to deduce the $axif$ values necessary to obtain the expected power for each wind speed, according to the operation of the wind turbine described in [3]. An adequate adjustment of the $axif$ values has been possible, validating the results for each wind speed—with the version of the OC3-Hywind [2] implemented in FHYGSYS (see Appendix E of [1])—using FASTv8.

The calculation process continues with Equations (99)–(101) from the data in Tables 10 and 11. With them, the radius ($r_{Turbine}$) and the area ($A_{Turbine}$) of the wind turbine, and the power coefficient (C_P) are calculated respectively.

$$r_{Turbine} = (L_{Blade} + r_{Hub}) \cdot \cos(\varphi_{Precone}) \tag{99}$$

$$A_{Turbine} = \pi \cdot \left[r_{Turbine}^2 - r_{Hub}^2\right] \tag{100}$$

$$C_P = 4 \cdot axif \cdot (1 - axif)^2 \tag{101}$$

For the calculation process, two assumptions are made: the values of axial induction factor ($axif$) and angular speed of the turbine (Ω) are considered constant for a given wind

speed (V_{W-REF}), taking the values expressed in Table 11. For intermediate wind speeds, linear interpolation is performed from the data in this table.

The next step is to calculate the tip speed ratio ($TSR(t)$) by means of Equation (102), and with it, the angular induction factor ($anif(t)$) is obtained through Equation (103). Both equations are extracted from [66].

$$TSR(t) = \frac{\Omega \cdot r_{Turbine}}{V_{1-2}(t)} \tag{102}$$

$$anif(t) = \frac{1}{2} \cdot \left(\sqrt{1 + \frac{4 \cdot axif \cdot (1 - axif)}{TSR^2(t)}} - 1 \right) \tag{103}$$

As a previous step to the calculation of the thrust and the moment produced in the turbine, with Equation (104)—extracted from [66,81]—the speed of the wind far upstream of the rotor ($V_0(t)$) is determined. This velocity is time-dependent due to the assumption that the $axif$ is constant.

$$V_0(t) = \frac{V_{1-2}(t)}{(1 - axif)} \tag{104}$$

Then, using Equations (105) and (106)—extracted from [66,81]—the magnitudes of the thrust ($T(t)$) and moment ($Q(t)$) vectors originated in the turbine are calculated.

$$T(t) = \int_{r\_hub}^{r\_turbine} \rho_{AIR} \cdot V_0^2(t) \cdot 4 \cdot axif \cdot (1 - axif) \cdot \pi \cdot r \cdot dr \tag{105}$$

$$Q(t) = \int_{r\_hub}^{r\_turbine} \rho_{AIR} \cdot V_0(t) \cdot \Omega \cdot (r_{turbine} - r_{hub})^2 \cdot 4 \cdot anif(t) \cdot (1 - axif) \cdot \pi \cdot r \cdot dr \tag{106}$$

It should be noted that these integrals are solved by applying the trapezoidal rule [69] and that the air density (ρ_{AIR}) appears in Table 4. Next, through Equations (107) and (108) the thrust ($\vec{F}_{WThrust(BODY)}(t)$) and moment ($\vec{M}_{WTorque(BODY)}(t)$), vectors are obtained from the unit vectors ($\vec{v}_{WTorque(BODY)} = \vec{v}_{WThrust(BODY)}$) of both (see Figure 12).

$$\vec{F}_{WThrust(BODY)}(t) = \vec{v}_{WThrust(BODY)} \cdot T(t) \tag{107}$$

$$\vec{M}_{WTorque(BODY)}(t) = \vec{v}_{WTorque(BODY)} \cdot Q(t) \tag{108}$$

Finally, the moment ($\vec{M}_{WThrust(BODY)}(t)$) produced by the thrust vector at the origin of the mobile coordinate system is calculated with Equation (109).

$$\vec{M}_{WThrust(BODY)}(t) = CoM_{WTurbine(BODY)} \times \vec{F}_{WThrust(BODY)}(t) = \begin{vmatrix} \vec{i} & \vec{j} & \vec{k} \\ x_{CoM} & y_{CoM} & z_{CoM} \\ F_x & F_y & F_z \end{vmatrix} \tag{109}$$

As a last step, using Equation (110), the moment originated by the thrust vector is added to that produced in the turbine, thus obtaining the vector of wind turbine forces and moments ($\vec{F}_{j(BODY)}^{\rightarrow WIND\ TURBINE}(t)$).

$$\vec{F}_{j(BODY)}^{\rightarrow WIND\ TURBINE}(t) = \begin{bmatrix} \vec{F}_{WThrust(BODY)}(t) \\ \vec{M}_{WThrust(BODY)}(t) + \vec{M}_{WTorque(BODY)}(t) \end{bmatrix} \tag{110}$$

Additionally, FHYGSYS calculates other important magnitudes that help to study the behavior of the wind turbine: electrical power ($P_{ELE}(t)$), mechanical power ($P_{MEC}(t)$),

torque produced in the electrical generator ($Q_{GEN}(t)$), and thrust coefficient ($C_T(t)$). These magnitudes are, respectively, calculated with Equations (111)–(114). Equation (111) is extracted from [66,81], Equation (112) represents the power generator efficiency, Equation (113) is deducted from [3,61], and Equation (114) is extracted from [81].

$$P_{ELE}(t) = \frac{1}{2} \cdot \rho_{AIR} \cdot A_{Turbine} \cdot V_{1-2}^3(t) \cdot 4 \cdot axif \cdot (1 - axif)^2 \tag{111}$$

$$P_{MEC}(t) = \frac{P_{ELE}(t)}{genE} \tag{112}$$

$$Q_{GEN}(t) = \frac{Q(t)}{gearR} \cdot genE \tag{113}$$

$$C_T(t) = \frac{T(t)}{\frac{1}{2} \cdot \rho_{AIR} \cdot A_{Turbine} \cdot V_{1-2}^2(t)} \tag{114}$$

All the equations indicated in this section, as well as the *axif* data included in Table 11, have been validated with simulations under equivalent conditions by means of FASTv8, using the version of the OC3-Hywind [2] implemented in FHYGSYS (see Section 3, Appendix B of this work, and Appendix E of [1]).

2.8.2. Vector of Marine Current Turbine Forces

As previously indicated, the modeling of marine current turbines used in [1] and in this work is based on the methodology explained in Section 2.8.1. In this section, the modeling of marine current turbines is presented, making reference to the concepts explained and the equations shown in the previous section. As indicated in [1] and throughout this work, the floating hybrid system has two marine current turbines. The explanation given in this section refers to the modeling of one of them, but the methodology is applicable to both, considering the direction of $\overrightarrow{M}_{MCTorque}$ according to the case (see Figure 13).
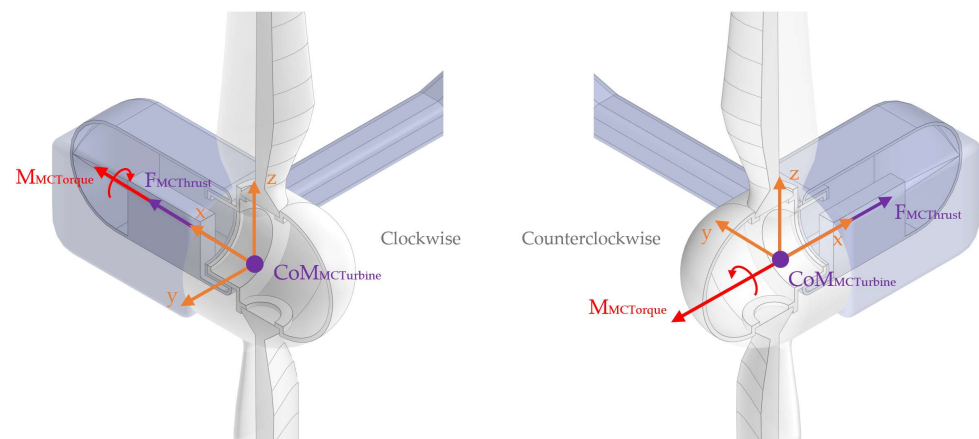

Figure 13. Thrust and torque vectors of marine current turbines and their points of application. The axes of the coordinate systems that appear in the figure—with their centers in each $CoM_{MCTurbine}$—are parallel to those of the mobile coordinate system.

The calculation also starts from—in this case—the effective current velocity vector ($\overrightarrow{v}_{EFF-SSCURR(INERTIAL)}(h,t)$), calculated using Equations (9)–(11) as explained in Section 2.3.2. The data needed to use these equations are the current velocity (V_{SWL}) and the point of application of the vector of marine current turbine forces ($F_{MCThrust}$), which is also the center of mass ($CoM_{MCTurbine}$) of the marine current turbine (see Figure 13).

In this case, in Equation (7), the $\overrightarrow{p}_{point(INERTIAL)}(t)$ point corresponds to the center of mass of the marine current turbine ($CoM_{MCTurbine}$) expressed in the inertial coordinate

system. This center of mass is also calculated from the inertial data—of each one of the marine current turbines—included in Appendix A of [1]. Table 12 contains part of the data needed to calculate the vector of marine current turbine forces.

Table 12. Marine current turbine properties.

Property	Value	Symbol
Hub depth [1]	−20 m	h_{Hub}
Hub radius [1]	1 m	r_{Hub}
Blade Length [1]	9 m	L_{Blade}
Precone [1]	0 deg	$\varphi_{Precone}$
Shaft tilt [1]	0 deg	$\varphi_{Shaft\ Tilt}$
Gearbox Ratio [2]	97:1	$gearR$
Electrical Generator Efficiency [2]	0.944	$genE$

[1] Source [4]. [2] Estimated data equal to those of the wind turbine.

As in the previous case, as a starting point for the calculation process, the unit vector ($\vec{v}_{MCThrust(BODY)}$) of the vector of marine current turbine forces must be found (see Figure 13). This is achieved by Equation (115) from the data in Table 12, where ε is the direction of the sub-surface current.

$$\vec{v}_{MCThrust(BODY)} = \begin{bmatrix} \cos\varepsilon & -\sin\varepsilon & 0 \\ \sin\varepsilon & \cos\varepsilon & 0 \\ 0 & 0 & 1 \end{bmatrix} \cdot \begin{bmatrix} \cos\left(\varphi_{Shaft\ Tilt}\cdot\frac{\pi}{180}\right) & 0 & \sin\left(\varphi_{Shaft\ Tilt}\cdot\frac{\pi}{180}\right) \\ 0 & 1 & 0 \\ -\sin\left(\varphi_{Shaft\ Tilt}\cdot\frac{\pi}{180}\right) & 0 & \cos\left(\varphi_{Shaft\ Tilt}\cdot\frac{\pi}{180}\right) \end{bmatrix} \cdot \begin{bmatrix} 1 \\ 0 \\ 0 \end{bmatrix} \quad (115)$$

Similarly, the vector of marine current turbine forces ($F_{MCThrust}$) is not aligned with the effective current velocity vector ($\vec{v}_{EFF-SSCURR(INERTIAL)}(h,t)$). Therefore, this situation must be compensated using Equations (96)–(98) in a similar way, from the vectors $\vec{v}_{EFF-SSCURR(INERTIAL)}(h,t)$ and $\vec{v}_{MCThrust(BODY)}$, obtaining as a result the magnitude ($V_{1-2}(t)$) of the effective velocity vector in marine current turbine ($\vec{v}_{EFF-MCThrust(BODY)}(h,t)$).

In this case, Table 13 contains the data that establish the behavior of marine current turbines for applying the One-Dimensional theory.

Table 13. Rotor speed, axial induction factor, and pitch angle as a function of current speed.

Sub-Surface Current Speed [1] V_{SWL} (m/s)	Rotor Speed [2] Ω (rpm)	Axial Induction Factor $axif$ (-)	Pitch Angle [2] φ_{pitch} (deg)
0.5	3.37	0.221552	0
0.65	4.363	0.211013	0
0.8	5.356	0.212288	0
0.95	6.349	0.212249	0
1.1	7.35	0.205184	0
1.25	8.355	0.201525	0
1.4	9.36	0.201909	0
1.55	10.21	0.194966	0
1.7	10.77	0.194207	0
1.85	11.32	0.194904	0
1.9	11.5 [3]	0.193221	0

[1] Current speeds at still water level. [2] Source [4]. [3] Rated rotor speed.

In Table 13, the data of the axial induction factor ($axif$) have been deduced from the behavior data of marine turbines described in [4,5].

For the application of the One-Dimensional theory, the same two assumptions have been made as in the previous section: the values of the axial induction factor ($axif$) and the turbine rotation speed (Ω) are considered constant. These values are extracted for a given

current speed (V_{SWL}). Linear interpolation is also performed with the data in Table 13 in the case of intermediate values of current speed. Likewise, no simulations have been carried out, either in [1] or in this work, with current velocity values (V_{SWL}) greater than 1.9 m/s since it would be necessary to include the effect of a certain pitch angle and this situation has not been modeled with the One-Dimensional theory.

Finally, from the data in Tables 12 and 13 and the value of $V_{1-2}(t)$, the One-Dimensional theory is applied through Equations from (99)–(110), obtaining with this last equation the vector of marine current turbine forces and moments ($\vec{F}_{j(BODY)}^{\rightarrow CURRENT\ TURBINE}$).

The only difference is that, in Equation (108), while the unit vector of the clockwise turbine $\vec{v}_{MCTorque(BODY)}$ is equal to the unit vector $\vec{v}_{MCThrust(BODY)}$, for the counterclockwise turbine, these vectors are opposite ($\vec{v}_{MCTorque(BODY)} = -\vec{v}_{MCThrust(BODY)}$), this is easily verified by observing Figure 13.

3. Results

In order to present the results obtained from the mathematical modeling described in [1] and in this work, a simulation has been chosen with the version of OC3-Hywind [2] implemented with the FHYGSYS simulation tool. In Appendix E of [1], the differences between the inertial data of the OC3-Hywind version of FHYGSYS and those of the floating system that incorporates the marine current turbines (see Figure 1) are explained.

This means that the results presented in this section do not include marine current turbines, thus allowing a code-to-code comparison of the mathematical model with FASTv8. In Appendix E of [1], a code-to-code comparison of the FHYGSYS tool was already included using the mathematical modeling described in [1] and in this work but without including wave action. Since the final objective of the development of FHYGSYS is to have a tool that allows for testing different automatic control strategies of the floating system, it is especially interesting to carry out simulations with the inclusion of waves because the waves can cause instabilities in the floating system that the automatic control system must be able to minimize.

The simulation that has been chosen for the presentation of results includes the action of the wind, the marine sub-surface current and the waves (see Supplementary Materials Video S1: Results_Test). The values used for the simulation appear in Table 14, and Figure 14 illustrates the floating system and the corresponding thrust vectors that influence it.

Table 14. Test conditions.

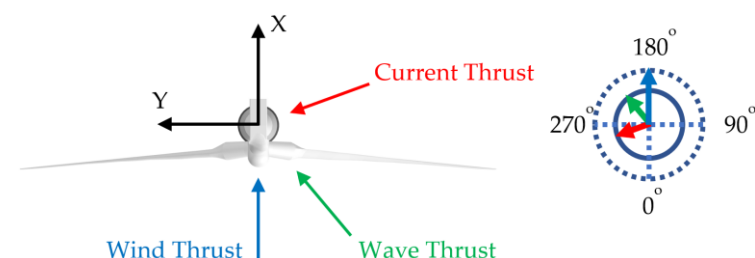| Wind Speed	Wind Direction	Sub-Surface Current Speed	Sub-Surface Current Direction	Wave Height	Wave Period	Wave Direction
10 m/s	0 deg	1.1 m/s	110 deg	6 m	10 s	40 deg

Figure 14. Position of the thrust vectors on the floating system for the test.

The adjustment of the FASTv8 parameters to carry out a simulation with the same conditions as with FHYGSYS is the same as that indicated in the introduction of Appendix E of [1], with the differences indicated in Tables 15–18.

Table 15. Changes in "NRELOffshrBsline5MW_OC3Hywind_ElastoDyn.dat".

Section	Parameter	Original Value	Modified Value
INITIAL CONDITIONS	RotSpeed	12.1	11.43

Table 16. Changes in "NRELOffshrBsline5MW_InflowWind_12mps.dat".

Section	Parameter	Original Value	Modified Value
Parameters for Steady Wind Conditions	HWindSpeed	0	10

Table 17. Changes in "NRELOffshrBsline5MW_OC3Hywind_HydroDyn.dat".

Section	Parameter	Original Value	Modified Value
WAVES	WaveMod	2	2
	WaveHs	6	6
	WaveTp	10	10
	WaveDir	0	40
	CurrMod	0	1
CURRENT	CurrSSV0	0	1.1
	CurrSSDir	"DEFAULT"	110

Table 18. Inclusion in "NRELOffshrBsline5MW_OC3Hywind_HydroDyn.dat"—OutList section—new output parameters.

Parameter	Description	Units
WavesFxi	Total wave-excitation loads	(N)
WavesFyi	from diffraction at the WRP	(N)
WavesFzi	(force in x, y, z directions)	(N)
WavesMxi	Total wave-excitation loads	(N·m)
WavesMyi	from diffraction at the WRP	(N·m)
WavesMzi	(moment in x, y, z directions)	(N·m)

As indicated in previous paragraphs, the results presented in this section include the action of the waves; this causes, in all the graphs, signals of sinusoidal origin corresponding to the influence of the waves on the magnitude represented appearing superimposed. Firstly, Figure 15 shows the representation of the six degrees of freedom of the floating system.
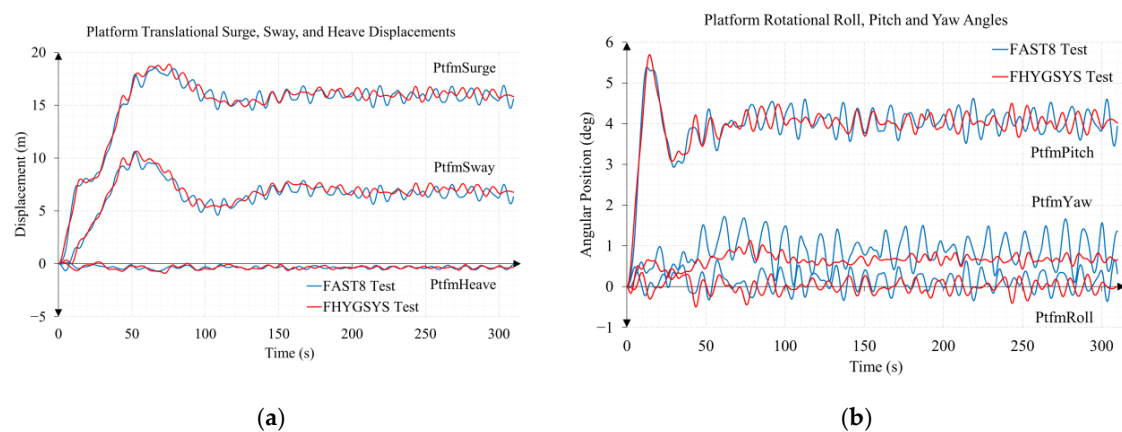
Figure 15. Linear and angular degrees of freedom: (**a**) linear degrees of freedom; (**b**) angular degrees of freedom.

Figure 15 shows the most important magnitudes that allow for comparing the behavior of FHYGSYS with respect to FASTv8. These are the displacements in the surge, sway, and heave directions and the rotations about the X, Y, and Z axes of the inertial coordinate system, roll, pitch, and yaw. This is the main result of applying the mathematical model presented in [1] and completed in this work. Considering the main objective of the development of FHYGSYS—explained previously—the first conclusion is that a tool has been achieved, which will allow, in future works, for this type of floating system to be evaluated from the point of view of the development of automatic control systems.

Other important results, those corresponding to the total hydrodynamic loads, are shown in Figure 16. They represent the sum of all the hydrodynamic loads that act on the floating system.
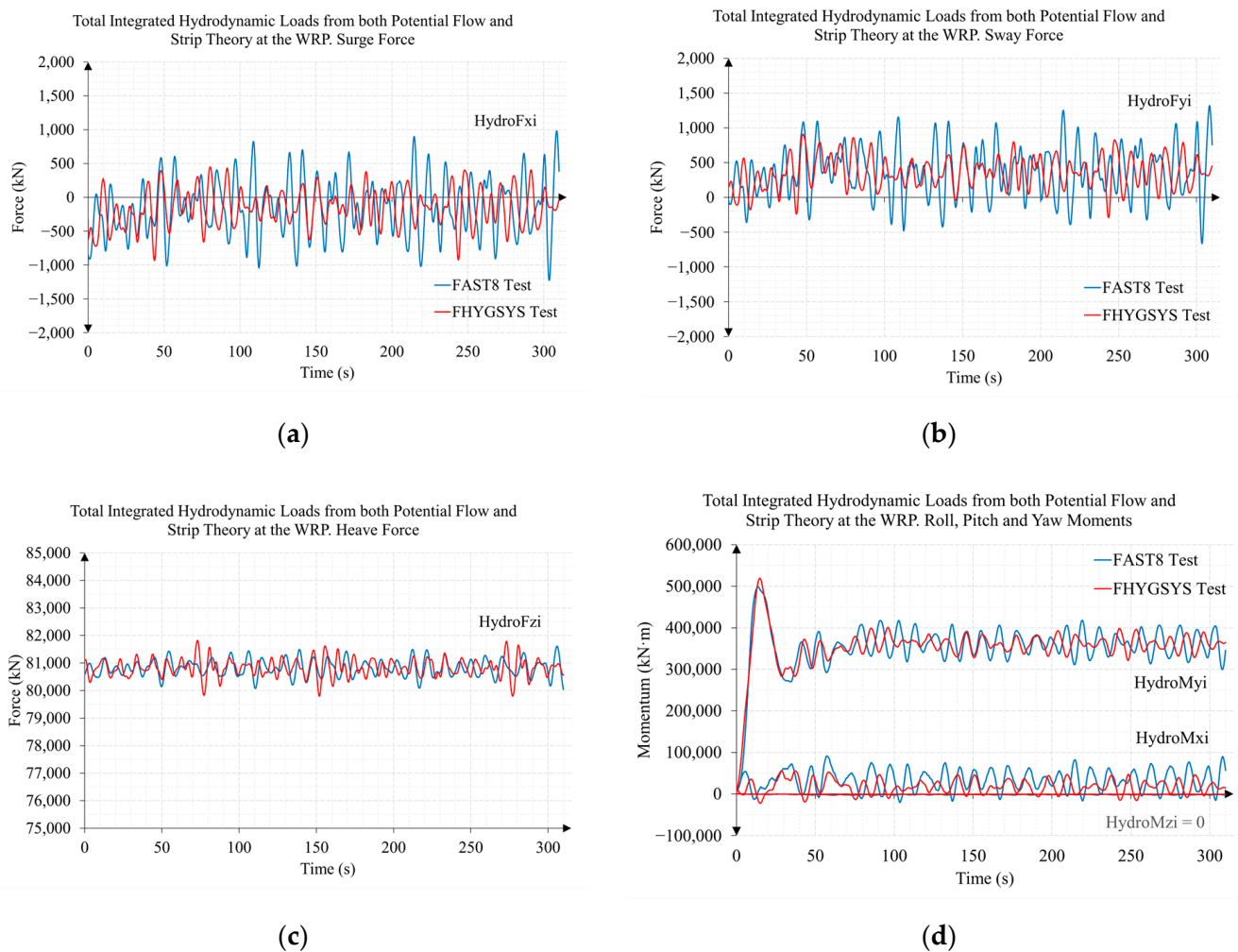
Figure 16. Total integrated hydrodynamic loads from both potential flow and strip theory at the WRP: (**a**) surge force; (**b**) sway force; (**c**) heave force; (**d**) roll, pitch, and yaw moments.

These results—which are described in detail in Section 2.6—can be considered acceptable for the purpose of FHYGSYS. In Figure 16 and the following, WRP means WAMIT Reference Point, this point corresponds to the origin of coordinates of the inertial coordinate system [82] (see Figures 3 and 4). To carry out the code-to-code comparison, all the forces obtained with FHYGSYS have also been expressed in the initial coordinate system.

The results shown in Figures 15 and 16 show a greater amplitude in the sinusoidal component of the magnitudes obtained with FASTv8. During the development of the wave modeling, it was observed that, by modifying the seeds that generate Gaussian white noise ($W(\omega)$), the amplitude of the sinusoidal component of the magnitudes obtained with

FHYGSYS also varied. For this reason, these amplitude differences are not considered a modeling error. The decision was made to use the same seeds used by FASTv8 (see Section 2.6.5) to aid in the FHYGSYS validation process, but simulations can be performed with others if desired. This difference in the amplitude of the sinusoidal components appears in many of the graphs presented in this section and in the following ones. In Appendix B, the results are shown under the same conditions as in this section but with five different pairs of seeds. The references that appear together with the magnitudes obtained within the graphs correspond to the references used in the HydroDyn package [82] used by FASTv8. The same happens with the title of each of the graphs.

3.1. Mooring System Modeling

Figure 17 shows the evolution of the tensions in each of the fairleads of the floating platform.
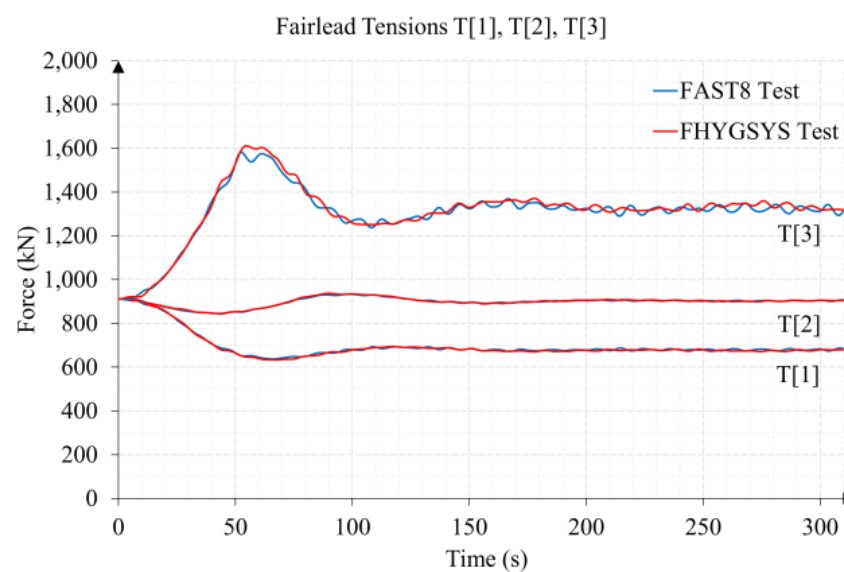
Figure 17. Force on the fairleads of the floating platform of each mooring line. In this figure, T[1], T[2] and T[3] are the nomenclature used by FASTv8 for the Fairlead Tensions in mooring lines 1, 2 and 3.

Observing Figures 5, 14 and 17, the behavior of the tensions in the fairleads can be related. In fact, it is verified that due to the orientation of the thrust vectors of the currents and waves, mooring line 3 is the one that suffers the greatest stress.

The results show the sinusoidal component due to the waves, discussed in the previous section, an issue that does not preclude accepting the modeling described in Section 2.4. In Appendix E of [1], more examples of mooring system modeling comparison between FASTv8 and FHYGSYS are shown.

3.2. Gravitational and Buoyancy Modeling

The comparison of the gravitational and hydrostatic forces—called restoring forces [60]—is performed jointly because, in most cases, a combination of these two forces is carried out for modeling [60]. It is probably for this reason that gravitational forces have not been found separately in FASTv8. They are two opposite forces (see Figure 9) and with a similar order of magnitude that allows their combination to simplify modeling. In FHYGSYS and in this work, it has been decided to model the two forces separately for simplicity in their formulations and for clarity in their explanation.

Figure 18 shows the comparison of the results of the hydrostatic forces, concluding from its observation that the results obtained are acceptable for the objectives set.
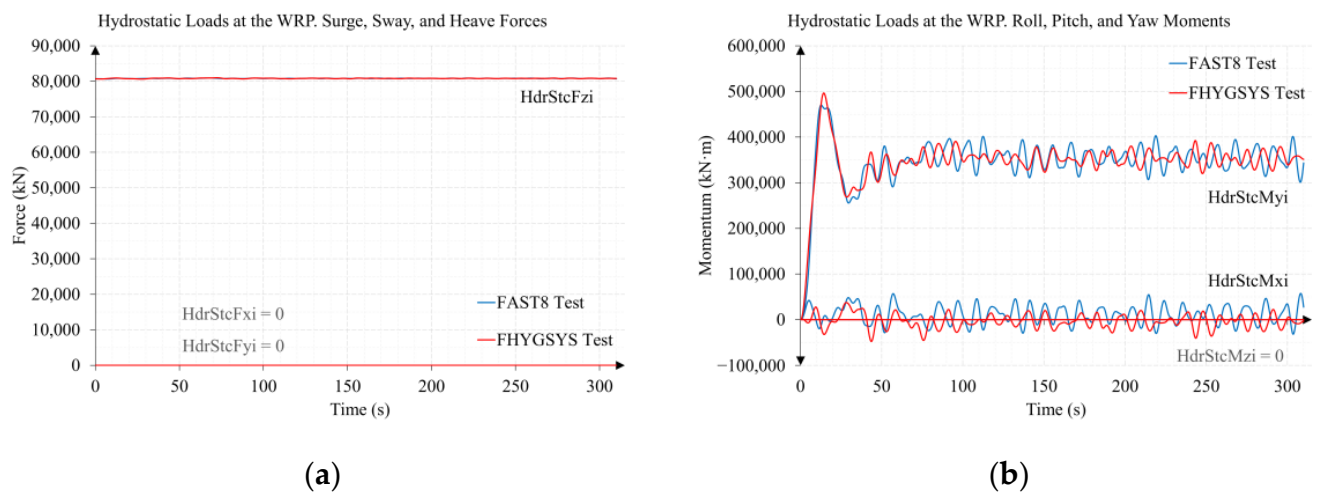
Figure 18. Hydrostatic loads at the WRP: (**a**) forces; (**b**) moments.

Figure 19 shows an enlargement of the heave force to observe in more detail this force of a high magnitude. This figure can also be compared with Figure 16c, noting that the origin of the greater amplitude of the sinusoidal component does not come from the modeling of hydrostatic forces.
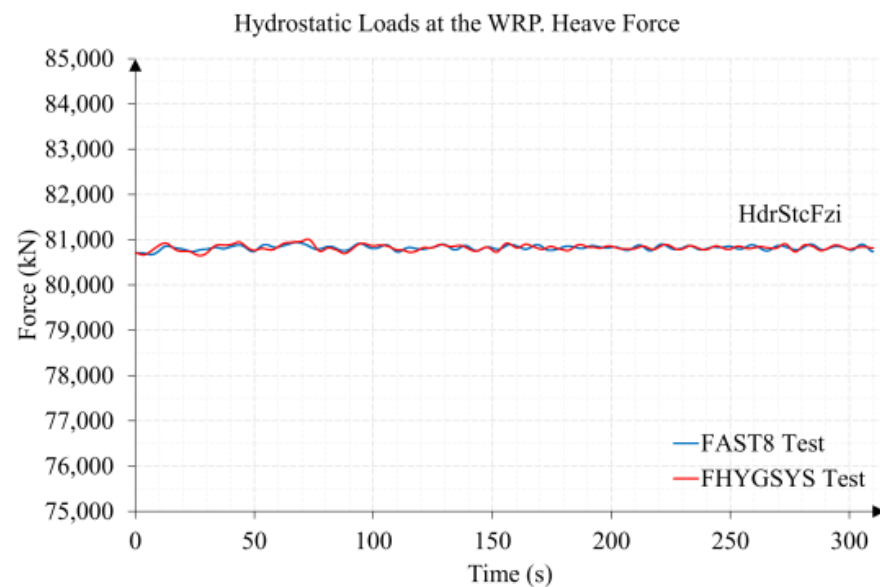

Figure 19. Hydrostatic loads at the WRP. Heave force.

3.3. Additional Damping and Stiffness Modeling

Figure 20 shows the results of the modeling of the additional damping and stiffness. A similar evolution is observed in all degrees of freedom, highlighting a more pronounced difference in the yaw moment. This difference is already observed in Figure 16d and is due to differences in modeling between the two tools. Summarizing, on the one hand, the differences in the modeling of the waves are observed and, on the other hand, the differences already observed in AddMzi in the comparison of results are presented in Appendix E of [1].
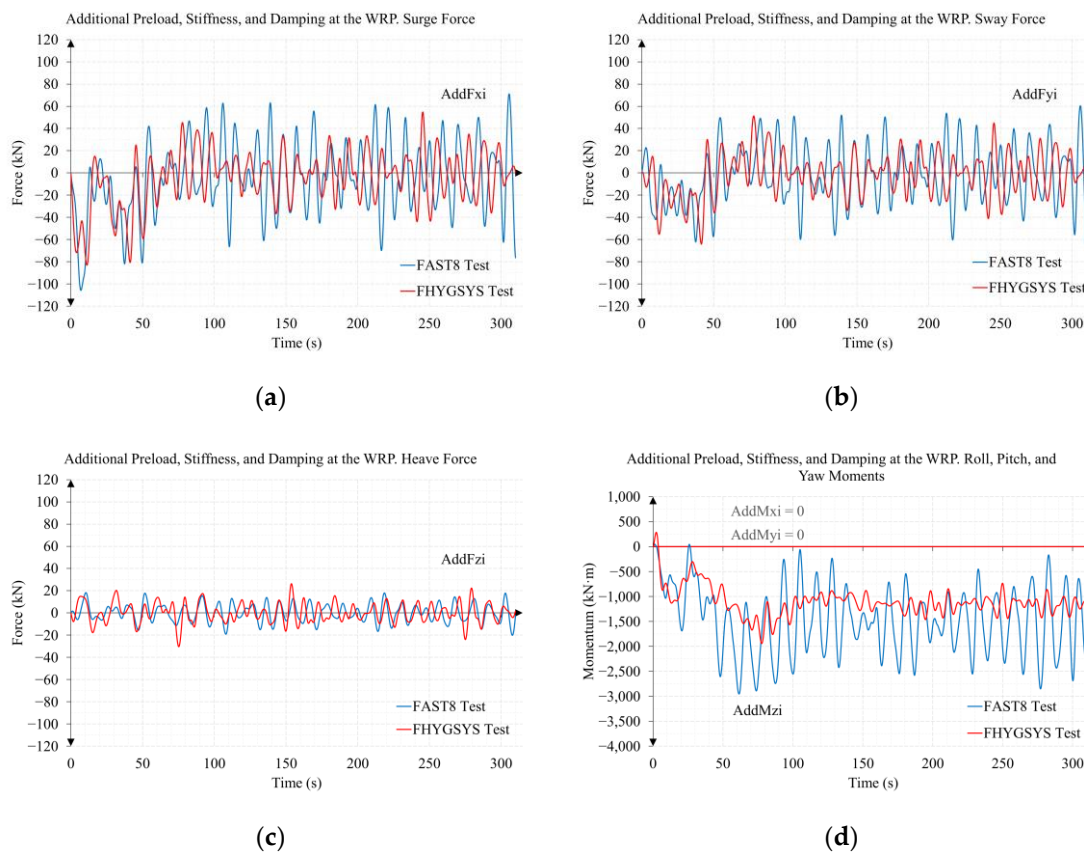
Figure 20. Additional preload, stiffness, and damping at the WRP: (**a**) surge force; (**b**) sway force; (**c**) heave force; (**d**) roll, pitch, and yaw moments.

3.4. Added Mass Modeling

Figure 21 shows the graphs of the radiation loads, also known as the loads due to the added mass. In them, it is inferred that the trend is similar, but the responses are very much masked by the Gaussian white noise ($W(\omega)$) that the waves incorporate. In Appendix E of [1], the results of the comparisons of these forces with a very high coincidence can be observed.

3.5. Viscous Drag Modeling

To compare the results of modeling of viscous drag forces, FASTv8 does not directly provide these results, but they can be obtained indirectly by subtracting all others from the total hydrodynamic loads. Thus, the total integrated hydrodynamic loads from both potential flow and strip theory ($HydroFji$ and $HydroMji$) are subtracted from the hydrostatic loads ($HdrStcFji$ and $HdrStcMji$), the additional damping and stiffness loads ($AddFji$ and $AddMji$), the radiation loads ($RdtnFji$ and $RdtnMji$), and the wave-excitation loads ($WavesFji$ and $WavesMji$), yielding as a result, the viscous drag loads ($ViscDFji$ and $ViscDMji$). This is expressed mathematically through Equations (116) and (117).

$$ViscDFji = HydroFji - HdrStcFji - AddFji - RdtnFji - WavesFji \tag{116}$$

$$ViscDMji = HydroMji - HdrStcMji - AddMji - RdtnMji - WavesMji \tag{117}$$

Figure 22 shows the results obtained, in which it is verified that the trend of the graphs is the same, but in this case, in the responses of FHYGSYS, a greater amplitude of the sinusoidal components is observed.
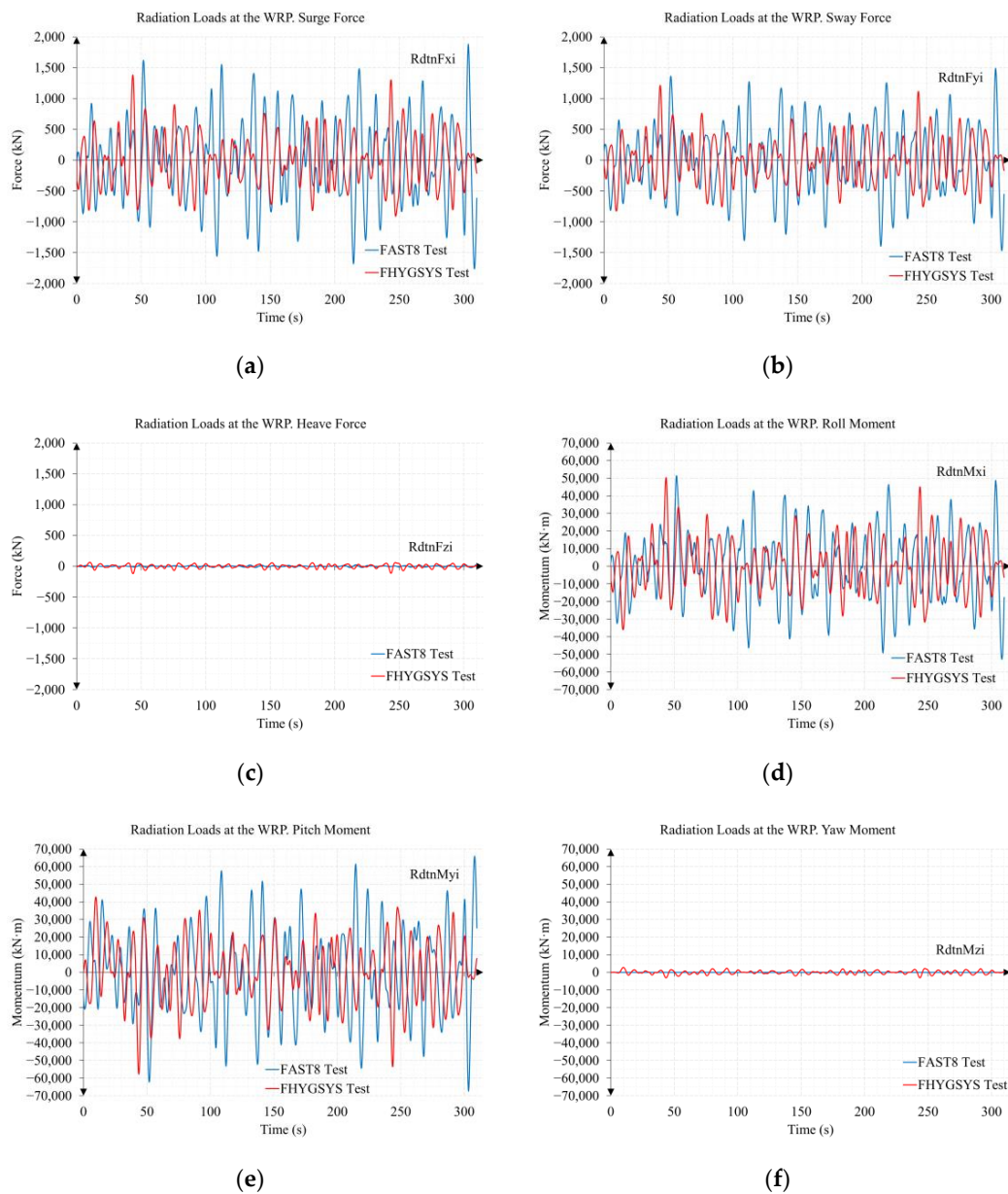
Figure 21. Radiation loads at the WRP: (**a**) surge force; (**b**) sway force; (**c**) heave force; (**d**) roll moment; (**e**) pitch moment; (**f**) yaw moment.
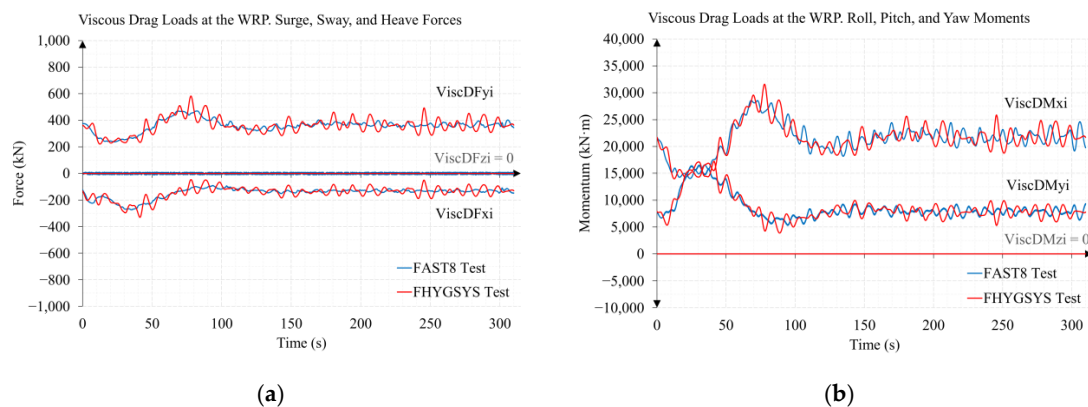

Figure 22. Viscous drag loads at the WRP: (**a**) surge, sway, and heave forces; (**b**) roll, pitch, and yaw moments.

3.6. Wave Modeling

As previously indicated, the inclusion of waves in the modeling of the floating system provides an ideal tool for the development of automatic control systems for this type of system.

Figure 23 shows the total wave elevation; as explained in Section 2.6.5, it is calculated using Equation (78), and it is an important magnitude since it is needed to calculate the Z component of the force of the incident waves.
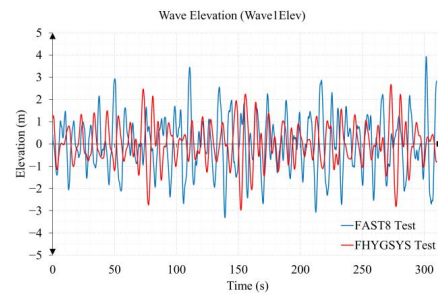
Figure 23. Total wave elevation at the WRP.

As already mentioned, the wave spectrum obtained depends on Gaussian white noise ($W(\omega)$), more specifically on the seeds used to generate it. By varying the values of the seeds, other values of this magnitude are generated, consequently affecting the rest of the magnitudes that act on the floating system. In Appendix B, the results are shown under the same conditions as in this section but with five different pairs of seeds. Figure 24 shows the components of the wave loads, in which a certain correlation is observed in the amplitude in the different graphs. In the wave period, this correlation is not observed, but as already indicated, this is due to the modeling differences between the two tools.
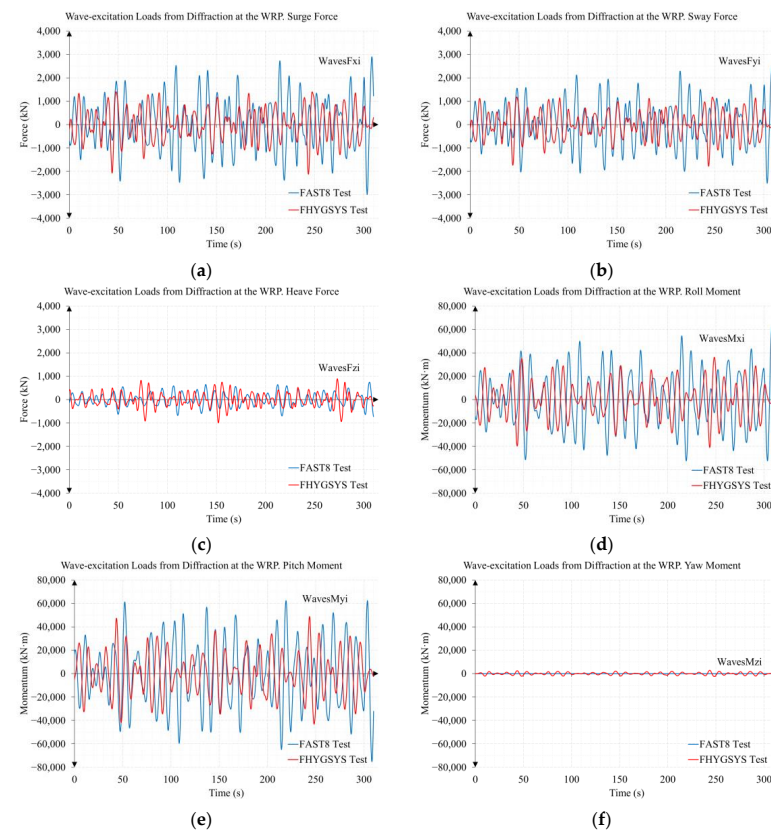

Figure 24. Total wave-excitation loads from diffraction at the WRP: (**a**) surge force; (**b**) sway force; (**c**) heave force; (**d**) roll moment; (**e**) pitch moment; (**f**) yaw moment.

3.7. Coriolis–Centripetal Modeling

Coriolis–Centripetal modeling cannot be directly compared with values obtained with FASTv8. However, it can be indirectly compared by observing the responses of the six degrees of freedom shown in Figure 15. As explained in Section 2.7, these forces depend on the speed of the floating system, so they contribute to the transient part of these responses being more appropriate when comparing the results obtained with the two tools.

3.8. Wind Turbine Modeling

Figure 25 shows the results of the comparison between FASTv8 and FHYGSYS referring to the wind turbine. In them, it is verified that the modeling exposed in Section 2.8.1 can be considered appropriate, fulfilling the objectives of the development of FHYGSYS. In Appendix E of [1], other comparisons without the inclusion of waves are shown.
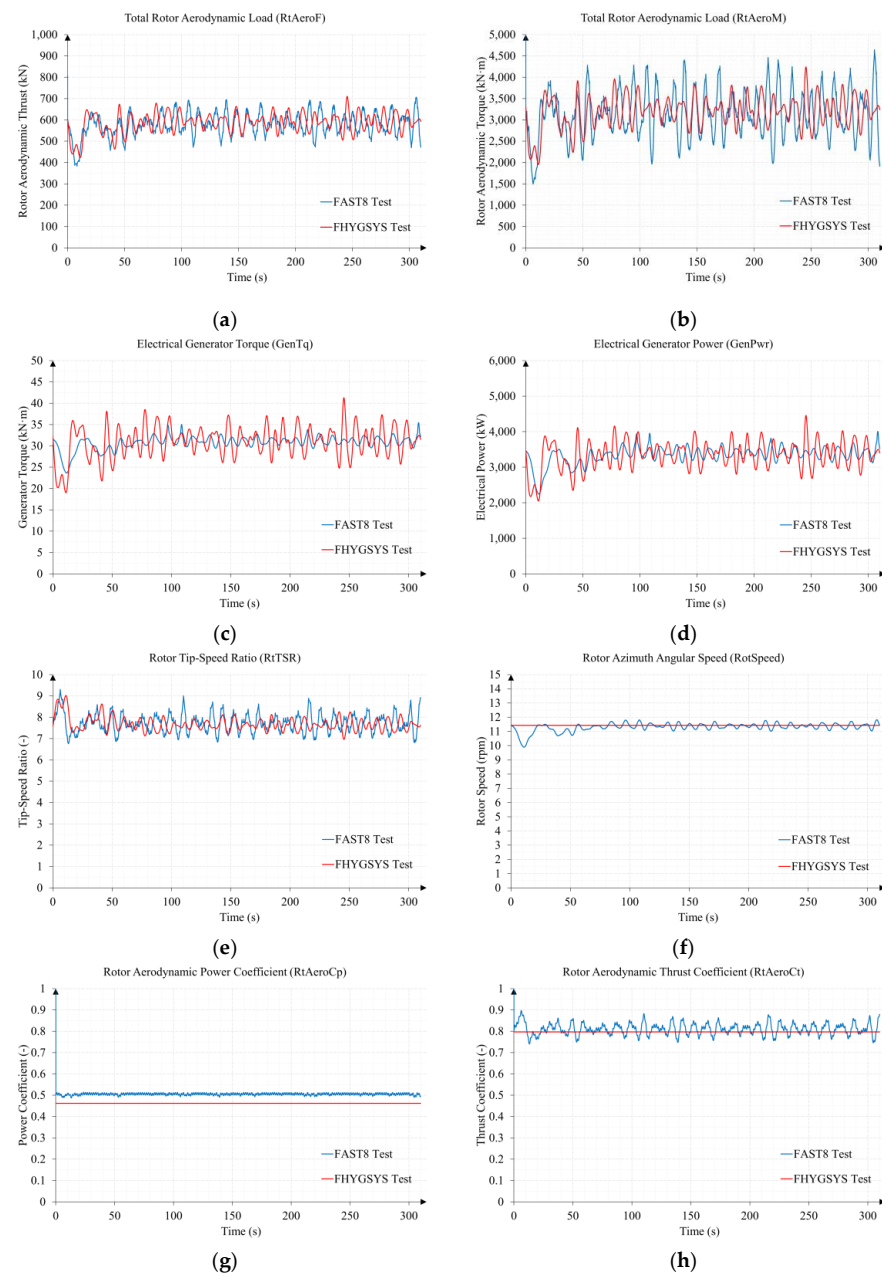

Figure 25. Wind turbine modeling results: (**a**) rotor thrust; (**b**) rotor torque; (**c**) generator torque; (**d**) electric power generation; (**e**) tip speed ratio; (**f**) rotor speed; (**g**) power coefficient; (**h**) thrust coefficient.

In Figure 25a,b the FASTv8 results shown correspond to the modulus of the total rotor aerodynamic loads, applying Equation (118) for Figure 25a and Equation (119) for Figure 25b. The nomenclature used in these equations is the same as that used in FASTv8 and is detailed in Appendix E of [1]. Similarly, the FHYGSYS results shown in Figure 25a correspond to the modulus of the surge, sway, and heave components of the vector $\vec{F}_{j(BODY)}^{WINDTURBINE}(t)$—calculated in Equation (110)—and in Figure 25b to the modulus of the roll, pitch, and yaw components of the same vector.

$$RtAeroF = \sqrt{RtAeroFxh^2 + RtAeroFyh^2 + RtAeroFzh^2} \qquad (118)$$

$$RtAeroM = \sqrt{RtAeroMxh^2 + RtAeroMyh^2 + RtAeroMzh^2} \qquad (119)$$

3.9. Marine Current Turbine Modeling

The marine current turbines have not been able to be compared with the results of another simulation tool; however, the behavior of the marine turbines described in [4,5] has been reproduced as much as possible, given the same dimensions, the same inertial and electrical characteristics, and the same turbine rotation speed curve. The modeling of the marine current turbines has been completed by applying these data as described in Section 2.8.2 with the same code compared and validated with FASTv8 for the wind turbine.

4. Discussion

This work is part of a series of articles that describe the model of a floating hybrid system such as the one shown in Figure 1. In [1], the kinematic and dynamic modeling of the floating system was described, as well as the method to calculate the added mass and the inertial characteristics of the system. This paper concludes the exposition of the mathematical modeling of the floating hybrid system, exposing the forces acting on it and describing in detail the mathematical formulation used. The acting forces refer fundamentally to those originating due to the hydrodynamics, the mooring system, and the wind and marine current turbines.

Force modeling is based on vector calculation and basically consists of obtaining the corresponding force vector, knowing or deducing its application point, and moving the force to the calculation point—in this case, the origin of the mobile coordinate system—thus obtaining an equivalent force and moment at this point.

The calculation is completed by rotating and translating the inertia tensor, usually expressed in the center of mass of each individual body; displacing it to the calculation point; and applying the dynamics equations, as explained in [1].

Figure 2 shows an operating diagram of the mathematical model in which the matrices of the rigid body (M_{RB}), added mass (M_{AM}), and the resultant forces ($\vec{F}_{j(BODY)}^{TOTAL}$) acting on the floating hybrid system can be considered as key elements for its operation. The M_{RB} and M_{AM} matrices represent the mechanical—inertial—characteristics of the floating system and how it will behave when moving through the fluid. The resultant forces and moments that act on the floating system determine the direction, amplitude, and frequency of its movements.

For an adequate understanding of the exposition developed in this work, we recommend reading Part I [1], since many of the explanations made are based on it.

The One-Dimensional theory [66,81] has been used to model wind turbines and marine currents. This modeling technique makes it possible to reproduce the behavior of a turbine in which the operation is known. In this way, it is possible to carry out simulations of how the floating system will behave, but on which it will not be possible to modify any operating pattern that has not been previously tested either in a real model or with a simulation tool.

This means that—according to the authors' interpretation—an integrated automatic control system cannot be implemented on a simulation tool that uses the One-Dimensional theory for turbine modeling.

For this reason, within the series of scheduled publications, one will be included in which the integration of Blade Element Momentum (BEM) theory for turbine modeling in FHYGSYS is described. With this technique, results are obtained from the construction and aerodynamic characteristics of the blades, which allows us, for example, to implement a blade pitch control system. Electrical characteristics of the generators are also used to calculate the power generated, which also allows for the development of a generator torque control system. In this way, modifications can be included in the modeling of the turbines that allow for obtaining results with more details of operation such as those described in [31,37,83].

On the other hand, the modeling described in [1] and in this work allows the study of the behavior of the floating hybrid system with different meteorological conditions, different wind, and marine current speeds, adding the action of waves, etc. The comparison of results exposed in Section 3, in Appendix B, and in Appendix E of [1], allows for having a tool that serves to achieve the main objective for which FHYGSYS has been developed: to implement an integrated control system for the stability of the floating hybrid system.

The mathematical model exposed in [1] and in this work requires careful development since an inadequate composition in some part of it leads to the generation of deficient results. For this reason, all the parts that make up the modeling of the floating hybrid system have been thoroughly exposed.

One of the important issues for the modeling of partially or totally submerged systems is the modeling of the added mass since an inadequate modeling gives deficient results in the transient responses of the different magnitudes. For this reason, in Appendix A, an example of calculation of the added mass matrix (M_{AM}) has been included to clarify the processing of this matrix.

With the aim of demonstrating the reliability and consistency of the results in Appendix B, five simulations have been included, under the same conditions established in Section 3, but using different pairs of seeds to generate white Gaussian noise $W(\omega)$ in each case. Observing the results, it is concluded that when using different seeds, different results are obtained, but all are compatible with the objective of simulating the waves acting on the floating hybrid system.

A test has also been included in Appendix B, under the same conditions as in Section 3, but lasting one hour. This test allows us to evaluate the stability over time of the simulations carried out with FHYGSYS, compared with the results obtained with FASTv8. The conclusion obtained from the test is that FHYGSYS offers temporary stability in the results, demonstrating the reliability of the mathematical model of the floating hybrid system.

In addition to the upcoming post explaining the integration of BEM in FHYGSYS, future work will focus on the study of integrated floating platform stability systems. It is also intended to develop variants of the floating hybrid system with different sizes of turbines, different aerodynamic profiles, etc.

Also included in this series of articles will be one dedicated to the control requirements of the floating system, where cooperative control techniques among all the turbines will be exposed following the hypotheses explained in [1]. For example, making the marine turbines work in power generation mode or in actuator mode to contribute to the stability of the floating hybrid system.

Another of the future publications of the series of articles will be focused on how to translate the exposed mathematical model into computer language, describing the architecture of FHYGSYS as well as the computer resolution of the key points of the code.

Once this first series of articles is finished, we also intend to carry out studies focused on specific aspects of the floating hybrid system, such as the mooring system or certain aspects of the hydrodynamics of the floating system. We also intend to adapt FHYGSYS to other concepts such as the OC4 semi-submersible wind turbine [84].

Abbreviations

Acronym list

ANSYS	Swanson Analysis Systems
ASHES	Aero-servo-hydro-elastic simulation
BEM	Blade Element Momentum Theory
CFD	Computational Fluid Dynamics
DNV	Det Norske Veritas (The Norwegian Veritas)
DTU	Technical University of Denmark
EMEC	European Marine Energy Center
FAST	Fatigue, Aerodynamics, Structures, and Turbulence
FHS	Floating Hybrid Systems
FHYGSYS	Floating Hybrid Generator Systems Simulator
GPL	General Public License
HAWC2	Horizontal Axis Wind Turbine Simulation Code 2nd Generation
JONSWAP	Joint North Sea Wave Project
LES	Large Eddy Simulation Method
MCT	Marine Current Turbines
OC3	Offshore Code Comparison Collaboration
RANS	Reynolds-Averaged Navier–Stokes method
SWL	Still Water Level
TTS	Tidal Turbine Simulation
WAMIT	Wave Analysis Massachusetts Institute of Technology
WAsP	Wind Atlas Analysis and Application Program
WEC	Wave Energy Converter
WRP	WAMIT Reference Point
WT	Wind Turbine
WTS	Wind Turbine Simulation

Symbol list

$a(t,x,y,z)$	acceleration of the water particle at a point of coordinates x, y, and z of the inertial coordinate system
$a_{x(INERTIAL)}(h,t)$	x component of the acceleration $a(t,x,y,z)$ at depths h
$a_{y(INERTIAL)}(h,t)$	y component of the acceleration $a(t,x,y,z)$ at depths h
$\vec{a}_{x,y(INERTIAL)}(h,t)$	x and y components of the acceleration $a(t,x,y,z)$ at depths h
a,b,c	shape parameters to define an ellipsoid
$AddFji$	additional preload, stiffness, and damping forces (i = surge, sway, and heave)
$AddMji$	additional preload, stiffness, and damping moments (i = roll, pitch, and yaw)

$AddYS$	additional yaw spring stiffness
$axif$	axial induction factor of the wind turbine (or marine current turbine)
$anif(t)$	angular induction factor of the wind turbine (or marine current turbine)
$A_{Turbine}$	area of the wind turbine (or marine current turbine)
$\vec{av}_{j(BODY)}$	acceleration vector of six degrees of freedom expressed in the mobile coordinate system
$\alpha_0, \beta_0, \gamma_0$	parameters which depend on the values of the semi-axes of the ellipsoid
α	power law exponent
β	yaw angle that represents the direction of the waves
C_B	cable-seabed friction coefficient
C_D	aerodynamic drag coefficient
$C_D(h)$	drag coefficient of the tower or the floating platform at the p_{VDi} points for the calculation of the viscous drag forces
C_L	aerodynamic lift coefficient
CoB	center of buoyancy of the floating hybrid system
$CoB_{(BODY)}(t)$	center of buoyancy of the floating hybrid system expressed in the mobile coordinate system
CoM	center of mass of the floating hybrid system
$CoM_{(BODY)}(t)$	center of mass of the floating hybrid system expressed in the mobile coordinate system
$CoM_{MCTurbine}$	center of mass of the marine current turbine
$CoM_{WTurbine}$	center of mass of the wind turbine
$CoM_{WTurbine(BODY)}$	center of mass of the wind turbine expressed in the mobile coordinate system
C_P	power coefficient of the wind turbine (or marine current turbine)
$\vec{cross}_{FAi(INTER)}(t)$	cross product of the position vectors $\vec{p}_{FAi(INTER)(t=0)}$ and $\vec{p}_{FAi(INTER)(t>0)}(t)$
$C_T(t)$	thrust coefficient of the wind turbine (or marine current turbine)
$\vec{cv}1$ and $\vec{cv}2$	vectors needed to obtain the Coriolis–centripetal matrix (M_{CC})
$D(h)$	diameter of the tower or the floating platform at the p_{VDi} points for the calculation of the viscous drag forces
D_C	mooring line diameter
$d\vec{F}_{(BODY)}^{VISCOUS}(h,t)$	differential of the vector of viscous drag forces expressed in the mobile coordinate system
$d\vec{F}_{x(INERTIAL)}^{VISCOUS}(h,t)$	x component of $d\vec{F}_{(BODY)}^{VISCOUS}(h,t)$ vector
$d\vec{F}_{y(INERTIAL)}^{VISCOUS}(h,t)$	y component of $d\vec{F}_{(BODY)}^{VISCOUS}(h,t)$ vector
$d\vec{F}_{x,y(BODY)}^{WAVES}(h,t)$	x and y components of the differential of the vector of wave forces expressed in the mobile coordinate system
$d\vec{F}_{x,y(INERTIAL)}^{WAVES}(h,t)$	x and y components of the differential of the vector of wave forces expressed in the inertial coordinate system
D_{Hub}	wind turbine hub diameter
$d\vec{M}_{(BODY)}^{VISCOUS}(h,t)$	differential of the moment vector of viscous drag forces expressed in the mobile coordinate system
$d\vec{M}_{x,y(BODY)}^{WAVES}(h,t)$	x and y components of the differential of the moment vector of wave forces expressed in the mobile coordinate system
d_{WATER}	water depth
δ	direction of the wind velocity vector
Δt	time increment used for the simulations
EA	equivalent mooring line extensional stiffness
ε	direction of the sub-surface current velocity vector
f	wave frequency related to the angular speed by $\omega = 2 \cdot \pi \cdot f$
$\vec{F}_{(BODY)}^{ADDITIONAL\ DAMPING}(t)$	vector of additional damping forces expressed in the mobile coordinate system
$\vec{F}_{(INERTIAL)}^{ADDITIONAL\ DAMPING}(t)$	vector of additional damping forces expressed in the inertial coordinate system

$\overset{\rightarrow CORIOLIS}{F_{(BODY)}}(t)$	vector of Coriolis–centripetal forces expressed in the mobile coordinate system
$\overset{\rightarrow GRAVITY}{F_{(BODY)}}(t)$	vector of gravitational forces expressed in the mobile coordinate system
$\overset{\rightarrow GRAVITY}{F_{(INERTIAL)}}$	vector of gravitational forces expressed in the inertial coordinate system
$\overset{\rightarrow HYDROSTATICS}{F_{(BODY)}}(t)$	vector of hydrostatic forces expressed in the mobile coordinate system
$\overset{\rightarrow HYDROSTATICS}{F_{(INERTIAL)}}(t)$	vector of hydrostatic forces expressed in the inertial coordinate system
$F_{Line\ i}$	force vector of mooring line i (i = line 1, 2, or 3) expressed in the anchor coordinate system
$\overset{\rightarrow LINE\ i}{F_{(ANCHOR)}}(t)$	force vector of mooring line i (i = line 1, 2, or 3) expressed in the anchor coordinate system
$\overset{\rightarrow LINE\ i}{F_{(BODY)}}(t)$	force vector of mooring line i (i = line 1, 2, or 3) expressed in the mobile coordinate system
$\overset{\rightarrow LINE\ i}{F_{(INERTIAL)}}(t)$	force vector of mooring line i (i = line 1, 2, or 3) expressed in the inertial coordinate system
$\overset{\rightarrow VISCOUS}{F_{(BODY)}}(t)$	force and moment vector due to the viscous drag expressed in the mobile coordinate system without neglecting the values of heave and yaw
$\overset{\rightarrow VISCOUS}{F_{(INERTIAL)}}(t)$	force and moment vector due to the viscous drag expressed in the inertial coordinate system without neglecting the values of heave and yaw
$\overset{\rightarrow VISCOUS\ DRAG}{F_{(INERTIAL)}}(t)$	force and moment vector due to the viscous drag expressed in the inertial coordinate system
$\overset{\rightarrow\ WAVES}{F_{x,y(BODY)}}(t)$	force and moment vector due to the waves expressed in the mobile coordinate system without heave component
$\overset{\rightarrow WAVES}{F_{z(BODY)}}(t)$	heave component of force and moment vector due to the waves expressed in the mobile coordinate system
$\overset{\rightarrow WAVES}{F_{z(INERTIAL)}}(t)$	heave component of force and moment vector due to the waves expressed in the inertial coordinate system
$\overset{\rightarrow ADDED\ MASS}{F_{j(BODY)}}$	force and moment vector due to the added mass expressed in the mobile coordinate system
$\overset{\rightarrow ADDITIONAL\ DAMPING}{F_{j(BODY)}}$	force and moment vector due to the additional damping and stiffness expressed in the mobile coordinate system
$\overset{\rightarrow CORIOLIS}{F_{j(BODY)}}$	force and moment vector due to the Coriolis–centripetal effects expressed in the mobile coordinate system
$\overset{\rightarrow CURRENT\ TURBINE}{F_{j(BODY)}}$	force and moment vector due to marine current turbines thrust expressed in the mobile coordinate system
$\overset{\rightarrow GRAVITY}{F_{j(BODY)}}$	force and moment vector due to gravitational field expressed in the mobile coordinate system
$\overset{\rightarrow HYDRODYNAMICS}{F_{j(BODY)}}$	force and moment vector due to hydrodynamics expressed in the mobile coordinate system
$\overset{\rightarrow HYDROSTATICS}{F_{j(BODY)}}$	force and moment vector due to hydrostatics expressed in the mobile coordinate system
$\overset{\rightarrow LINE\ 1}{F_{j(BODY)}}, \overset{\rightarrow LINE\ 2}{F_{j(BODY)}}, \overset{\rightarrow LINE\ 3}{F_{j(BODY)}}$	force and moment vector due to the mooring lines 1, 2, and 3, expressed in the mobile coordinate system
$\overset{\rightarrow LINE\ i}{F_{j(BODY)}}$	force and moment vector due to the mooring line I (i = line 1, 2, or 3) expressed in the mobile coordinate system
$\overset{\rightarrow MOORING\ SYSTEM}{F_{j(BODY)}}$	force and moment vector due to the mooring system expressed in the mobile coordinate system
$\overset{\rightarrow NEAR-SURFACE\ CURRENT}{F_{j(BODY)}}$	virtual force and moment vector due to the action of near-surface current on the floating platform expressed in the mobile coordinate system

$\overset{\rightarrow SUB-SURFACE\ CURRENT}{F_{j(BODY)}}$	virtual force and moment vector due to the action of sub-surface current on the floating platform expressed in the mobile coordinate system
$\overset{\rightarrow TOTAL}{F_{j(BODY)}}$	resultant force and moment vector of the floating hybrid system expressed in the mobile coordinate system
$\overset{\rightarrow VISCOUS\ DRAG}{F_{j(BODY)}}$	force and moment vector due to the viscous drag expressed in the mobile coordinate system
$\overset{\rightarrow WAVES}{F_{j(BODY)}}$	force and moment vector due to the waves expressed in the mobile coordinate system
$\overset{\rightarrow WIND\ TOWER}{F_{j(BODY)}}$	virtual force and moment vector due to the action of wind on the tower expressed in the mobile coordinate system
$\overset{\rightarrow WIND\ TURBINE}{F_{j(BODY)}}$	force and moment vector due to wind turbine thrust expressed in the mobile coordinate system
$F_{MCThrust}$	vector of marine current turbine force
$F_{WThrust}$	vector of wind turbine force
$\vec{F}_{WThrust(BODY)}(t)$	vector of wind turbine force expressed in the mobile coordinate system
g	gravity acceleration
$gearR$	wind turbine—or marine current turbine—gearbox ratio
$genE$	wind turbine—or marine current turbine—electrical generator efficiency
$\gamma(T_p, H_s)$	peak shape parameter in JONSWAP spectrum
h	height if $h > 0$ or depth if $h \leq 0$, z coordinate of a point
H_{Ai}	horizontal component of force vector of mooring line i (i = line 1, 2, or 3) applied on its anchor
$HdrStcFji$	hydrostatic forces (i = surge, sway, and heave)
$HdrStcMji$	hydrostatic moments (i = roll, pitch, and yaw)
H_{Fi}	horizontal component of force vector of mooring line i (i = line 1, 2, or 3) applied on its fairlead
$h_{free\ shadow}$	height of the tower of the floating system free from the shadow of the wind turbine
h_{Hub}	wind turbine hub height, or marine current turbine depth
H_s	significant wave height
$h_{submerged}$	depth of the submerged part of the floating platform
$HydroFji$	total integrated hydrodynamic forces from both potential flow and strip theory (i = surge, sway, and heave)
$HydroMji$	total integrated hydrodynamic moments from both potential flow and strip theory (i = roll, pitch, and yaw)
I_{xx}, I_{yy}, I_{zz}	moments of inertia of the floating hybrid system
I_{xy}, I_{yz}, I_{zx}	products of inertia of the floating hybrid system
$I_{xx(SUM)}, I_{yy(SUM)}, I_{zz(SUM)}$	moments of inertia of the submerged volume of the floating hybrid system
$I_{xy(SUM)}, I_{yz(SUM)}, I_{zx(SUM)}$	products of inertia of the submerged volume of the floating hybrid system
j	imaginary unit of value $\sqrt{-1}$
$k(\omega)$	wave number in a finite depth
L	unstretched mooring line length
L_{Blade}	wind turbine—or marine current turbine—blade length
L_{Bi}	unstretched portion of the mooring line resting on the seabed
λ_{wave}	wavelength
$\overset{\rightarrow ADDITIONAL\ DAMPING}{M_{(INERTIAL)}}(t)$	moment vector of additional damping forces expressed in the inertial coordinate system
$\overset{\rightarrow ADDDAMP\ \&\ STIFFNESS}{M_{(BODY)}}(t)$	moment vector of additional damping and stiffness forces expressed in the mobile coordinate system
$\overset{\rightarrow CORIOLIS}{M_{(BODY)}}(t)$	moment vector of Coriolis–centripetal forces expressed in the mobile coordinate system
$\overset{\rightarrow GRAVITY}{M_{(BODY)}}(t)$	moment vector of gravitational forces expressed in the mobile coordinate system

$\overrightarrow{M}_{(BODY)}^{HYDROSTATICS}(t)$	moment vector of hydrostatic forces expressed in the mobile coordinate system
$\overrightarrow{M}_{(BODY)}^{LINE\ i}(t)$	moment vector of mooring line i (i = line 1, 2, or 3) expressed in the mobile coordinate system
$\overrightarrow{M}_{(INERTIAL)}^{STIFFNESS}(t)$	moment vector of stiffness forces expressed in the inertial coordinate system
$\overrightarrow{M}_{MCThrust}$	moment vector of marine current turbine force
$\overrightarrow{M}_{MCTorque}$	vector of marine current turbine moment
$\overrightarrow{M}_{WThrust(BODY)}(t)$	moment vector of wind turbine force expressed in the mobile coordinate system
$\overrightarrow{M}_{WTorque(BODY)}(t)$	vector of wind turbine moment expressed in the mobile coordinate system
M_{AM}	added mass matrix
M_{CC}	Coriolis–centripetal matrix
m_{FS}	total mass of the floating hybrid system
$M_{BODY}^{INERTIAL}$	transformation matrix that allows changing between the inertial coordinate system and the mobile coordinate system
$M_{HT\ BODY}^{INERTIAL}$	homogeneous transformation matrix that allows for changing between the inertial coordinate system and the mobile coordinate system
$M_{HTi\ ANCHOR}^{INERTIAL}$	homogeneous transformation matrix that allows for changing between the inertial coordinate system and the anchor coordinate system of the mooring line i (i = line 1, 2, or 3)
m_{Line}	equivalent mooring line mass density
M_{RB}	rigid body matrix
$M_{RB(11)}$	top left 3×3 submatrix of M_{RB}
$M_{RB(12)}$	top right 3×3 submatrix of M_{RB}
$M_{RB(21)}$	bottom left 3×3 submatrix of M_{RB}
$M_{RB(22)}$	bottom right 3×3 submatrix of M_{RB}
$m_{SUM}(t)$	mass of the submerged volume of the floating hybrid system
ω	angular speed related to the wave frequency by $\omega = 2 \cdot \pi \cdot f$
Ω	module of the angular speed of the wind turbine—or marine current turbine—rotor
p_{A1}, p_{A2}, p_{A3}	points of the anchors fixed on the seabed in the initial position
$p_{Ai(INERTIAL)}$	Points of the anchors of mooring lines 1, 2, and 3 expressed in the inertial coordinate system
$P_{ELE}(t)$	electrical power generated by the turbine
p_{F1}, p_{F2}, p_{F3}	points of the fairleads attached to the floating platform in the initial position
p_{Fi}	points of the fairlead of mooring lines 1, 2, and 3
$p_{Fi(ANCHOR)}(t)$	p_{Fi} points expressed in the anchor coordinate system
$p_{Fi(BODY)}$	p_{Fi} points expressed in the mobile coordinate system
$p_{Fi(INERTIAL)}$	p_{Fi} points expressed in the inertial coordinate system
$\overrightarrow{p}_{FAi(INTER)}$	position vector of the fairlead of mooring lines 1, 2, and 3 expressed in the intermediate anchor coordinate system
$P_{MEC}(t)$	mechanical power generated by the turbine
$\overrightarrow{p}_{point(INERTIAL)}(t)$	point—or position vector—expressed in the inertial coordinate system
p_{VDi}	centers of the circular sections into which the tower and the floating platform are divided for the calculation of the viscous drag forces
$\overrightarrow{p}_{VDi(BODY)}(t)$	p_{VDi} points expressed in the mobile coordinate system
$\overrightarrow{p}_{VDi(INERTIAL)}(t)$	p_{VDi} points expressed in the inertial coordinate system
p_{VDmax}	highest shadow-free p_{VDi} point
p_{VDmin}	deepest shadow-free p_{VDi} point
$p_{VDswl}(t)$	p_{VDi} point at the still water level

$\varphi_{anchori}(t)$	angle between the position vectors $\vec{p}_{FAi(INTER)(t=0)}$ and $\vec{p}_{FAi(INTER)(t>0)}(t)$ of the mooring line i (i = line 1, 2, or 3)
$\varphi_{anchorCSi}(t)$	angle of rotation of the intermediate anchor coordinate system around its corresponding Z axis to obtain the anchor coordinate system of each mooring line i (i = line 1, 2, or 3)
$\varphi_{Line\ 1}, \varphi_{Line\ 2}, \varphi_{Line\ 3}$	yaw angle with respect to inertial X axis of the mooring lines in the initial position
φ_{pitch}	pitch angle of wind turbine—or marine current turbine–blades
$\varphi_{Precone}$	wind turbine—or marine current turbine—precone angle
$\varphi_{ShaftTilt}$	wind turbine—or marine current turbine—shaft tilt angle
$Q(t)$	moment vector module of the turbine
$q_6(t)$	system degree of freedom 6, yaw value of the floating hybrid system at each instant of time
$\dot{q}_1, \dot{q}_2, \dot{q}_3, \dot{q}_4, \dot{q}_5, \dot{q}_6$	vector $\vec{vv}_{i(INERTIAL)}(t)$ components
$Q_{GEN}(t)$	torque produced in the electrical generator
Re	real part of a complex number
$RdtnFji$	radiation forces (i = surge, sway, and heave)
$RdtnMji$	radiation moments (i = roll, pitch, and yaw)
r_{Hub}	wind turbine—or marine current turbine—hub radius
$r_{swl}(t)$	radius of the floating platform at its intersection with the still water level
$RtAeroF$	total rotor aerodynamic forces (thrust)
$RtAeroM$	total rotor aerodynamic moments (torque)
$r_{Turbine}$	wind turbine—or marine current turbine—radius
ρ_{AIR}	density of air
$\rho_{fluid}(h)$	density of the corresponding fluid at the p_{VDi} points for the calculation of the viscous drag forces
$\rho_{SEAWATER}$	density of seawater
$S_{JONSWAP}^{1-Sided}(\omega)$	one-sided power spectral density of the wave elevation per unit time of JONSWAP spectrum
$S_{P-M}^{1-Sided}(\omega)$	one-sided power spectral density of the wave elevation per unit time of Pierson–Moskowitz spectrum
$S_{JONSWAP}^{2-Sided}(\omega)$	two-sided power spectral density of the wave elevation per unit time of JONSWAP spectrum
$\sigma(\omega)$	scaling factor in the JONSWAP spectrum
t	time or instant of time
$T(t)$	thrust vector module of the turbine
T_{AM}	kinetic energy of the added mass
T_s	wave peak period
$TSR(t)$	tip speed ratio of the turbine
u, v, w, p, q, r	vector $\vec{vv}_{i(BODY)}(t)$ components
$U_1(\omega)$	first set of random numbers—generated from a certain seed—for each of the ω values
$U_2(\omega)$	second set of random numbers—generated from a certain seed—for each of the ω values
$V_0(t)$	wind—or marine current—speed far upstream of the rotor
$V_{1-2}(t)$	magnitude of the effective wind—or marine current—velocity vector on the wind turbine (or marine current turbine)
V_{Ai}	vertical component of force vector of mooring line i (i = line 1, 2, or 3) applied on its anchor
V_{Fi}	vertical component of force vector of mooring line i (i = line 1, 2, or 3) applied on its fairlead
$ViscDFji$	viscous drag forces (i = surge, sway, and heave)
$ViscDMji$	viscous drag moments (i = roll, pitch, and yaw)
$V_{NSCUR}(h)$	magnitude of the near-surface current velocity vector at a certain depth

$V_{SSCUR}(h)$	magnitude of the sub-surface current velocity vector at a certain depth
V_{SWL}	magnitude of the sub-surface current velocity vector at the reference depth
V_{W-REF}	magnitude—or mean wind speed—of the wind velocity vector at the reference height
$V_{WIND}(h)$	magnitude of the wind velocity vector at a certain height
$\vec{v}_{EFF-MCThrust(BODY)}(h,t)$	effective marine current velocity vector on the marine current turbine expressed in the mobile coordinate system
$\vec{v}_{EFF-NSCURR(INERTIAL)}(h,t)$	effective near-surface current velocity vector expressed in the inertial coordinate system
$\vec{v}_{EFF-SSCURR(BODY)}(h,t)$	effective sub-surface current velocity vector expressed in the mobile coordinate system
$\vec{v}_{EFF-SSCURR(INERTIAL)}(h,t)$	effective sub-surface current velocity vector expressed in the inertial coordinate system
$\vec{v}_{EFF-WIND(BODY)}(h,t)$	effective wind velocity vector expressed in the mobile coordinate system
$\vec{v}_{EFF-WIND(INERTIAL)}(h,t)$	effective wind velocity vector expressed in the inertial coordinate system
$\vec{v}_{EFF-WThrust(BODY)}(t)$	effective wind velocity vector on the wind turbine expressed in the mobile coordinate system
$\vec{v}_{NSCUR(INERTIAL)}(h)$	near-surface current velocity vector of the vector field rotated by the corresponding angle δ expressed in the inertial coordinate system
$\vec{v}_{point(INERTIAL)}(t)$	velocity vector of the floating hybrid system at a given point expressed in the inertial coordinate system
$\vec{v}_{SSCUR(INERTIAL)}(h)$	sub-surface current velocity vector of the vector field rotated by the corresponding angle ε expressed in the inertial coordinate system
$\vec{v}_{VDi(INERTIAL)}(h,t)$	velocity vector of the floating hybrid system at the p_{VDi} points expressed in the inertial coordinate system
$\vec{v}_{VDRi(INERTIAL)}(h,t)$	relative velocity vector between the speed of the fluids and that of the floating hybrid system at the p_{VDi} points expressed in the inertial coordinate system
$\vec{v}_{VDRix(INERTIAL)}(h,t)$	x component of $\vec{v}_{VDRi(INERTIAL)}(h,t)$ velocity vector
$\vec{v}_{VDRiy(INERTIAL)}(h,t)$	y component of $\vec{v}_{VDRi(INERTIAL)}(h,t)$ velocity vector
$\left|\vec{v}_{VDRix-y(INERTIAL)}(h,t)\right|$	magnitude of the relative velocity vector $\vec{v}_{VDRi(INERTIAL)}(h,t)$ neglecting the z component
$\vec{v}_{MCThrust(BODY)}$	unit vector of marine current turbine force expressed in the mobile coordinate system
$\vec{v}_{MCTorque(BODY)}$	unit vector of marine current turbine moment expressed in the mobile coordinate system
$\vec{v}_{WIND(INERTIAL)}(h)$	wind velocity vector of the vector field rotated by the corresponding angle δ expressed in the inertial coordinate system
$\vec{v}_{WThrust(BODY)}$	unit vector of wind turbine force expressed in the mobile coordinate system
$\vec{v}_{WTorque(BODY)}$	unit vector of wind turbine moment expressed in the mobile coordinate system
$\vec{vv}_{i(BODY)}$	velocity vector of six degrees of freedom of the floating hybrid system expressed in the mobile coordinate system
$\vec{vv}_{i(INERTIAL)}$	velocity vector of six degrees of freedom of the floating hybrid system expressed in the inertial coordinate system
$W(\omega)$	white Gaussian noise time-series process
$WavesFji$	wave-excitation forces from diffraction (i = surge, sway, and heave)
$WavesMji$	wave-excitation moments from diffraction (i = roll, pitch, and yaw)
w_L	apparent weight of the mooring line in fluid per unit length
x	x component of each element of the mesh that represents the sea
$X_A, Y_A, Z_A, K_A, M_A, N_A$	vector $-\vec{F}_{j(BODY)}^{ADDEDMASS}$ components
x_{Fi}	x component of $p_{Fi(ANCHOR)}(t)$

$X_{\dot{u}}, Y_{\dot{v}}, Z_{\dot{w}}, K_{\dot{p}}, M_{\dot{q}}, N_{\dot{r}}$	values of the main diagonal of the added mass matrix
y	y component of each element of the mesh that represents the sea
y_{Fi}	y component of $p_{Fi(ANCHOR)}(t)$
z	z component of the vector $p_{VDi(INERTIAL)}$ to calculate the acceleration of the water particles
z_{Fi}	z component of $p_{Fi(ANCHOR)}(t)$
z_{REF}	reference height of the wind velocity vector
$z_{NSCUR}(t)$	depth to calculate the magnitude of the near-surface current velocity vector
$z_{SSCUR}(t)$	depth to calculate the magnitude of the sub-surface current velocity vector
$z_{WIND}(t)$	height to calculate the magnitude of the wind velocity vector
$\zeta_{swl}(t)$	wave elevation at the intersection of the floating platform with the still water level
$\zeta_{mesh}(t)$	wave elevation of each element of the mesh that represents the sea
$\zeta(t, x, y)$	wave elevation of a grid element—of the mesh that represents the sea—with x and y coordinates

Appendix A

This appendix presents, as an example, the calculation of the values of the added mass matrix (M_{AM}) from the inertial characteristics of the submerged part of the floating hybrid system—shown in Figure 1—that appear in Table 3. These characteristics are the mass ($m_{SUM}(t)$), the center of buoyancy ($CoB(t)$), and the inertia tensor ($M_{IT(SUM)(FS)}(t)$) of the submerged volume of the floating hybrid system for $t = 0$.

Following the indications of Section 2.3.3 of [1], firstly, the parameters that define the ellipsoid with which the submerged volume of the floating system resembles are calculated with Equations (A1) and (A2).

$$a = b = \frac{D_{max}}{2} = \frac{9.4}{2} = 4.7 \text{ m} \tag{A1}$$

$$c = \frac{h_{submerged}(t)}{2} = \frac{120}{2} = 60 \text{ m} \tag{A2}$$

The value of $h_{submerged}$ appears in Table 7, while D_{max} is the diameter of the floating platform below the conical region shown in Table 8. Both data are taken from [2]. This calculation is performed at each instant of time; for instants $t > 0$, $h_{submerged}$ varies and the calculation is performed with this updated value, while the value of D_{max} is considered constant given the mostly spar shape of the submerged volume of the floating hybrid system.

Next, Equations (23)–(31) of [1] are applied to obtain the values of the main diagonal of the added mass matrix (M_{AM}).

$$e = \sqrt{1 - \frac{a^2}{c^2}} = 0.996927 \tag{A3}$$

$$\alpha_0 = \beta_0 = \frac{1}{e^2} - \frac{1 - e^2}{2 \cdot e^3} \cdot \log \frac{1 + e}{1 - e} = 0.986119 \tag{A4}$$

$$\gamma_0 = \frac{2 \cdot (1 - e^2)}{e^3} \cdot \left(\frac{1}{2} \cdot \log \frac{1 + e}{1 - e} - e \right) = 0.0277629 \tag{A5}$$

In Equations (A4) and (A5), log represents the natural logarithm of the corresponding values.

$$X_{\dot{u}} = -\frac{\alpha_0}{2 - \alpha_0} \cdot m_{SUM}(t) = -0.972617 \cdot 8,302,931 = -8,075,574 \text{ kg} \tag{A6}$$

$$Y_{\dot{v}} = -\frac{\beta_0}{2-\beta_0} \cdot m_{SUM}(t) = -0.972617 \cdot 8,302,931 = -8,075,574 \text{ kg} \tag{A7}$$

$$Z_{\dot{w}} = -\frac{\gamma_0}{2-\gamma_0} \cdot m_{SUM}(t) = -0.0140769 \cdot 8,302,931 = -116,879 \text{ kg} \tag{A8}$$

$$K_{\dot{p}} = -\frac{(b^2-c^2)^2 \cdot (\gamma_0-\beta_0)}{2 \cdot (b^4-c^4) + (b^2+c^2)^2 \cdot (\beta_0-\gamma_0)} \cdot I_{xx(SUM)}(t) = -0.919262 \cdot 410,511 \cdot 10^5 = -377,367 \cdot 10^5 \text{ kg} \cdot \text{m}^2 \tag{A9}$$

$$M_{\dot{q}} = -\frac{(c^2-a^2)^2 \cdot (\alpha_0-\gamma_0)}{2 \cdot (c^4-a^4) + (c^2+a^2)^2 \cdot (\gamma_0-\alpha_0)} \cdot I_{yy(SUM)}(t) = -0.919262 \cdot 410,511 \cdot 10^5 = -377,367 \cdot 10^5 \text{ kg} \cdot \text{m}^2 \tag{A10}$$

$$N_{\dot{r}} = -\frac{(a^2-b^2)^2 \cdot (\beta_0-\alpha_0)}{2 \cdot (a^4-b^4) + (a^2+b^2)^2 \cdot (\alpha_0-\beta_0)} \cdot I_{zz(SUM)}(t) = 0 \text{ kg} \cdot \text{m}^2 \tag{A11}$$

The solution of Equation (A11) is indeterminate, so zero is chosen as the result. Once the values of the main diagonal of the M_{AM} matrix have been calculated, Equation (32) from [1] is applied. In this equation, some elements appear multiplied by the mass of the submerged volume ($m_{SUM}(t)$). As in Equations (A6)–(A8)—Equations (26)–(28) of [1]—the mass of the submerged volume must be multiplied by the coefficients as a function of α_0, β_0, and γ_0. For this reason, Equation (32) of [1] should be interpreted as shown in Equation (A12).

$$M_{AM} = -\begin{bmatrix} X_{\dot{u}} & 0 & 0 & 0 & Y_{\dot{v}} \cdot z_{CoB} & -Z_{\dot{w}} \cdot y_{CoB} \\ 0 & Y_{\dot{v}} & 0 & -X_{\dot{u}} \cdot z_{CoB} & 0 & Z_{\dot{w}} \cdot x_{CoB} \\ 0 & 0 & Z_{\dot{w}} & X_{\dot{u}} \cdot y_{CoB} & -Y_{\dot{v}} \cdot x_{CoB} & 0 \\ 0 & -Y_{\dot{v}} \cdot z_{CoB} & Z_{\dot{w}} \cdot y_{CoB} & K_{\dot{p}} & -I_{xy(SUM)} & -I_{zx(SUM)} \\ X_{\dot{u}} \cdot z_{CoB} & 0 & -Z_{\dot{w}} \cdot x_{CoB} & -I_{xy(SUM)} & M_{\dot{q}} & -I_{yz(SUM)} \\ -X_{\dot{u}} \cdot y_{CoB} & Y_{\dot{v}} \cdot x_{CoB} & 0 & -I_{zx(SUM)} & -I_{yz(SUM)} & N_{\dot{r}} \end{bmatrix} \tag{A12}$$

Finally, applying Equation (A12) to the considered example, the fully processed added mass matrix (M_{AM}) is obtained, representing the results in Equation (A13).

$$M_{AM} = -\begin{bmatrix} -8,075,574 & 0 & 0 & 0 & 498,180 \cdot 10^3 & 0 \\ 0 & -8,075,574 & 0 & -498,180 \cdot 10^3 & 0 & -42.8265 \\ 0 & 0 & -116,879 & 0 & 2959.03 & 0 \\ 0 & -498,180 \cdot 10^3 & 0 & -377,367 \cdot 10^5 & 0 & 60,847.1 \\ 498,180 \cdot 10^3 & 0 & 42.8265 & 0 & -377,233 \cdot 10^5 & 0 \\ 0 & -2959.03 & 0 & 60,847.1 & 0 & 0 \end{bmatrix} \tag{A13}$$

Appendix B

*Appendix B.1. Five Tests with Different Seeds to Generate White Gaussian Noise*

For the sake of brevity, in the five tests, only the magnitudes that have been considered most relevant are shown. Table A1 contains the random seeds used in each of the corresponding parameters of the five tests carried out, compared with those of the test in Section 3. The weather conditions are the same as those of the Section 3 test.
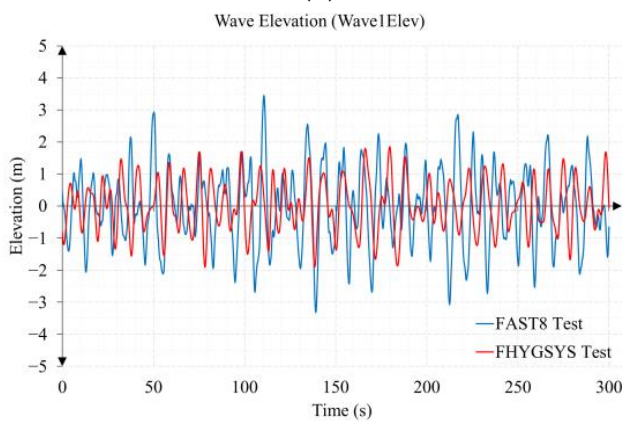
Table A1. Seeds used in Matlab® in each test.

Test	Parameter	Seed
Section 3	$U_1(\omega)$	1,011,121,314
	$U_2(\omega)$	123,456,789
First	$U_1(\omega)$	2,505,145,020
	$U_2(\omega)$	1,130,143,962
Second	$U_1(\omega)$	740,180,996
	$U_2(\omega)$	2,144,412,254
Third	$U_1(\omega)$	19,329,888
	$U_2(\omega)$	3,200,590,489
Fourth	$U_1(\omega)$	645,186,545
	$U_2(\omega)$	2,201,119,503
Fifth	$U_1(\omega)$	3,938,040,421
	$U_2(\omega)$	2,229,424,326
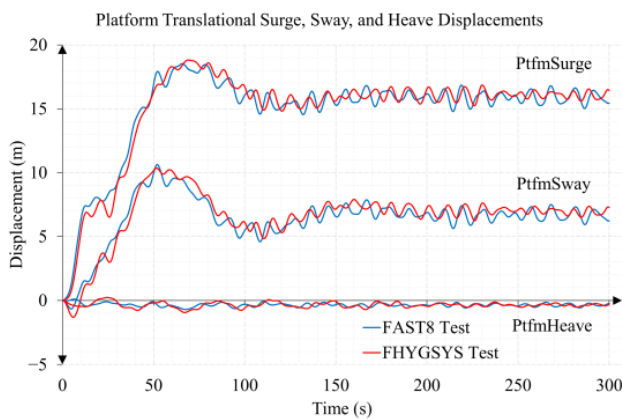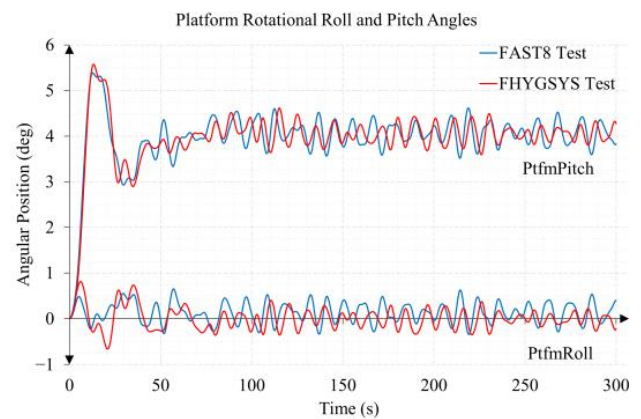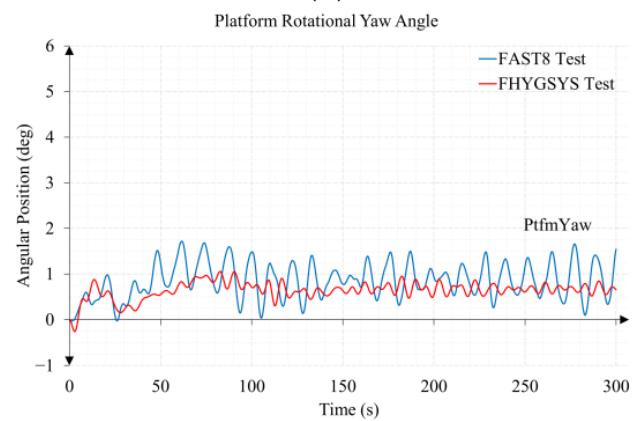
Figure A1. First test results: (**a**) surge, sway, and heave displacements; (**b**) roll and pitch angles; (**c**) wave elevation; (**d**) yaw angle.
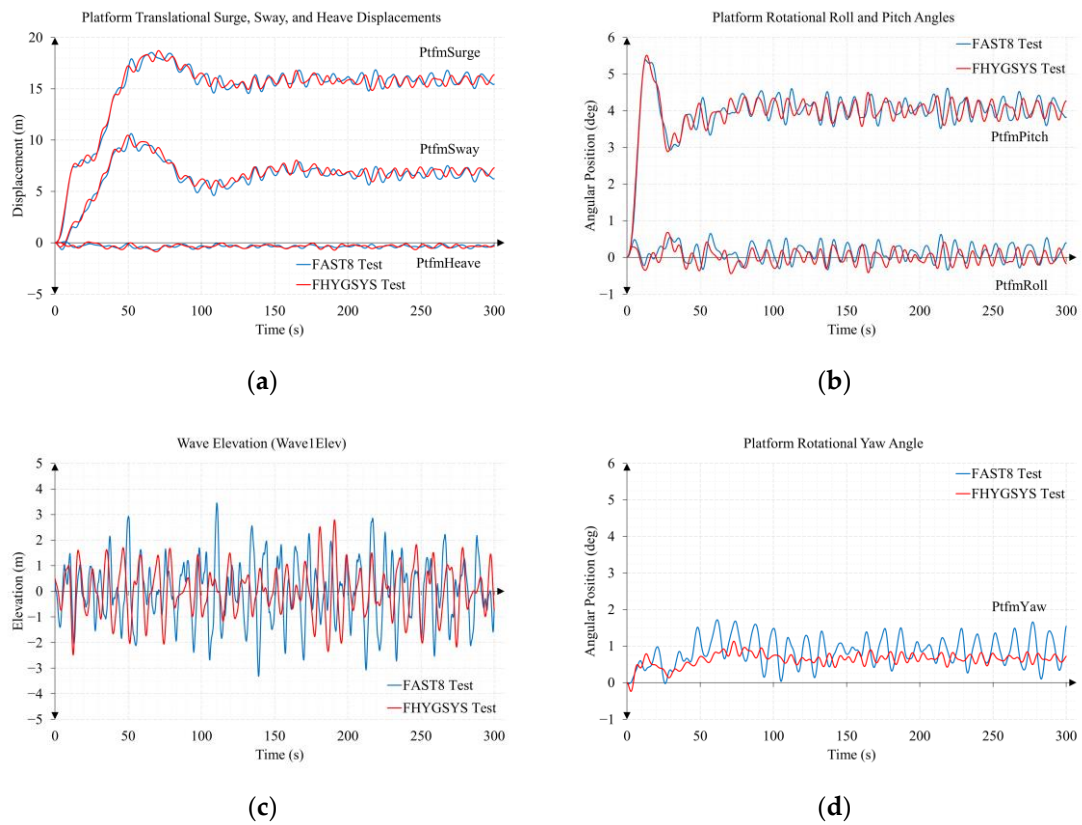
Figure A2. Second test results: (**a**) surge, sway, and heave displacements; (**b**) roll and pitch angles; (**c**) wave elevation; (**d**) yaw angle.
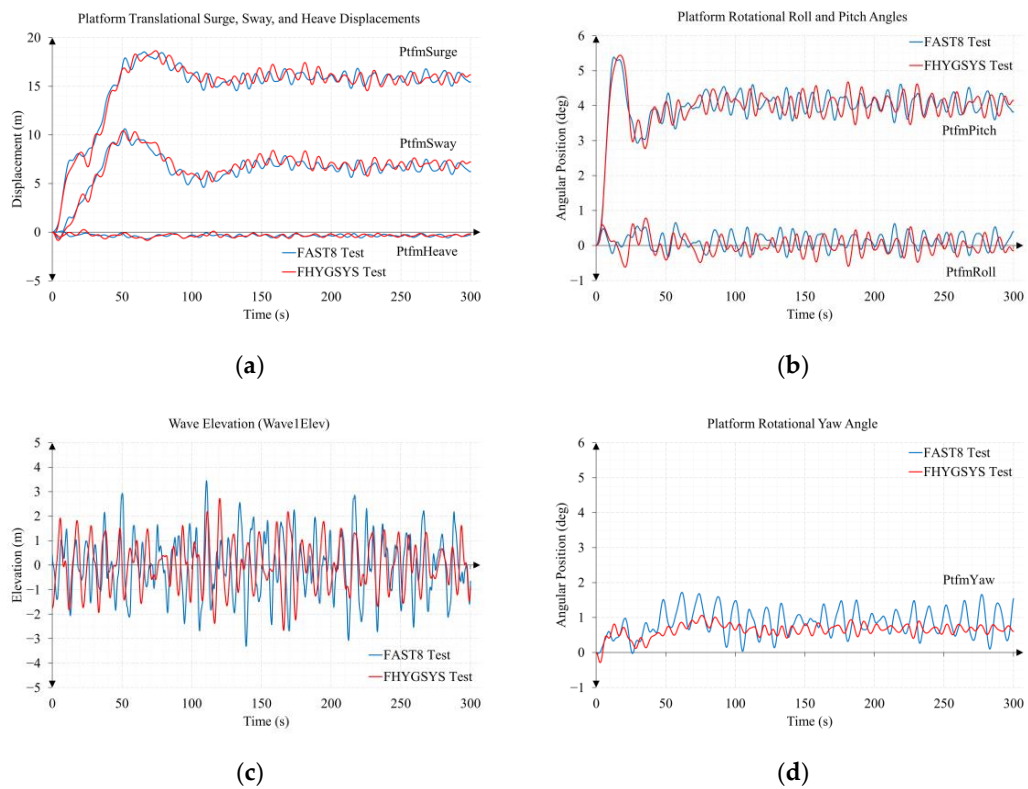
Figure A3. Third test results: (**a**) surge, sway, and heave displacements; (**b**) roll and pitch angles; (**c**) wave elevation; (**d**) yaw angle.
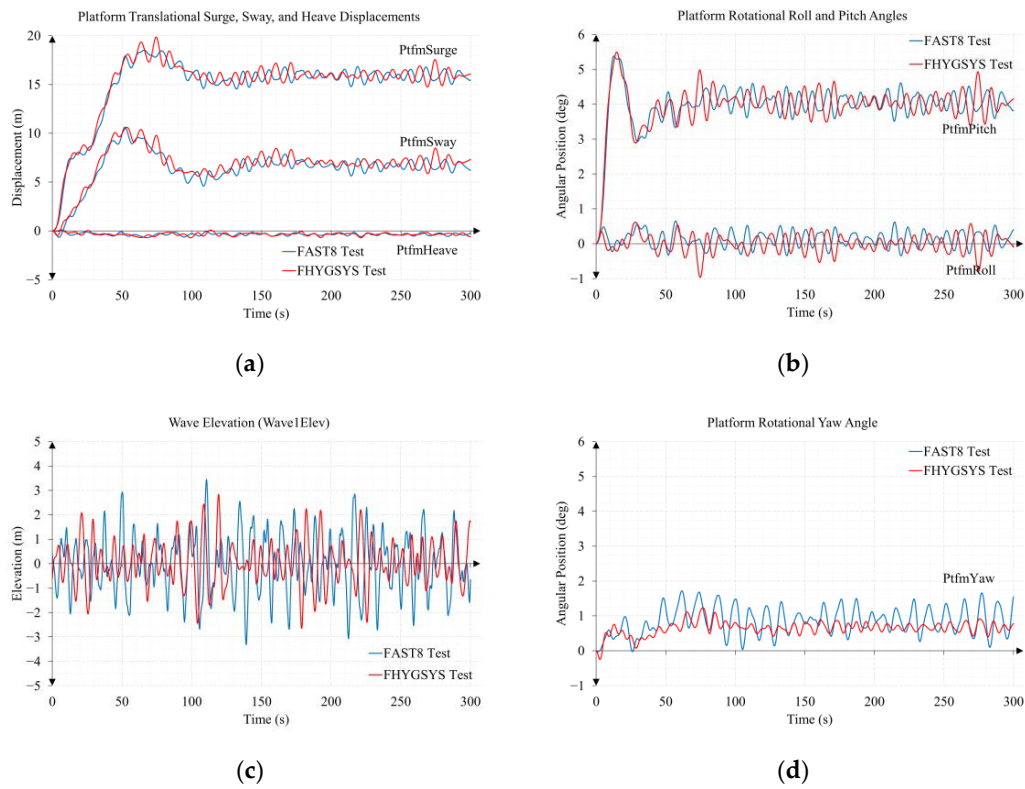
Figure A4. Fourth test results: (**a**) surge, sway, and heave displacements; (**b**) roll and pitch angles; (**c**) wave elevation; (**d**) yaw angle.
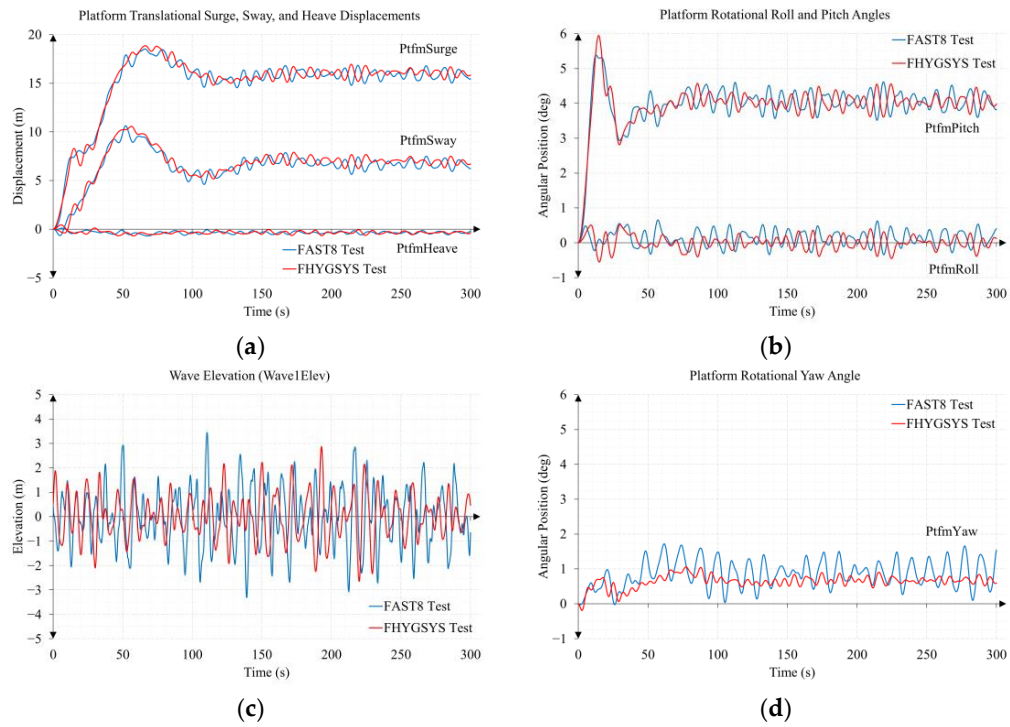
Figure A5. Fifth test results: (**a**) surge, sway, and heave displacements; (**b**) roll and pitch angles; (**c**) wave elevation; (**d**) yaw angle.

Appendix B.2. Complete Test of One Hour Duration

This section shows the results of a complete test such as the one carried out in Section 3 but lasting one hour. The weather conditions are the same as those of the Section 3 test.
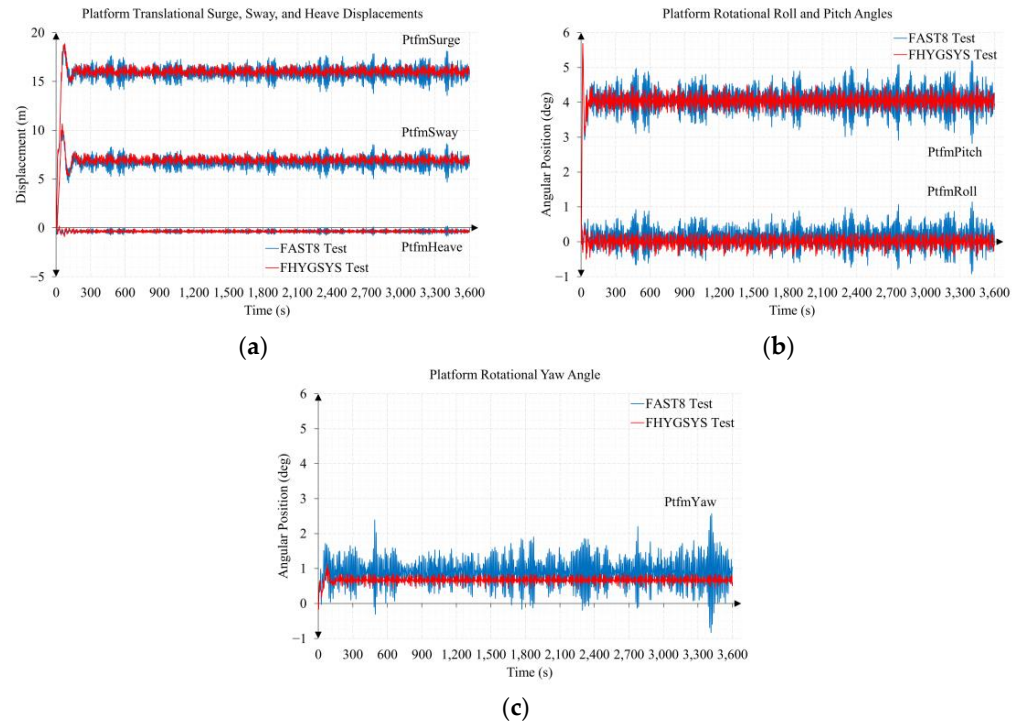
Figure A6. Linear and angular degrees of freedom (one hour test): (**a**) linear degrees of freedom; (**b**) roll and pitch angles; (**c**) yaw angle.
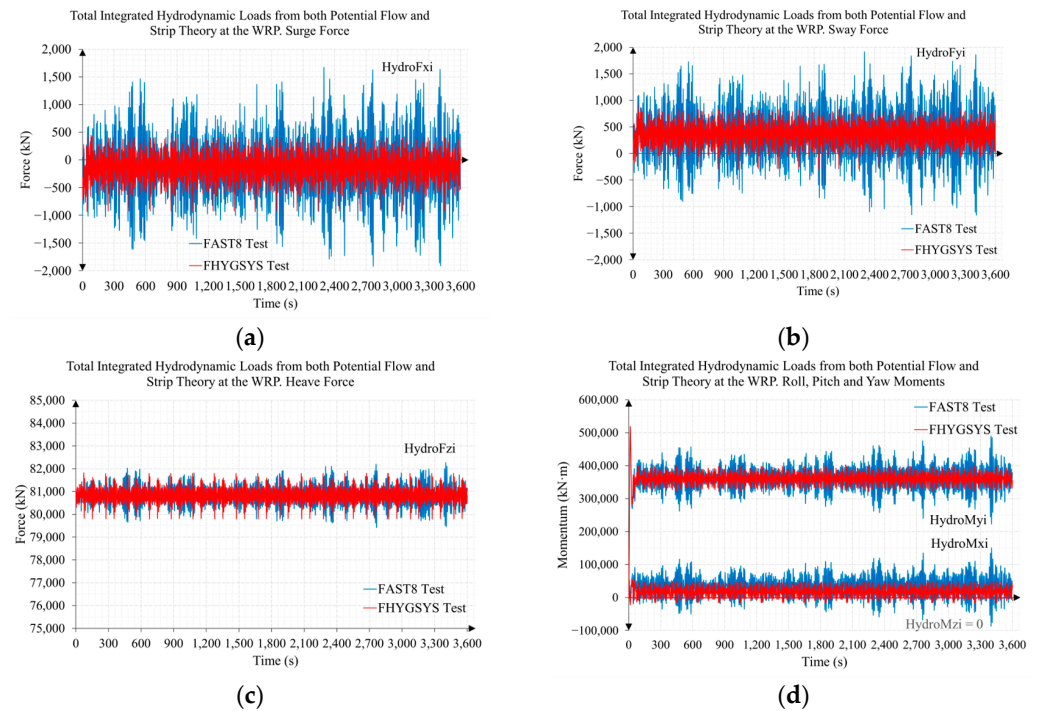
Figure A7. Total integrated hydrodynamic loads from both potential flow and strip theory at the WRP (one hour test): (**a**) surge force; (**b**) sway force; (**c**) heave force; (**d**) roll, pitch, and yaw moments.
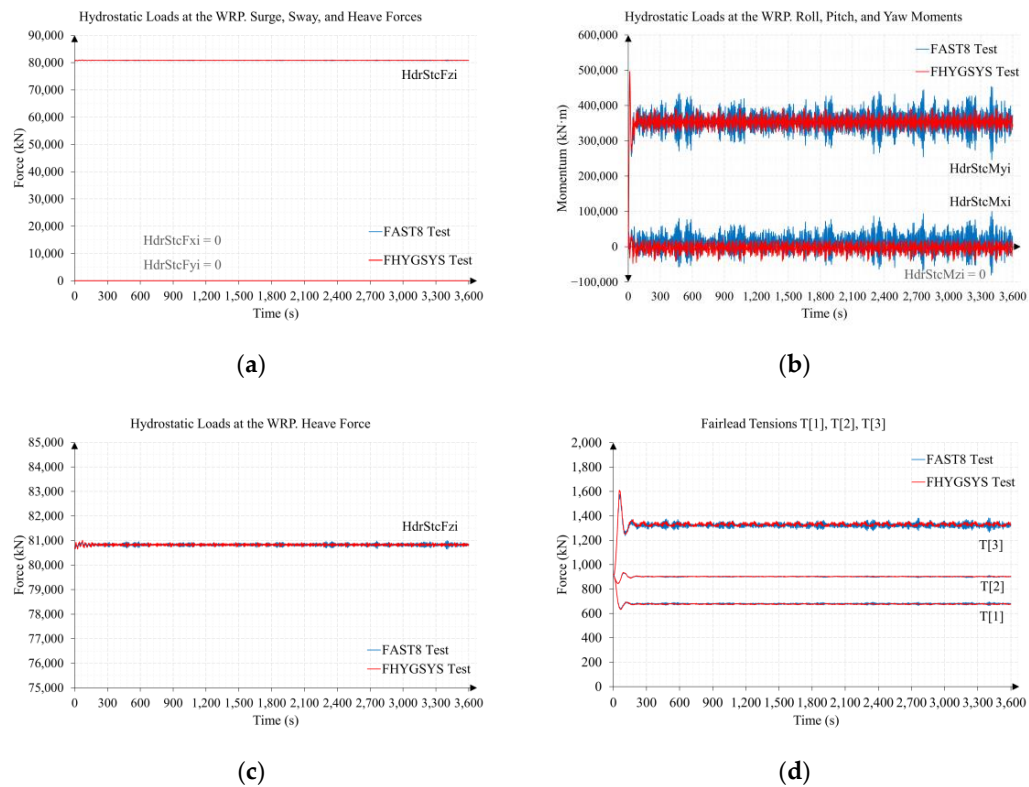
Figure A8. Hydrostatic loads at the WRP and mooring line forces (one hour test): (**a**) forces; (**b**) moments; (**c**) heave force; (**d**) force on the fairleads of the floating platform of each mooring line. In this figure, T[1], T[2] and T[3] are the nomenclature used by FASTv8 for the Fairlead Tensions in mooring lines 1, 2 and 3.
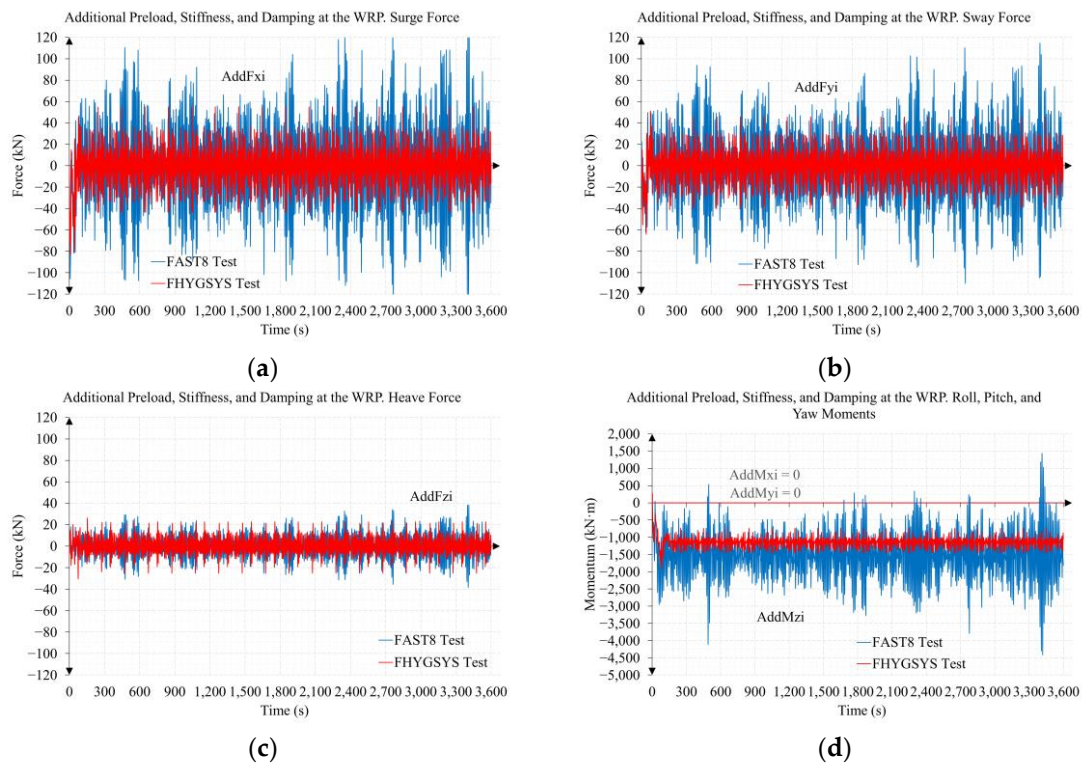
Figure A9. Additional preload, stiffness, and damping at the WRP (one hour test): (**a**) surge force; (**b**) sway force; (**c**) heave force; (**d**) roll, pitch, and yaw moments.
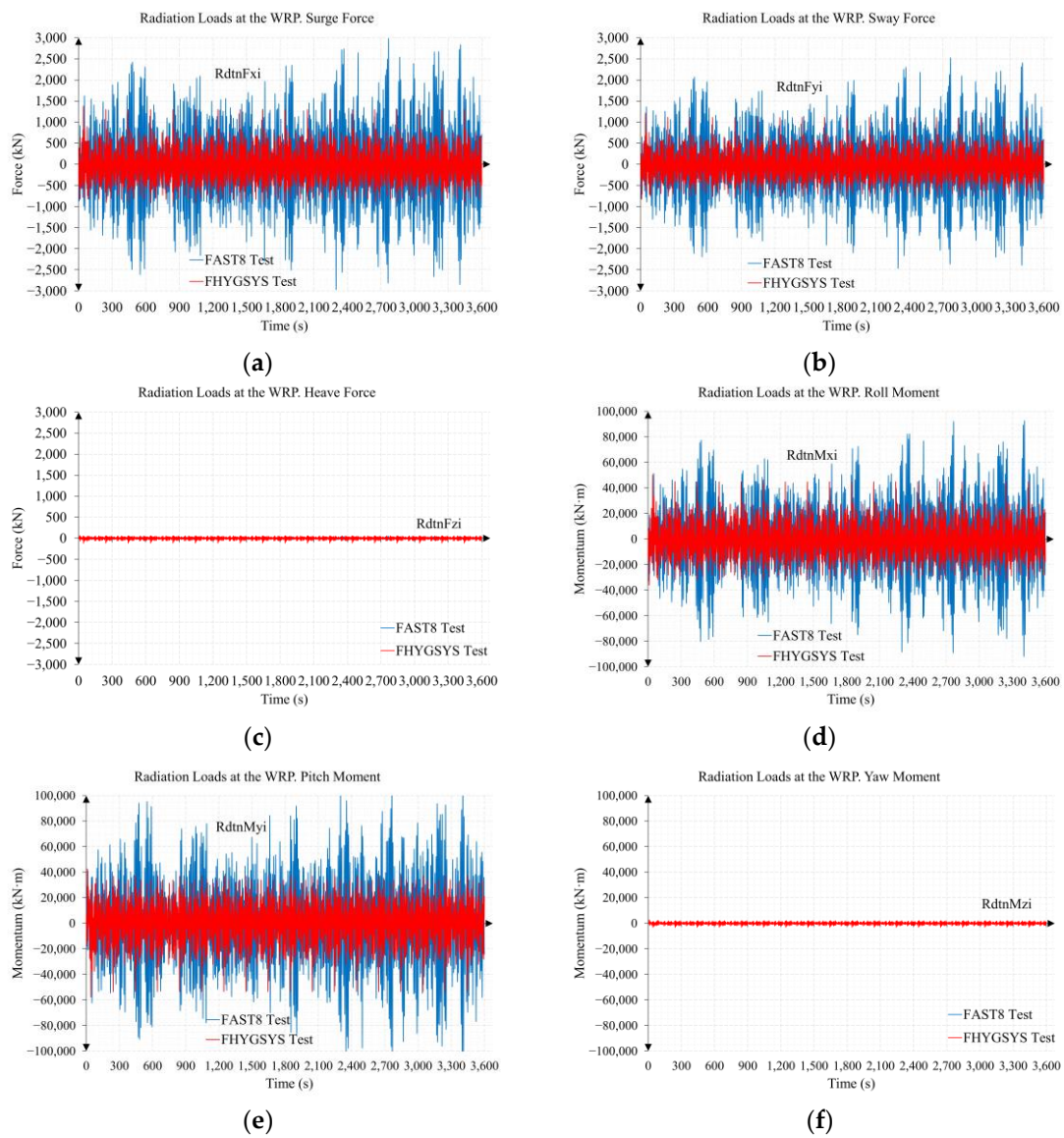
Figure A10. Radiation loads at the WRP (one hour test): (**a**) surge force; (**b**) sway force; (**c**) heave force; (**d**) roll moment; (**e**) pitch moment; (**f**) yaw moment.
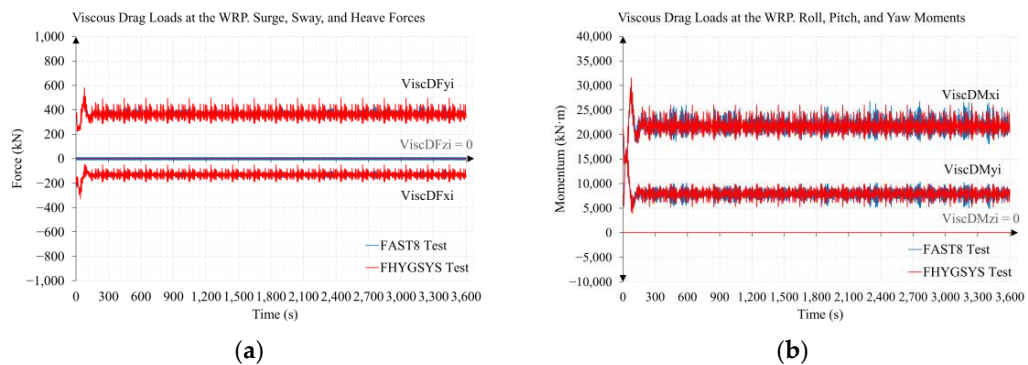
Figure A11. Viscous drag loads at the WRP (one hour test): (**a**) surge, sway, and heave forces; (**b**) roll, pitch, and yaw moments.
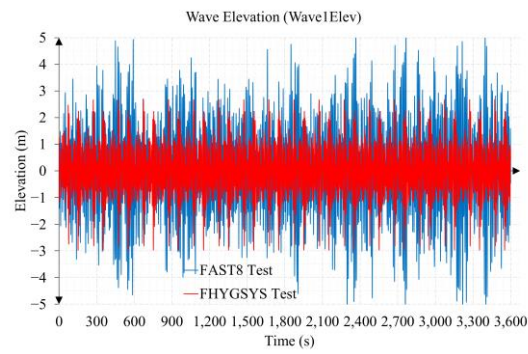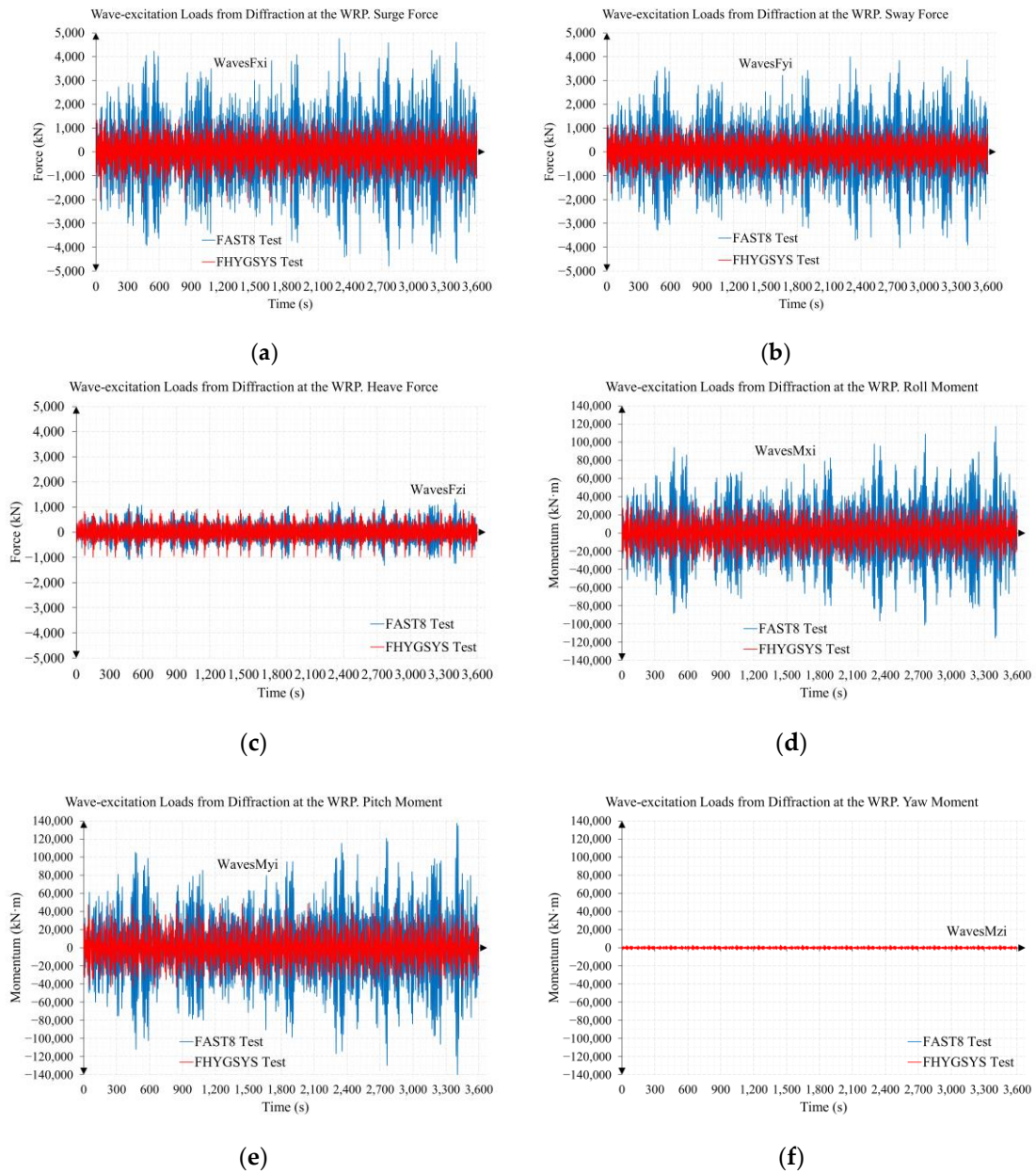
Figure A12. Total wave elevation at the WRP (one hour test).

(**a**)　　　　　　　　　　　　　　　　　　　　　(**b**)

(**c**)　　　　　　　　　　　　　　　　　　　　　(**d**)

(**e**)　　　　　　　　　　　　　　　　　　　　　(**f**)

Figure A13. Total wave-excitation loads from diffraction at the WRP (one hour test): (**a**) surge force; (**b**) sway force; (**c**) heave force; (**d**) roll moment; (**e**) pitch moment; (**f**) yaw moment.
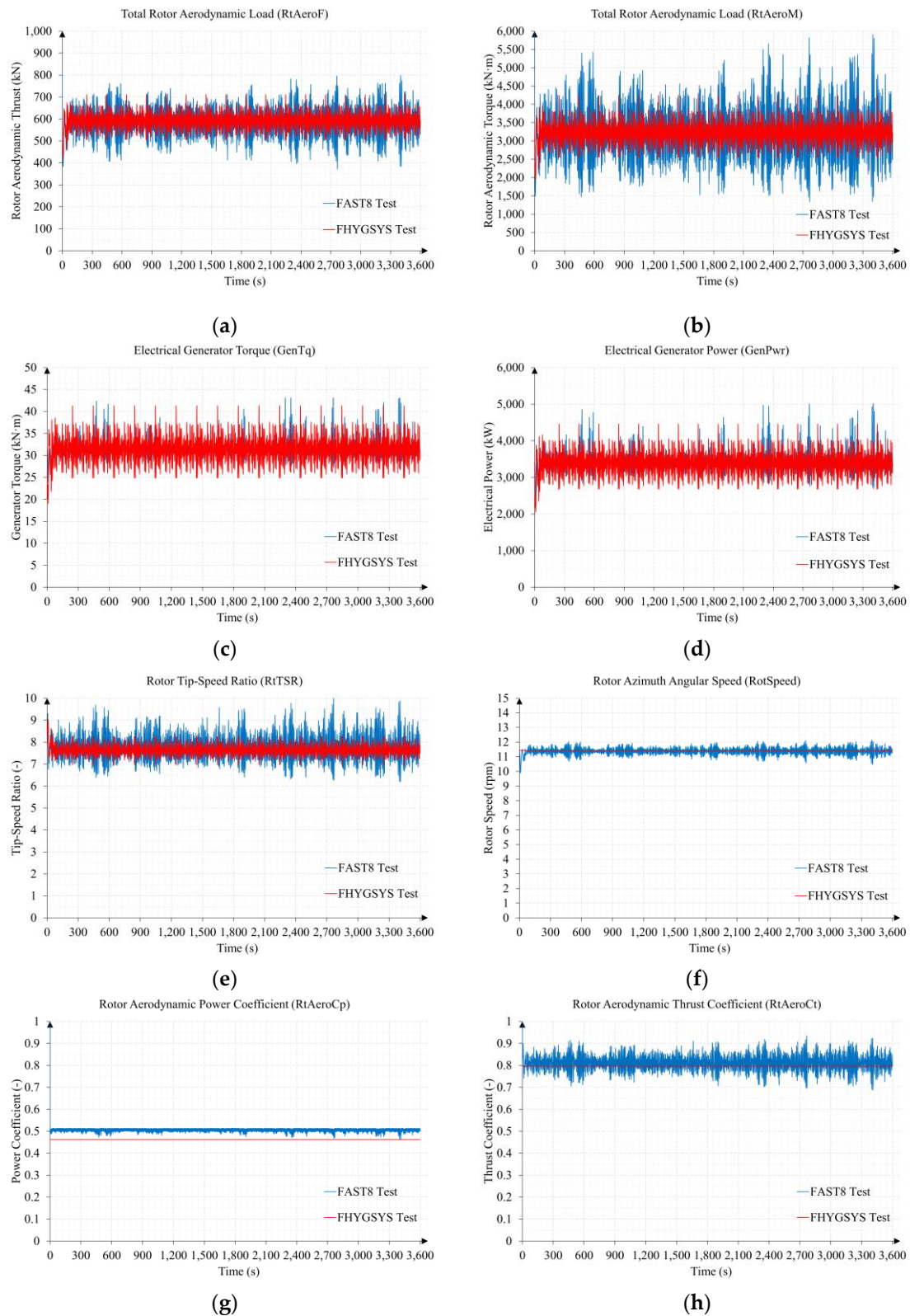
Figure A14. Wind turbine modeling results (one hour test): (**a**) rotor thrust; (**b**) rotor torque; (**c**) generator torque; (**d**) electric power generation; (**e**) tip speed ratio; (**f**) rotor speed; (**g**) power coefficient; (**h**) thrust coefficient.

References

1. Tamarit, F.; García, E.; Quiles, E.; Correcher, A. Model and Simulation of a Floating Hybrid Wind and Current Turbines Integrated Generator System, Part I: Kinematics and Dynamics. *J. Mar. Sci. Eng.* **2023**, *11*, 126. [CrossRef]
2. Jonkman, J. *Definition of the Floating System for Phase IV of OC3*; NREL/TP-500-47535; NREL: Golden, CO, USA, 2010. [CrossRef]
3. Jonkman, J.; Butterfield, S.; Musial, W.; Scott, G. *Definition of a 5-MW Reference Wind Turbine for Offshore System Development*; NREL/TP-500-38060; NREL: Golden, CO, USA, 2009. [CrossRef]
4. Bir, G.S.; Lawson, M.J.; Li, Y. Structural Design of a Horizontal-Axis Tidal Current Turbine Composite Blade. In Proceedings of the 30th International Conference on Ocean, Offshore, and Arctic Engineering, Rotterdam, The Netherlands, 19–24 June 2011. [CrossRef]
5. Lawson, M.J.; Li, Y. Development and Verification of a Computational Fluid Dynamics Model of a Horizontal-Axis Tidal Current Turbine. In Proceedings of the 30th International Conference on Ocean, Offshore, and Arctic Engineering, Rotterdam, The Netherlands, 19–24 June 2011. [CrossRef]
6. FAST. 2005. Available online: https://www.nrel.gov/wind/nwtc/fast.html (accessed on 28 January 2023).
7. FAST v8. 2016. Available online: https://www.nrel.gov/wind/nwtc/fastv8.html (accessed on 28 January 2023).
8. WAMIT. 1999. Available online: https://www.wamit.com (accessed on 28 January 2023).
9. OpenFAST. 2017. Available online: https://www.nrel.gov/wind/nwtc/openfast.html (accessed on 28 January 2023).
10. HAWC2. 2007. Available online: https://www.hawc2.dk (accessed on 28 January 2023).
11. QBlade. 2009. Available online: https://qblade.org (accessed on 28 January 2023).
12. ASHES. 2013. Available online: https://www.simis.io (accessed on 28 January 2023).
13. Simulia Wind Turbine Simulation. 2002. Available online: https://www.3ds.com/products-services/simulia/solutions/infrastructure-energy-materials/wind (accessed on 28 January 2023).
14. OpenWindPower. 2019. Available online: https://virtuosity.bentley.com/product/openwindpower (accessed on 28 January 2023).
15. DNV Software Packages. 2013. Available online: https://www.dnv.com/software/services/software-for-offshore-wind/floating-offshore-wind.html (accessed on 28 January 2023).
16. ANSYS Fluent. 2006. Available online: https://www.ansys.com/products/fluids/ansys-fluent (accessed on 10 February 2023).
17. WAsP-Suite. 1995. Available online: https://www.wasp.dk/download/wasp12-suite-installer (accessed on 28 January 2023).
18. Simulwind. 2017. Available online: https://www.simulwind.com (accessed on 28 January 2023).
19. WindTechSim. 2020. Available online: https://www.pnw.edu/civs/wind (accessed on 28 January 2023).
20. TidalBladed. 2016. Available online: https://www.dnv.com/services/industry-standard-tidal-turbine-software-modelling-tool-tidalbladed-3799 (accessed on 8 February 2023).
21. OpenTidalFarm. 2014. Available online: https://opentidalfarm.readthedocs.io/en/latest (accessed on 8 February 2023).
22. Nichita, C.; Luca, D.; Dakyo, B.; Ceanga, E. Large band simulation of the wind speed for real time wind turbine simulators. *IEEE Trans. Energy Convers.* **2002**, *17*, 523–529. [CrossRef]
23. Welfonder, E.; Neifer, R.; Spanner, M. Development and experimental identification of dynamic models for wind turbines. *Control Eng. Pract.* **1997**, *5*, 63–73. [CrossRef]
24. Van der Hoven, I. Power spectrum of horizontal wind speed in the frequency range from 0.0007 to 900 cycles per hour. *J. Atmos. Sci.* **1957**, *14*, 160–164. [CrossRef]
25. Kojabadi, H.M.; Chang, L.; Boutot, T. Development of a Novel Wind Turbine Simulator for Wind Energy Conversion Systems Using an Inverter-Controlled Induction Motor. *IEEE Trans. Energy Convers.* **2004**, *19*, 547–552. [CrossRef]
26. Neammanee, B.; Sirisumrannukul, S.; Chatratana, S. Development of a Wind Turbine Simulator for Wind Generator Testing. *Int. Energy J.* **2007**, *8*, 21–28. Available online: https://www.thaiscience.info/journals/Article/RIEJ/10968980.pdf (accessed on 26 April 2023).
27. Monfared, M.; Kojabadi, H.M.; Rastegar, H. Static and dynamic wind turbine simulator using a converter controlled dc motor. *Renew. Energy* **2007**, *33*, 906–913. [CrossRef]
28. Hu, W.; Wang, Y.; Song, X.; Wang, Z. Development of Wind Turbine Simulator for Wind Energy Conversion Systems based on Permanent Magnet Synchronous Motor. In Proceedings of the International Conference on Electrical Machines and Systems, Wuhan, China, 17–20 October 2008. Available online: https://ieeexplore.ieee.org/document/4771136 (accessed on 26 April 2023).
29. Ajirlo, K.S.; Tari, P.H.; Gharali, K.; Zandi, M. Development of a wind turbine simulator to design and test micro HAWTs. *Sustain. Energy Technol. Assess.* **2021**, *43*, 100900. [CrossRef]
30. Cordle, A.; Jonkman, J. State of the Art in Floating Wind Turbine Design Tools. In Proceedings of the 21st International Offshore and Polar Engineering Conference, Maui, HI, USA, 19–24 June 2011.
31. Sebastian, T.; Lackner, M.A. Development of a free vortex wake method code for offshore floating wind turbines. *Renew. Energy* **2012**, *46*, 269–275. [CrossRef]
32. Vorpahl, F.; Schwarze, H.; Fischer, T.; Seidel, M.; Jonkman, J. Offshore wind turbine environment, loads, simulation, and design. *WIREs Energy Environ.* **2013**, *2*, 548–570. [CrossRef]
33. Inoue, T.; Adilah, A.; Iijima, K.; Oh, S.; Suzuki, H. Discussion on Coupling Effect in Structural Load of FOWT for Condensing Wind and Wave Bins for Spectral Fatigue Analysis. *J. Mar. Sci. Eng.* **2020**, *8*, 937. [CrossRef]

34. Pham, T.-D.; Dinh, M.-C.; Kim, H.-M.; Nguyen, T.-T. Simplified Floating Wind Turbine for Real-Time Simulation of Large-Scale Floating Offshore Wind Farms. *Energies* **2021**, *14*, 4571. [CrossRef]

35. Kara, F. Coupled dynamic analysis of horizontal axis floating offshore wind turbines with a spar buoy floater. *Wind. Eng.* **2023**, 0309524X221150220. [CrossRef]

36. Jonkman, J.; Musial, W. *Offshore Code Comparison Collaboration (OC3) for IEA Task 23 Offshore Wind Technology and Deployment*; NREL/TP-5000-48191; NREL: Golden, CO, USA, 2010. [CrossRef]

37. Benelghali, S.; Balme, R.; Le Saux, K.; Benbouzid, M.; Charpentier, J.F.; Hauville, F. A Simulation Model for the Evaluation of the Electrical Power Potential Harnessed by a Marine Current Turbine. *IEEE J. Ocean. Eng.* **2007**, *32*, 786–797. [CrossRef]

38. Batten, W.M.J.; Bahaj, A.S.; Molland, A.F.; Chaplin, J.R. Experimentally validated numerical method for the hydrodynamic design of horizontal axis tidal turbines. *Ocean. Eng.* **2006**, *34*, 1013–1020. [CrossRef]

39. Bahaj, A.S.; Molland, A.F.; Chaplin, J.R.; Batten, W.M.J. Power and thrust measurements of marine current turbines under various hydrodynamic flow conditions in a cavitation tunnel and a towing tank. *Renew. Energy* **2006**, *32*, 407–426. [CrossRef]

40. Benelghali, S.; Benbouzid, M.E.H.; Charpentier, J.F.; Ahmed-Ali, T.; Munteanu, I. Experimental Validation of a Marine Current Turbine Simulator: Application to a Permanent Magnet Synchronous Generator-Based System Second-Order Sliding Mode Control. *IEEE Trans. Ind. Electron.* **2011**, *58*, 118–126. [CrossRef]

41. Caraiman, G.; Nichita, C.; Mînzu, V.; Dakyo, B.; Jo, C.H. Development of a marine current turbine simulator based on HILS concept. In Proceedings of the 3rd International Symposium on Electrical and Electronics Engineering (ISEEE), Galati, Romania, 16–18 September 2010. [CrossRef]

42. Caraiman, G.; Nichita, C.; Mînzu, V.; Dakyo, B. Marine current turbine simulator development based on hardware in the loop simulation concept. *J. Energy Power Eng.* **2011**, *5*, 877–885.

43. Churchfield, M.J.; Li, Y.; Moriarty, P.J. A large-eddy simulation study of wake propagation and power production in an array of tidal-current turbines. *Phil. Trans. R. Soc. A* **2013**, *371*, 20120421. [CrossRef]

44. ElZalabani, M.H.; Fahmy, F.; Nafeh, A.E.-S.A.; Allam, G. Modelling and Simulation of Tidal Current Turbine with Permanent Magnet Synchronous Generator. *TELKOMNIKA Indones. J. Electr. Eng.* **2015**, *13*, 57–64. [CrossRef]

45. Parkinson, S.G.; Collier, W.J. Model validation of hydrodynamic loads and performance of a full-scale tidal turbine using Tidal Bladed. *Int. J. Mar. Energy* **2016**, *16*, 279–297. [CrossRef]

46. ALSTOM 1MW Tidal Turbine. 2013. Available online: https://www.emec.org.uk/about-us/our-tidal-clients/alstom (accessed on 12 February 2023).

47. Einrí, A.N.; Jónsdóttir, G.M.; Milano, F. Modeling and Control of Marine Current Turbines and Energy Storage Systems. *IFAC-PapersOnLine* **2019**, *52*, 425–430. [CrossRef]

48. Milano, F. A python-based software tool for power system analysis. In Proceedings of the 2013 IEEE Power & Energy Society General Meeting, Vancouver, BC, Canada, 21–25 July 2013. [CrossRef]

49. Gu, J.; Cai, F.; Müller, N.; Zhang, Y.; Chen, H. Two-Way Fluid–Solid Interaction Analysis for a Horizontal Axis Marine Current Turbine with LES. *Water* **2020**, *12*, 98. [CrossRef]

50. Gao, Y.; Liu, H.; Lin, Y.; Gu, Y.; Ni, Y. Hydrodynamic Analysis of Tidal Current Turbine under Water-Sediment Conditions. *J. Mar. Sci. Eng.* **2022**, *10*, 515. [CrossRef]

51. García, E.; Fabuel, D.; Pizá, R.; Morant, F.; Correcher, A.; Quiles, E. Hydro-Wind Kinetics Integrated Module for the Renewable Energy Generation. In Proceedings of the 2012 Oceans-Yeosu, Yeosu, Republic of Korea, 21–24 May 2012. [CrossRef]

52. García, E.; Pizá, R.; Benavides, X.; Quiles, E.; Correcher, A.; Morant, F. Mechanical Augmentation Channel Design for Turbine Current Generators. *Adv. Mech. Eng.* **2014**, *6*, 650131. [CrossRef]

53. Szabó, L. On the use of rotary-linear generators in floating hybrid wind and wave energy conversion systems. In Proceedings of the 2018 IEEE International Conference on Automation, Quality and Testing, Robotics (AQTR), Cluj-Napoca, Romania, 24–26 May 2018. [CrossRef]

54. Derakhshan, S.; Moghimi, M.; Motawej, H. Development of a mathematical model to design an offshore wind and wave hybrid energy system. *Energy Equip. Syst.* **2018**, *6*, 181–200. [CrossRef]

55. Tamarit, F.; García, E.; Correcher, A.; Quiles, E.; Morant, F. Mathematical Model of a Cogeneration System Composed of a Floating Wind Turbine and Two Marine Current Turbines. In Proceedings of the 7th International Conference on Systems and Control (ICSC 2018), Valencia, Spain, 24–26 October 2018. [CrossRef]

56. Hu, J.; Zhou, B.; Vogel, C.; Liu, P.; Willden, R.; Sun, K.; Zang, J.; Geng, J.; Jin, P.; Cui, L.; et al. Optimal design and performance analysis of a hybrid system combing a floating wind platform and wave energy converters. *Appl. Energy* **2020**, *269*, 114998. [CrossRef]

57. García, E.; Correcher, A.; Quiles, E.; Tamarit, F.; Morant, F. Control and Supervision Requirements for Floating Hybrid Generator Systems. *Int. J. Environ. Res. Public Health* **2022**, *19*, 12781. [CrossRef]

58. Newman, J.N. *Marine Hydrodynamics*; The MIT Press: Cambridge, MA, USA, 1977.

59. Paul, R.P. *Robot Manipulators: Mathematics, Programming, and Control*; The MIT Press: Cambridge, MA, USA, 1981.

60. Fossen, T.I. *Marine Control Systems. Guidance, Navigation and Control of Ships, Rings and Underwater Vehicles*, 1st ed.; Marine Cybernetics: Trondheim, Norway, 2002.

61. Jonkman, J. *Dynamics Modeling and Loads Analysis of an Offshore Floating Wind Turbine*; NREL/TP-500-41958; NREL: Golden, CO, USA, 2007. [CrossRef]

62. Riley, W.F.; Sturges, L.D. *Engineering Mechanics: Statics*, 2nd ed.; John Wiley & Sons, Inc.: Hoboken, NJ, USA, 1996.

63. Hibbeler, R.C. *Engineering Mechanics: Statics*, 12th ed.; Prentice Hall, Inc.: Hoboken, NJ, USA, 2009.

64. Beer, F.P.; Johnston, E.R.; Mazurek, D.F.; Eisenberg, E.R. *Vector Mechanics for Engineers: Statics*, 9th ed.; McGraw-Hill: New York, NY, USA, 2009.

65. *IEC 61400–3*; Wind Turbines—Part 3: Design Requirements for Offshore Wind Turbines, 1st ed. International Electrotechnical Commission (IEC): Geneva, Switzerland, 2009.

66. Jonkman, J.M. *Modeling of the UAE Wind Turbine for Refinement of FAST_AD*; NREL/TP-500-34755; NREL: Golden, CO, USA, 2003. [CrossRef]

67. Masciola, M.; Jonkman, J.; Robertson, A. Implementation of a Multisegmented, Quasi-Static Cable Model. In Proceedings of the 23rd International Offshore and Polar Engineering Conference Anchorage, Anchorage, AK, USA, 30 June–5 July 2013.

68. Smith, R.T.; Minton, R.B. *Calculus, Premiere ed.*; McGraw-Hill: Boston, MA, USA, 2000.

69. Chapra, S.C.; Canale, R.P. *Numerical Methods for Engineers: With Software and Programming Applications*, 4th ed.; McGraw-Hill: New York, NY, USA, 2001.

70. Gao, Z.-T.; Feng, X.-Y.; Zhang, Z.-T.; Liu, Z.-L.; Gao, X.-X.; Zhang, L.-J.; Li, S.; Li, Y. A brief discussion on offshore wind turbine hydrodynamics problem. *J. Hydrodyn.* **2022**, *34*, 15–30. [CrossRef]

71. Tian, W.; Wang, Y.; Shi, W.; Michailides, C.; Wan, L.; Chen, M. Numerical study of hydrodynamic responses for a combined concept of semisubmersible wind turbine and different layouts of a wave energy converter. *Ocean Eng.* **2023**, *272*, 113824. [CrossRef]

72. Matha, D. *Model Development and Loads Analysis of an Offshore Wind Turbine on a Tension Leg Platform, with a Comparison to Other Floating Turbine Concepts*; NREL/SR-500-45891; NREL: Golden, CO, USA, 2010. [CrossRef]

73. Roald, L.; Jonkman, J.; Robertson, A. *The Effect of Second-Order Hydrodynamics on a Floating Offshore Wind Turbine*; NREL/TP-5000-61452; NREL: Golden, CO, USA, 2014. [CrossRef]

74. Berteaux, H.O. *Buoy Engineering*; John Wiley & Sons, Inc.: New York, NY, USA, 1976.

75. WAMIT User Manual. 2020. Available online: https://www.wamit.com/manualv7.4/wamit_v74manual.html (accessed on 8 March 2023).

76. Faltinsen, O.M. *Sea Loads on Ships and Offshore Structures*; Cambridge University Press: Cambridge, UK, 1990.

77. Betti, G.; Farina, M.; Marzorati, A.; Scattolini, R.; Guagliardi, G.A. Modeling and control of a floating wind turbine with spar buoy platform. In Proceedings of the 2012 IEEE International Energy Conference and Exhibition (ENERGYCON), Florence, Italy, 9–12 September 2012. [CrossRef]

78. Imlay, F.H. *The Complete Expressions for Added Mass of a Rigid Body Moving in an Ideal Fluid*; DTMB 1528; Department of the Navy David Taylor Model Basin: Washington, DC, USA, 1961.

79. Sclavounos, P.D. "13.022 Surface Waves and Their Interaction with Floating Bodies, Lecture Notes" Massachusetts Institute of Technology (MIT) OpenCourseWare. Lecture note 11. Available online: https://dspace.mit.edu/bitstream/handle/1721.1/35268/13-022Spring-2002/OcwWeb/Ocean-Engineering/13-022Surface-Waves-and-their-Interaction-With-Floating-BodiesSpring2002/LectureNotes/index.htm (accessed on 21 March 2023).

80. Lee, K.H. Responses of Floating Wind Turbines to Wind and Wave Excitation. Master's thesis, Massachusetts Institute of Technology, Cambridge, MA, USA, January 2005.

81. Hansen, M.O.L. *Aerodynamics of Wind Turbines*, 1st ed.; James & James (Science Publishers) Ltd.: London, UK, 2000.

82. Jonkman, J.M.; Robertson, A.N.; Hayman, G.J. *HydroDyn User's Guide and Theory Manual*; NREL/TP Draft Paper; NREL: Golden, CO, USA. Available online: https://www.nrel.gov/wind/nwtc/assets/downloads/HydroDyn/HydroDyn_Manual.pdf (accessed on 26 April 2023).

83. Scarlett, G.T.; Viola, I.M. Unsteady hydrodynamics of tidal turbine blades. *Renew. Energy* **2020**, *146*, 843–855. [CrossRef]

84. Robertson, A.; Jonkman, J.; Masciola, M.; Song, H.; Goupee, A.; Coulling, A.; Luan, C. *Definition of the Semisubmersible Floating System for Phase II of OC4*; NREL/TP-5000-60601; NREL: Golden, CO, USA, 2014. [CrossRef]